Fermi National Accelerator Laboratory

p̄p Collider Physics *

Dan Green
Fermi National Accelerator Laboratory
P.O. Box 500, Batavia, Illinois 60510

March 1989

$\bar{p}p$ COLLIDER PHYSICS

Dan Green
Fermi National Accelerator Laboratory[1]
P. O. Box 500
Batavia, Illinois 60510
U. S. A.

ABSTRACT

This note encompasses a set of six lectures given at the summer school
held at Campos Do Jordao on January of 1989 near Sao Paulo, Brazil.
The intent of the lectures was to describe the physics of $\bar{p}p$ at CERN
and Fermilab. Particular attention has been paid to making a self con-
tained presentation to a prospective audience of graduate students.
Since large Monte Carlo codes might not be available to all members
of this audience, great reliance was placed on "back of the envelope esti-
mates." Emphasis was also placed on experimental data rather than
theoretical speculation, since predictions for, for example, supersym
-metric particle production are easily obtained by transcription of
formulae already obtained.

A. POINT PARTICLE CONSTITUENTS AND THEIR COUPLINGS

In the field of elementary particle physics we have come to a synthesis in our
understanding which goes under the name of the Standard Model. Matter con-
sists of a number of pointlike spin one half fermions which come in two categories,
quarks and leptons. Within these two categories quark and lepton doublet pairs
are replicated in at least three generations. Energy, or the forces between matter,
is communicated by a series of spin one gauge bosons. There are eight gluons com-
municating the strong force, the photon communicating the electromagnetic force,
and the three charged and neutral gauge bosons, the W and Z communicating

---

[1]Operated by Universities Research Association Inc. under contract with the United States
Department of Energy

the weak force. The coupling constants describing the strength of these forces are all dimensionless. A schematic representation of the Standard Model is shown in Fig. A.1.

$$\text{QUARKS} \quad \begin{bmatrix} u \\ d \end{bmatrix} \quad \begin{bmatrix} c \\ s \end{bmatrix} \quad \begin{bmatrix} t \\ b \end{bmatrix} , \quad Q = \begin{bmatrix} 2/3 \\ -1/3 \end{bmatrix}$$

$$\text{LEPTONS} \quad \begin{bmatrix} e \\ \nu e \end{bmatrix} \quad \begin{bmatrix} \mu \\ \nu \mu \end{bmatrix} \quad \begin{bmatrix} \tau \\ \nu \tau \end{bmatrix} , \quad Q = \begin{bmatrix} 1 \\ 0 \end{bmatrix}$$

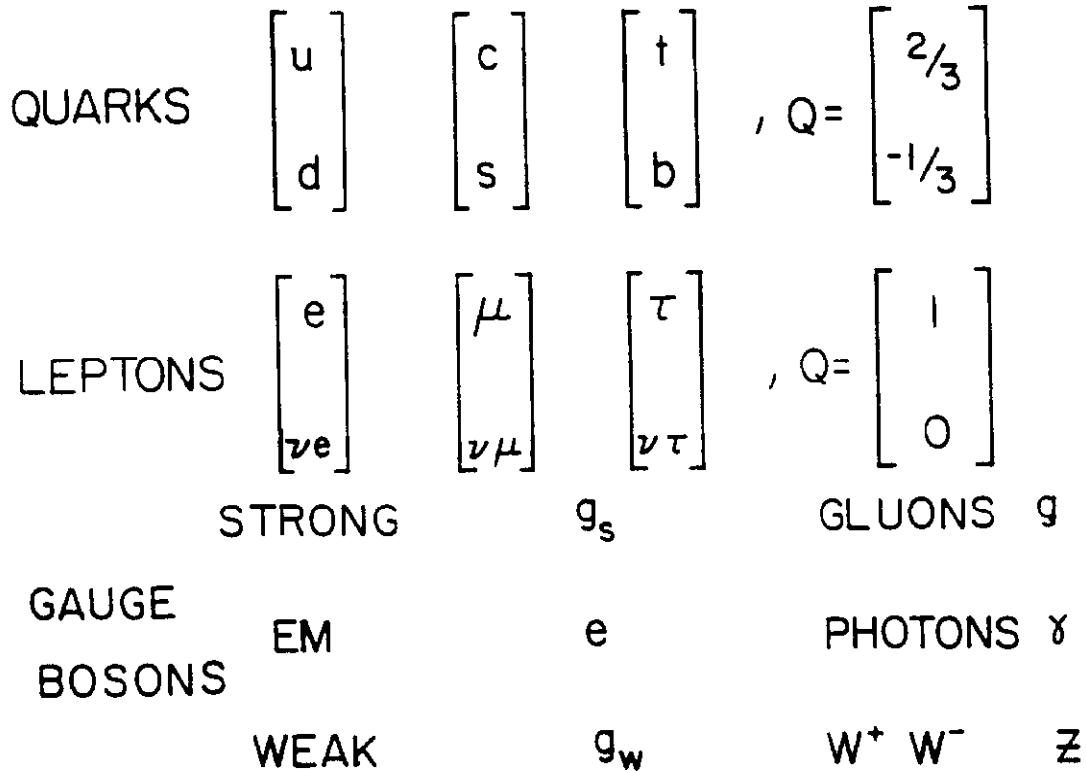| GAUGE BOSONS			
STRONG	g_s	GLUONS	g
EM	e	PHOTONS	γ
WEAK	g_w	$W^+\ W^-$	Z

Figure A.1: Standard Model for matter and energy. Constituents are doublets of quarks and leptons in three generations. Forces are transmitted by gauge bosons with dimensionless couplings.

In order to understand forces in the Standard Model, we'll start with the electromagnetic force which has the familiar form of minimal coupling. One starts with the kinetic term in the LaGrangian density for free particles and replaces the derivative by the covariant derivative. This derivative contains the interactive field which means that the replacement generates the interaction terms. They appear in the form of a current dotted with the interacting electromagnetic field.

2

$$\mathcal{L} = \bar{\psi}(\partial\!\!\!/ - m)\psi$$
$$\partial \rightarrow D = \partial - \imath eA \qquad (A.1)$$
$$\mathcal{L}_I = -\imath e(\bar{\psi}\gamma_\mu\psi)A^\mu$$
$$= -\imath e J_\mu A^\mu$$

Extending the scheme to the strong interactions, one replaces the U(1) group of the electric charge to the SU(3) group of color. Remember that color is effectively the charge of the strong interaction. This replacement leads to an octet of colored gluons, interacting with a color triplet of quarks. The gluon fields are represented by b_c.

$$U(1) \rightarrow SU(3)$$
$$-\imath e \rightarrow g_s\lambda_{ab}^c$$
$$3 \otimes \bar{3} = 1 \oplus 8$$
$$a,b = 1,2,3 \qquad c = 1,.......,8 \qquad (A.2)$$
$$R,\ B,\ G \qquad R\bar{B},\ R\bar{G},\ B\bar{R},\ B\bar{G},\ G\bar{R},\ G\bar{B},$$
$$(R\bar{R} + B\bar{B} - 2G\bar{G})/\sqrt{6},\ (R\bar{R} + B\bar{B})/\sqrt{2}$$
$$D = \partial - (g_s/2)\lambda_{ab}^c b_c$$

In the case of the electromagnetic and weak interactions, the U(1) group is replaced by an SU(2) ⊗ U(1) group. The weak doublets which we showed in Fig. A.1 interact with a triplet and singlet of gauge bosons giving rise to the electromagnetic and weak interactions. The covariant derivative introducing the W and B fields is given below:

$$U(1) \rightarrow SU(2) \otimes U(1)$$
$$Q_W \equiv (I_3 + Y/2)_W$$
$$e \rightarrow gQ_W$$
$$2 \otimes \bar{2} = 1 \oplus 3 \qquad (A.3)$$
$$\begin{pmatrix} q \\ q' \end{pmatrix} \qquad B^0, \qquad\qquad U(1),\ g_1$$
$$W^+, W^\circ, W^-,\ SU(2),\ g_2$$
$$D = \partial - \imath[g_1(Y/2)B + g_2\vec{I}\cdot\vec{W}]$$

3

There are two coupling constants, one associated with the SU(2) group, that is g_2, and the other with the U(1) group g_1. Ultimately we want to connect them with the physical couplings, the electromagnetic charge e, and the Fermi constant G. In order to do that we define physical states A and Z as arbitrary unitary rotations of the W and B neutral components. Then we identify the coupling of the A to be electric charge.

$$a) \begin{pmatrix} A \\ Z \end{pmatrix} = \begin{pmatrix} \cos\theta_W & \sin\theta_W \\ -\sin\theta_W & \cos\theta_W \end{pmatrix} \begin{pmatrix} B^0 \\ W^0 \end{pmatrix}$$

$$D = \partial - \imath \left[\begin{array}{c} (g_1 Y/2 \cos\theta_W + g_2 I_3 \sin\theta_W)A + g_2(I^+ W^- + I^- W^+) \\ +(g_2 I_3 \cos\theta_W - g_1 Y/2 \sin\theta_W)Z \end{array} \right]$$

$$b) \qquad g_1(Q - I_3)\cos\theta_W + g_2 I_3 \sin\theta_W = Qe \qquad\qquad (A.4)$$

$$g_1 \cos\theta_W = g_2 \sin\theta_W = e$$

This identification immediately shows the unification of electromagnetism and weak interactions in that the couplings g_1 and g_2 are both equal to the electromagnetic coupling e up to trigonometric functions. Hence, the minimal gauge coupling scheme again specifies the interactions between the fermions and gauge bosons. In particular, we find that g_2 specifies the charge changing weak currents and so we expect to identify g_2 with the Fermi constant. There is a more complicated connection between what is new in this theory, the prediction of the weak-neutral currents and the coupling constants g_1 and g_2.

$$a) \qquad D = \partial - \imath \left[\begin{array}{c} eQA + g_2(I^+ W^- + I^- W^+) + \\ (-g_1(Q - I_3)\sin\theta_W + g_2 I_3 \cos\theta_W)Z \end{array} \right]$$

$$
\begin{aligned}
b) \qquad & -g_1 Q \sin\theta_W + g_1 I_3 \sin\theta_W + g_2 I_3 \cos\theta_W \\
&= \sqrt{g_1^2 + g_2^2} \left[-Q \sin^2\theta_W + I_3 \sin^2\theta_W + I_3 \cos^2\theta_W \right] \qquad (A.5) \\
&= \sqrt{g_1^2 + g_2^2} \left[I_3 - Q \sin^2\theta_W \right]
\end{aligned}
$$

$$c) \qquad D = \partial - \imath \left[eQA + g_2(I^+ W^- + I^- W^+) + \sqrt{g_1^2 + g_2^2}(I_3 - Q\sin^2\theta_W)Z \right]$$

We now have derived the covariant derivative which specifies the interaction in terms of the physical particles of the theory, the photon, the charged-weak bosons, and the neutral-weak boson. The interactions that are specified by the gauge couplings of the fermions to the gauge bosons for the three forces; electromagnetic, strong, and weak are shown in Fig. A.2 with $g_2 \equiv g_W$. Left-handed weak-charged currents are explicitly assumed in Fig. A.2.
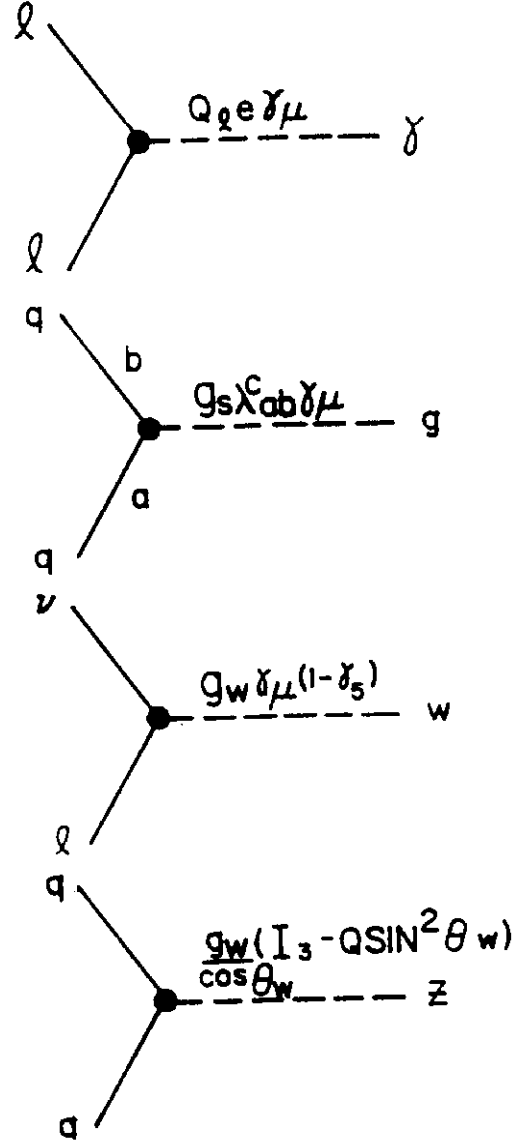

Figure A.2: Coupling of fermions to gauge bosons for the three forces; electromagnetic, strong, and weak.

So far we have specified the couplings of the bosons to the fermions. However, in the electroweak case, there is no particular reason why the weak eigenstates

should be equal to the strong eigenstates. Therefore, even assuming a universal electroweak-lepton coupling, there can be mixing in the quark sector. The coupling scheme for the favored quark couplings along with the relevant color factors is shown schematically for both W and Z gauge bosons in Fig. A.3. From these figures, it is very easy to estimate the branching ratios of Ws and Zs into different final states. We will have use of these estimates later. The W and Z bosons couple to the quark and lepton doublets shown in Fig. A.1.

$$1 \ : \ 1 \ : \ 1 \ : 3 : 3$$
$$e, \quad \mu, \quad \tau, \quad u,c$$

$$W - - \overset{g_W}{\bullet}$$

$$\nu e \ , \nu \mu \ , \nu \tau, \ \bar{d}, \bar{s}$$

$$1 : 1 : 1 : 1 \ : \ 1 \ : \ 1 : 3 : 3 : 3 : 3 : 3$$
$$e, \mu, \tau \ , \ \nu e \ , \ \nu_\mu \ , \nu \tau, u, d, s, c, b$$

$$Z - - \overset{g_W}{\bullet}$$

$$\bar{e}, \bar{\mu}, \bar{\tau}, \bar{\nu}_e \ , \ \bar{\nu}_\mu \ , \ \bar{\nu}_\tau, \bar{u}, \bar{d}, \bar{s}, \bar{c}, \bar{b}$$
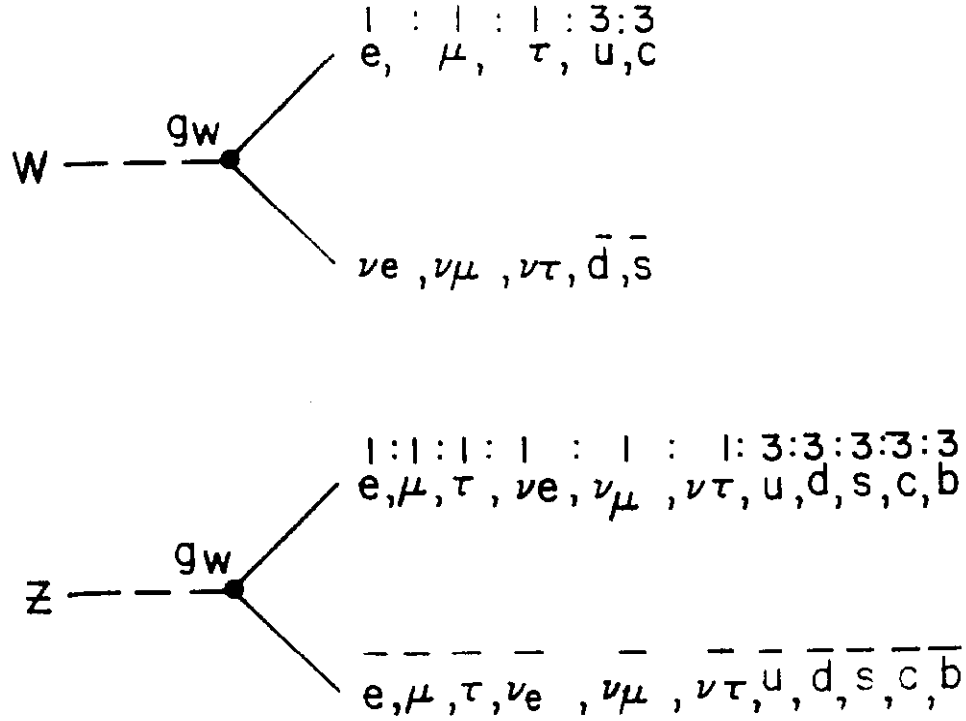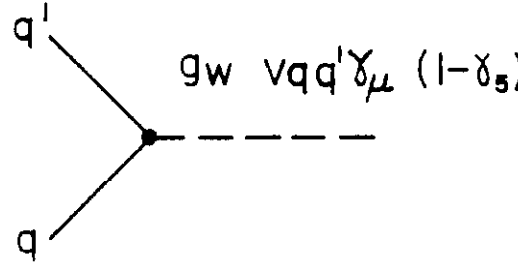
Figure A.3: Universal lepton coupling to W and Z gauge bosons. Favored quark couplings with color factors are also indicated.

Finally, in Fig. A.4 the non-diagonal coupling of W gauge bosons to the quarks is defined via the unitary matrix whose approximate form is also given in Fig. A.4. This matrix is known as the Kobayashi-Maskawa (KM) matrix.

$$g_W \, V_{qq'} \gamma_\mu (1-\gamma_5)$$

$$V_{qq'} \cong \begin{bmatrix} 1 & \theta & \theta^3 e^{-i\delta} \\ -\theta & 1 & \theta^2 \\ -\theta^3 e^{i\delta} & -\theta^2 & 1 \end{bmatrix} \begin{bmatrix} u \\ c \\ t \end{bmatrix}$$

$$\begin{bmatrix} d & s & b \end{bmatrix}$$

$$\theta \cong \theta_c \cong 1/5$$

Figure A.4: Coupling of W gauge bosons to quarks. Approximate form of the KM matrix.

The form of $V_{qq'}$ modifies the W-lepton coupling shown in Fig. A.2. The matrix $V_{qq'}$ is almost diagonal in the charge changing strong eigenstates - the quarks. The $V_{us} \sim \theta_c$ term comes from comparing $K \to \mu\nu$ to $\pi \to \mu\nu$ decays. The $V_{bc} \sim \theta_c^2$ result comes from the B lifetime measurement. The θ_c^3 terms are inferred using three generation unitarity. The complex phase of V_{bu} allows CP-violation to occur.

From simple dimensional arguments we expect that the widths, Γ, of the gauge bosons should be proportional to the masses of the bosons times the coupling constants squared. Given electroweak unification this means α times the mass. So, if the mass is about 100 GeV, we expect widths of about 1 GeV. We will quote the exact calculations in Section C, when we discuss production properties of W and Z bosons.

Now let's turn to the masses of the electroweak-gauge bosons in the presence of spontaneous symmetry breaking. This means that there exists a Higgs doublet

scalar field with a vacuum condensate which we represent by η. When the kinetic terms in the Higgs LaGrangian are replaced by the covariant derivative, which we have already worked out, we find that masses for the W and Z are generated; the photon remains massless.

$$
\begin{aligned}
(\partial\phi)^*(\partial\phi) &\rightarrow (D\phi)^*(D\phi) \\
<\phi> &= \begin{pmatrix} O \\ \eta \end{pmatrix} \\
(D\phi)^*(D\phi) &\sim \left(\frac{g_2^2}{2}\eta^2\right)\bar{W}W + \left(\frac{(g_1^2 + g_2^2)}{2}\eta^2\right)\bar{Z}Z
\end{aligned}
\tag{A.6}
$$

The W and Z masses are related to the coupling constants and the vacuum expectation value of the Higgs field.

$$
\begin{aligned}
M_\gamma &= 0 \\
M_W &= g_2\eta/\sqrt{2} \\
M_Z &= \sqrt{g_1^2 + g_2^2}\,\eta/\sqrt{2} \\
M_Z &= M_W/\cos\theta_W
\end{aligned}
\tag{A.7}
$$

The measured value of the Fermi constant is about 10^{-5} per GeV^2 as measured in, for example, muon decay. We can relate this value to the coupling constant $g_2 = g_W$ and from there we can derive a value for the vacuum expectation value.

$$
\begin{aligned}
g_2 &= g_W \\
G/\sqrt{2} &= g_W^2/8M_W^2 \\
\eta &= \sqrt{2}M_W/g_W \\
&= \frac{1}{\sqrt{G2\sqrt{2}}} = 175 \text{ GeV}
\end{aligned}
\tag{A.8}
$$

Of course, the masses of the W and Z bosons are to the same order of magnitude as the vacuum expectation value. The relationship in Eq. A.8 relates the weak coupling constant g_W, along with the W boson propagator g_W^2/M_W^2, to a contact 4 fermion effective coupling G. The Weinberg angle is measured in neutral current interactions (see Eq. A.5.c) to be $\sin^2\theta_W \sim 1/5$. This means that $g_W^2 = e^2/\sin^2\theta_W = 4\pi\alpha^2/\sin^2\theta_W$. With $\alpha = 1/137$, $g_W \sim 0.65$ or, $M_W = g_W\eta/\sqrt{2} \sim 80$

8

GeV and ($\theta_W \sim 26^\circ$) $M_Z \sim 89$ GeV. The experimental data confirming these predictions will be shown in Section C of this note.

The relationships were spectacularly confirmed at CERN when the W and Z bosons were both discovered in the mid 1980s. However, it is safe to say that many mysteries still remain. For example, just for amusement you can evaluate the critical density to close the universe. It turns out to be about 10 kilovolts per cubic centimeter. By contrast, the energy density due to the vacuum expectation value of the Higgs field is about 10^{55} times larger. Clearly, it requires some tuning to make the cosmological constant small.

What are the Higgs field couplings to the other particles in the theory? One allows not only a vacuum expectation value but an oscillation about it. In this case, the kinetic terms in the LaGrangian not only generate masses for the Ws and Zs but interactions between gauge bosons and the Higgs particles. These interaction terms will be important in discussing Higgs decay modes in Section C.

$$\phi = \begin{pmatrix} 0 \\ \eta + H \end{pmatrix} \tag{A.9}$$

$$(D\phi)^\star (D\phi) = \frac{g_2^2}{2}(\eta + H)^2 \bar{W}W + \frac{(g_1^2 + g_2^2)}{2}(\eta + H)^2 \bar{Z}Z$$

These interactions are schematically shown in Fig. A.5; they are easily read off from Eq. A.9.
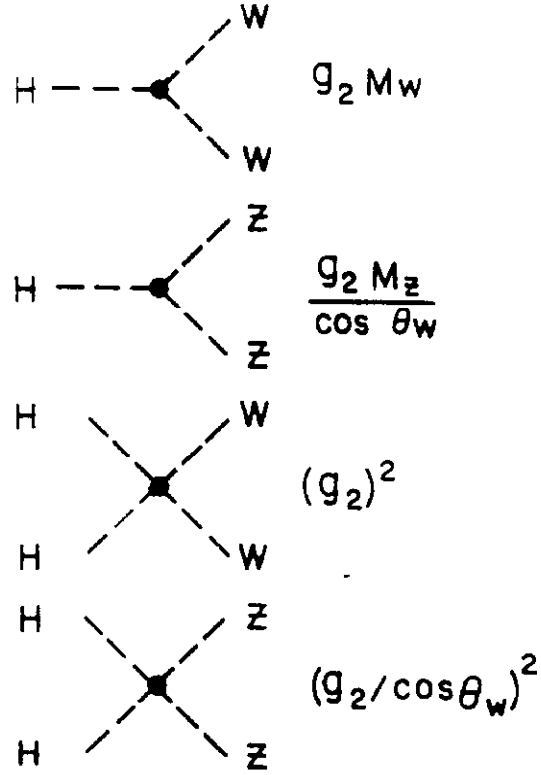
9

Figure A.5: Higgs couplings to electroweak bosons.

We can now ask about the coupling of Higgs particles to the fermions in the electroweak theory. This begins by specifying Yukawa couplings with ad hoc coupling constants.

$$
\begin{aligned}
\mathcal{L}_Y &= G'\bar{\ell}\phi\ell \\
&= G'\bar{\ell}(\eta + H)\ell \\
&\equiv m\bar{\ell}\ell + G'\bar{\ell}\ell H \\
m &= G'\eta
\end{aligned}
\tag{A.10}
$$

These Yukawa interactions generate mass terms for the fermions. However, there are unspecified coupling constants so there is no prediction for the fermion masses.

10

Even so, we find out that the Yukawa coupling constant is related to the mass. This means that the coupling of Higgs particles to fermions is proportional to the mass of the fermions.

$$
\begin{aligned}
\mathcal{L}_I &= G'\bar{\ell}\ell H \\
&= \frac{m}{\eta}\bar{\ell}\ell H \\
&\sim \left(\frac{g_W m}{\sqrt{2}M_W}\right)\bar{\ell}\ell H \\
&\sim (\sqrt{G}m)\bar{\ell}\ell H
\end{aligned} \tag{A.11}
$$

This fact will turn out to be very important in search strategies for Higgs particles. The implied Higgs couplings to fermions is shown schematically in Fig. A.6.
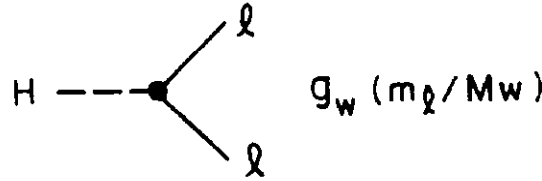
Figure A.6: Higgs coupling to fermions.

What about couplings among the gauge bosons? We have already derived the covariant derivative in Eq. A.5.c. Given the fermion kinetic piece in the Lagrangian, the substitution $\partial \to D$ generates the interactions shown in Fig. A.2 between gauge bosons and fermions. In an analagous fashion, the boson kinetic term $(\partial\Phi)^*(\partial\Phi)$ under the substitution $\partial \to D$ obviously generates "quartic" couplings:

$$
\begin{aligned}
D &= \partial - i\sum_{j}^{3} g_j\Phi_j, \quad \Phi_j = A, W, Z \\
(\partial\Phi)^*(\partial\Phi) &\to (D\Phi)(D\Phi)
\end{aligned} \tag{A.12}
$$

$$
\mathcal{L}_I \sim g_j\partial\Phi_1\Phi_2\Phi_3, \quad g_j^2\Phi_1\Phi_2\Phi_3\Phi_4
$$

These couplings are shown schematically in Fig. A.7. They are similar to those shown in Fig. A.5. The triple couplings are proportional to $g_W q$, due to the ∂ factor,

while the quartic couplings only contain the fields themselves and are proportional to g_W^2. Clearly, the implication of Eq. A.2 is that gluons also have triple and quartic non-Abelian couplings.
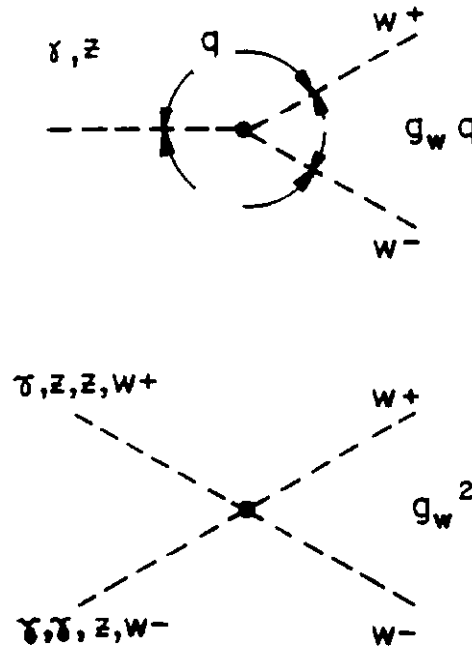

Figure A.7: Couplings between electroweak bosons.

In summary, what we have done in this Section is to very quickly and crudely define the constituents in the Standard Model, the quarks, the leptons, and the gauge bosons. Using the gauge principle, in a very schematic way, we have derived the interactions between the elements in the Standard Model. Those interactions are specified by coupling constants, one for the strong interaction g_s, one for the electromagnetic interaction e, one for the weak interaction (we can conveniently use the Fermi constant), and the mixing that gives us the physical states, the Weinberg angle. One other unknown parameter in the theory is the mass of the Higgs boson.

As an aid to memory, gluons are flavor blind. They only have color (strong charge). W and Z bosons are color blind, they only see flavor (weak charge). Leptons have flavor but no color, while quarks have both flavor and color (strong and electroweak interactions).

We are now in a position to use the interactions as specified in Section A and to look at the scattering of the constituents under the action of the various forces. That scattering is the subject of discussion in Section B.

B. SCATTERING OF POINT PARTICLES

We begin this Section with a discussion of the pointlike scattering of quarks and leptons. In the second half of this Section we will discuss the distribution of quarks within the hadrons that are the color singlet accessible asymptotic states. A familiar example of the scattering of leptons is the total cross-section for electron-positron scattering into $\mu^+\mu^-$. The cross-section is given in Eq. B.1:

$$\hat{\sigma}(e^+e^- \rightarrow \mu^+\mu^-) = 4\pi\alpha^2/3\hat{s} \qquad \text{(B.1)}$$
$$= 87 \, nb/\hat{s} \, (\text{GeV}^2)$$

A convention that we will adopt is that all elementary process and the kinematic variables associated with them are identified by ($\wedge$). For example, $\hat{\sigma}$ refers to the elementary cross-section and $\hat{s}$ refers to the square of the center-of-mass energy for the fundamental pointlike constituents. The Feynman diagram for this process makes it obvious that $\hat{\sigma}$ is proportional to the coupling constant to the fourth power or α^2. It is also obvious that since there are no other mass scales in the problem the only scale for a cross-section is the energy itself. Numerically this cross-section is 87 nanobarns divided by $\hat{s}$ in GeV^2. This is a typical electroweak cross-section scale.

Another familiar form for lepton scattering is given in Eq. B.2. This is the Rutherford scattering cross-section at low values of the momentum transfer $\hat{t}$. This form corresponds to $d\sigma/d\Omega$ going like $1/(\sin\hat{\theta})^4$.

$$\frac{d\hat{\sigma}(e\mu \rightarrow e\mu)}{d\hat{t}} \simeq 4\pi\alpha^2/\hat{t}^2 \qquad \text{(B.2)}$$

Now let us consider what evidence we have for pointlike quark processes in electromagnetic, weak, and strong interactions. Let's start with the ratio of the

cross-sections for e^+e^- annihilations into hadrons to that for e^+e^- into muon pairs. Drawing a Feynman diagram, the e^+e^- annihilates into a virtual photon. The ratio should just be the ratio of the coupling constant for the photon to quark and antiquark pairs with respect to muon pairs and the sum over the final state colors.

$$R \equiv \frac{\sigma(e^+e^- \rightarrow \text{hadrons})}{\sigma(e^+e^- \rightarrow \mu^+\mu^-)}$$
$$= (\Sigma Q_q^2)N_c \tag{B.3}$$

This means that the R value is just the sum of the squares of the quark charges times the number of colors in the final state. A plot of the measured R value is shown in Fig. B.1. It is clear from this figure that the ratio is essentially constant in between thresholds for production of new heavy quarks. The magnitude of R confirms our assumption that the number of colors is three. There is the famous threshold at the charm-quark mass, another threshold at the b quark mass around the Υ. People are looking at Tristan for the threshold indicating the onset of top anti-top production.
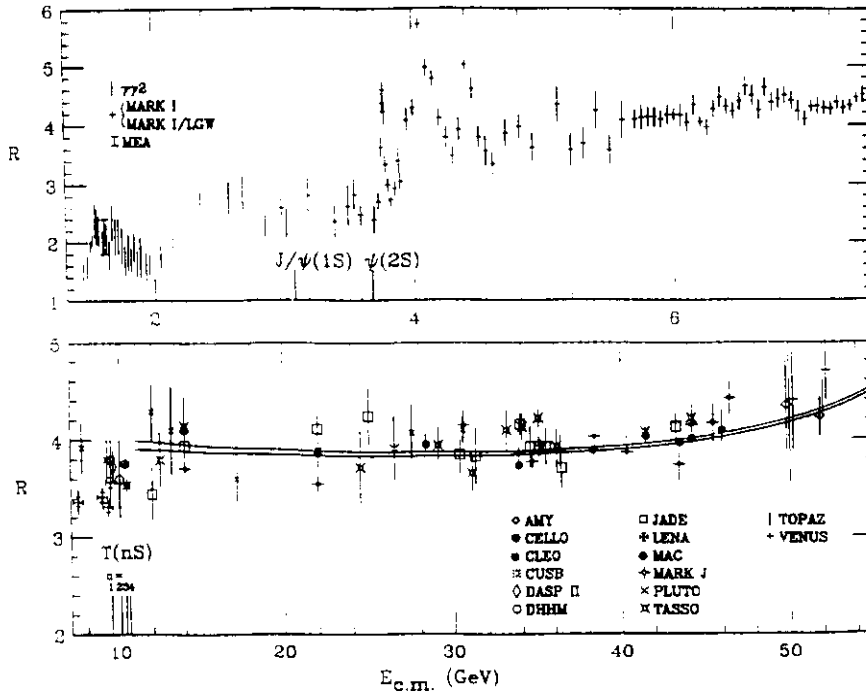

Figure B.1: Pointlike quark behavior in $e^+e^- \rightarrow$ hadrons. $R = \frac{\sigma(e^+e^- \rightarrow h)}{\sigma(e^+e^- \rightarrow \mu^+\mu^-)}$.

14

This data then is a good indication that quarks act like pointlike fermions in electromagnetic interactions. What about the situation in weak interactions? Are the quarks behaving like pointlike objects? Let's start with Eq. B.4.

$$
\begin{aligned}
\sigma(\nu e) &\sim g_W^4 \hat{s}/(\hat{s} + M_W^2)^2 \\
&\to \alpha_W^2/\hat{s} \\
&\to g_W^4 \hat{s}/M_W^4
\end{aligned}
\tag{B.4}
$$

In this case there is a second mass scale, which is the weak boson mass. That mass scale effects the propagator for the virtual W. We have two possible limits for the total cross-section for leptons. There is the high-energy limit, which is that limit wherein we have effectively only one mass scale because the weak boson mass is small. In that case, the limit is essentially that of Eq. B.1. The other limit is at low energies, where in fact the data presently exists. In that case, the propagator is such that the cross-section rises linearly with center-of-mass energy.

$$
\begin{aligned}
\sigma(\nu N) &\sim G^2 \hat{s} \\
\sigma(\nu N)/E_\nu &\sim G^2 M_N \\
&\sim 3 \times 10^{-38} cm^2/\text{GeV} \\
&\sim 0.03 \ pb/\text{GeV}
\end{aligned}
\tag{B.5}
$$

If we identify the fourth power of the electroweak-coupling constant with the second power of the Fermi constant, we can get an estimate for the slope of the neutrino nucleon total cross-section as a function of neutrino energy. We assume that what is happening is that the inelastic scattering between neutrino and nucleon consists of the sum of elastic scatterings off pointlike quarks in the nucleus. Data for this process are shown in Fig. B.2. In fact, the order of magnitude that we've estimated for the process is close to what is actually observed, the scale being $10^{-38} cm^2$ per GeV. We take this magnitude and the linear rise of the cross-section as good evidence that pointlike behavior of quarks in nucleons in electroweak interactions is exhibited.
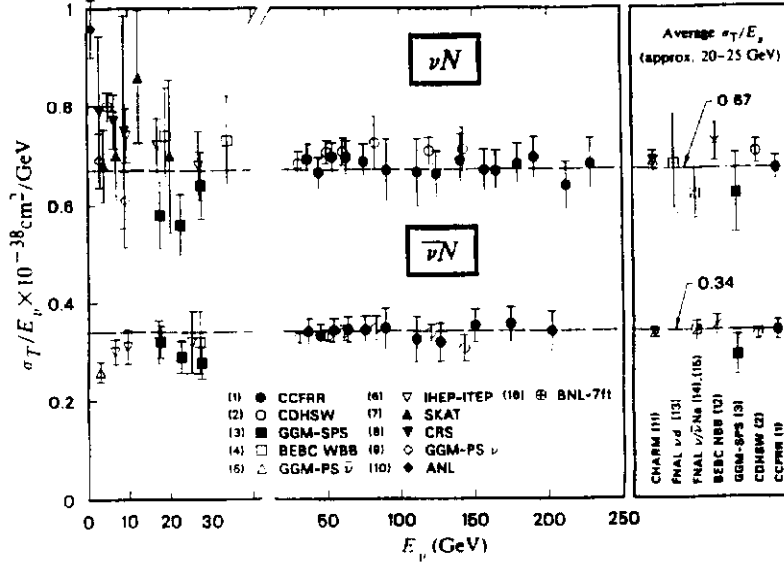
15

Figure B.2: Pointlike quark behavior in νN deep inelastic scattering.

What about in strong interactions? Take the case of inclusive production of pions as a function of transverse momentum. At low transverse momentum there is an exponential dependence which appears to be some sort of collective thermodynamic effect and which dominates the inclusive cross-section. However, at higher values of transverse momentum, say above 3 GeV/c, at the ISR there began to be uncovered a power law behavior of the distribution.

$$\frac{d\sigma}{dp_\perp^2} \sim e^{-bp_\perp} \to \frac{1}{p_\perp^N} \tag{B.6}$$

The ISR data is shown in Fig. B.3. What is happening here is that the exponential behavior is dying off and a pointlike power law behavior (associated with Rutherford type scattering) is being uncovered. This means that the quarks in hadrons also show pointlike behavior through their strong interactions.
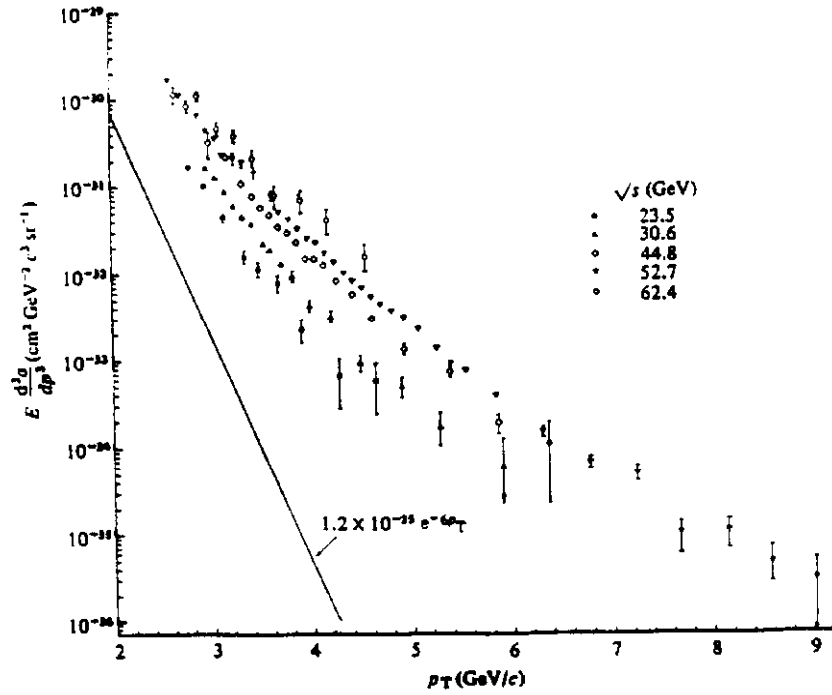
16

Figure B.3: Pointlike quark behavior in high $p_\perp$ π^0 production in pp collisions.

Having convinced ourselves that quarks show pointlike behavior in the same way that leptons do for electromagnetic, weak, and strong interactions we can now turn to the form of the scattering cross-sections. The formulae for two-body scattering processes that are used in this set of lectures and their appropriate Feynman diagrams are shown in Fig. B.4.

PROCESS	DIAGRAMS	$|A|^2$
$q\bar{q} \rightarrow q'\bar{q}'$		$\frac{4}{9}(\hat{t}^2 + \hat{u}^2)/\hat{s}^2$
$qq' \rightarrow qq'$		$\frac{4}{9}(\hat{s}^2 + \hat{u}^2)/\hat{t}^2$
$gg \rightarrow gg$		$\frac{9}{2}\begin{bmatrix} -\hat{t}\hat{u}/\hat{s}^2 - \hat{s}\hat{u}/\hat{t}^2 \\ \\ -\hat{s}\hat{t}/\hat{u}^2 + 3 \end{bmatrix}$
$qg \rightarrow q\gamma$		$\frac{1}{3}\left[\hat{s}/\hat{u} + \hat{u}/\hat{s}\right]$
$gg \rightarrow q\bar{q}$		$\frac{3}{8}(\hat{t}^2 + \hat{u}^2)\left[\frac{4}{9}\left(\frac{1}{\hat{t}\hat{u}}\right) - \left(\frac{1}{\hat{s}}\right)^2\right]$

Figure B.4: Elementary $2 \rightarrow 2$ processes referred to in this note. The appropriate Feynman diagram is included.

18

The column for the amplitude squared has the convention defined in Eq. B.7.

$$\frac{d\hat{\sigma}}{d\hat{t}} \equiv \left[\pi\alpha_1\alpha_2/\hat{s}^2\right]|A|^2 \tag{B.7}$$

What is factored out from the amplitude are the coupling constants at the two vertices and the dimensionally necessary one over $\hat{s}^2$ that one has for the differential cross-section. We can now read off the form of $|A|^2$ from the Feynman diagram. For example, in the process quark anti-quark into quark' anti-quark' we have the one over $\hat{s}^2$ contribution due to annihilation into a virtual photon propagator. This formula is exactly as seen already in Eq. B.1. For the exchange graph, $qq' \to qq'$, the photon propagator gives us a one over $\hat{t}^2$ piece and again this is something we have already seen in Eq. B.2 for differential Rutherford scattering.

There are four terms for the gluon-gluon scattering cross-section. The reason for that is as we said in Section A; gluons are themselves strongly charged and so they self couple into trilinear and quartic vertices. The four terms are easily read off as $1/\hat{s}^2$ (annihilation), $1/\hat{t}^2$ or $1/\hat{u}^2$ (exchange) and 3 (4 gluon vertex). Incidently, the gluon-gluon cross-section at 90^0 is numerically much larger than the other cross-sections given in Fig. B.4. This means that if all else is equal, gluon scattering dominates over say quark scattering or quark anti-quark annihilation.

Gluon quark scattering or gluon anti-quark scattering can lead to direct photon production. In this case we have a fermion propagator whereas in the previous cases we had a boson propagator. That leads to a one over $\hat{u}$ behavior in the elementary processes for exchange or a one over $\hat{s}$ behavior for annihilation. This comparison between fermion and boson propagators in the elementary processes will have implications which we'll see later.

Finally, in heavy quark anti-quark pair production we have gluon-gluon annihilation giving a one over $\hat{s}^2$ propagator plus another Feynman diagram for gluon-gluon fusion with a quark propagator giving one over $\hat{t}$ or $1/\hat{u}$ behavior. The cross-sections for many other elementary processes have been calculated by many authors and they are in the References given in this note.

Going beyond elementary two-body processes we will occasionally need to think

about radiative and other $2 \rightarrow 3$ processes. The Feynman diagrams for fermion scattering (which is a $2 \rightarrow 2$ process) and bremsstrahlung (which is a $2 \rightarrow 3$ process) in a static Coulomb field are shown in Fig. B.5.
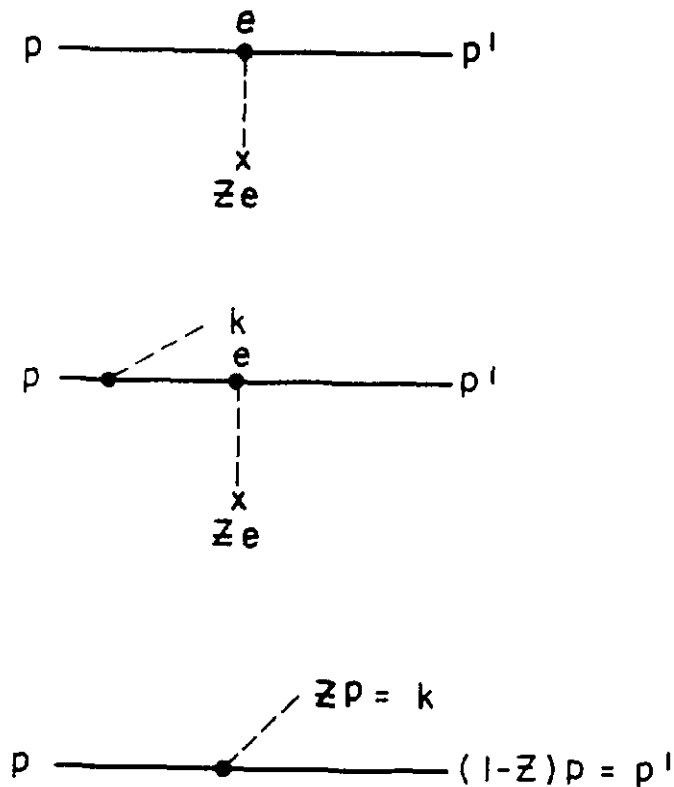

Figure B.5: Diagrams for fermion scattering and bremsstrahlung in a static Coulomb field.

From non-relativistic quantum mechanical perturbation theory we know that the amplitude for a process is proportional to one over the energy difference between the initial and final state for the virtual process. When one evaluates ΔE in the case of bremsstrahlung one finds that the amplitude goes like one over z where z is the momentum fraction carried off by a photon. In the ultrarelativistic limit for the fermions,

$$E = \sqrt{p^2 + m^2} \sim p + m^2/2p$$

$$A \sim 1/\Delta E = 1/(E_i - E_f)$$

$$\Delta E \simeq p^2 + m^2/2p - zp - (1-z)p - m^2/2(1-z)p \qquad \text{(B.8)}$$

$$\sim m^2/2p \left[\frac{z}{1-z} \right]$$

$$A \sim 1/z$$

In order to conserve energy and momentum in a virtual process the thing for the massless photon to do is to be as soft as possible. This gives us the standard radiative behavior that the cross-section goes like one over k, where k is the photon momentum. The complete cross-section for bremsstrahlung, normalized to the $2 \to 2$ process of fermion scattering is given in Eq. B.9:

$$\frac{d\sigma}{d\vec{k}}/\sigma_0 \sim \left(\frac{\alpha}{\pi} \right) \left(\frac{d\Omega_k}{4\pi} \right) \left(\frac{dk}{k} \right) \left[+ \frac{\left(\frac{\vec{\beta}' \cdot \vec{\epsilon}}{1 - \vec{\beta}' \cdot \vec{k}} \right)^2}{\left(\frac{\vec{\beta} \cdot \vec{\epsilon}}{1 - \vec{\beta} \cdot \vec{k}} \right)^2} \right] \qquad \text{(B.9)}$$

Looking at the diagrams in Fig. B.5 it is obvious that this cross-section ratio is proportional to α. The (dk/k) factor for this radiative process has already been explained. Finally, there are some directional factors. They imply that the soft photon is preferentially radiated collinear to the momentum in either the initial or the final state. The directionality can be justified by recalling that in dipole radiation the polarization vector is parallel to the electric field. We know that the electric field impulse of the fast moving particle is perpendicular to its direction of motion. This in turn means that the dipole radiation is transverse to the electric field or parallel to the direction of motion of either the incoming or outgoing fermion. These results are derived in many books on electromagnetism. We will assume that the radiation is collinear in future applications.

Of course, what this means is that if we have a quark or gluon at some particular value of momentum, it will evolve by a cascade process. This is very much in the spirit of electromagnetic cascade development due to bremsstrahlung and pair production. The evolution equations were given in Rossi's classical book on

21

electromagnetic showers many years ago. The gluons being colored can themselves produce pairs of gluons. The quarks can bremsstrahlung a gluon, whereas the gluons can make pairs of quarks and anti-quarks. The diagrams for the evolution of the quarks and gluons by bremsstrahlung, pair production, and triple gluon coupling are shown in Fig. B.6.
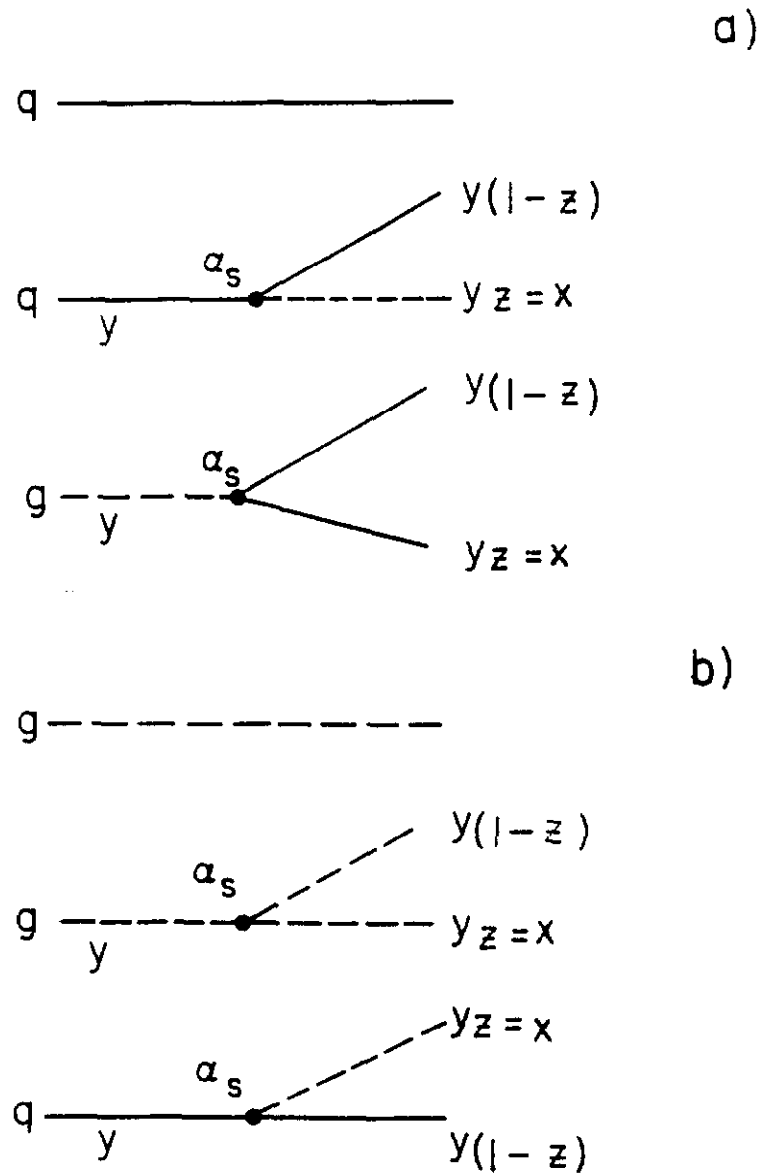

Figure B.6: Diagrams for evolution of quarks and gluons. a) Quarks by bremsstrahlung and pair production, b) Gluons by bremsstrahlung and triple gluon coupling.

The form for the evolution equations of, say, $xg(x)$, follows from our previous derivation, Eq. B.8, of the $1/z$ piece of Eq. B.9. For example, we can read off the contribution to evolution as given in Eq. B.10. The piece due only to low x gluons is shown below:

$$d[xg(x)] \simeq \frac{\alpha_s}{\pi} \int_x^1 dz \left\{ \left[\frac{a}{1-z} + \frac{b}{z} \right] [yg(y)] + \frac{c}{z}[yq(y)] \right\}$$

$$d[xg(x)] \sim \frac{\alpha_s}{\pi} \int_x^1 dz \left(\frac{b}{z} \right) [yg(y)] \qquad \text{(B.10)}$$

$$x = yz$$

If we ignore a possible q^2 evolution of α_s (discussed later), we can do the integral very crudely. At low x values;

$$d[xg(x)] \sim \frac{\alpha_s b}{\pi} \int_1^{1/x} \frac{d(\frac{1}{y})}{(1/y)}[yg(y)]$$

$$\frac{d[xg(x)]}{[xg(x)]} \sim \frac{\alpha_s b}{\pi} d \left[\ln \left(\frac{1}{x} \right) \right] \qquad \text{(B.11)}$$

$$[xg(x)] \sim e^{[(\alpha_s b/\pi) \ln(1/x)]}$$

One can see that the gluon distribution at low x is more divergent than $1/x$ due to a pile-up of gluons at $x = 0$ caused by radiative evolutionary processes. This fact will have some importance in the discussion of "minijets" in Section D.

Now in fact, we are almost always going to assume that if we found the distribution of quarks inside a proton, that distribution is true for all values of momentum transfer. As we have shown, this is not the case. The distribution functions have to evolve because the interactions imply that naive scaling cannot be true. However, since the effects are small and since we are interested in simple order of magnitude hand calculations, we will no longer consider evolution of the distribution functions. For example, from $q = 10$ to $q = 100$ GeV the distribution functions

of quarks varies only by about 20%. There are many uncertainties in hadronic calculations larger than this, so we just ignore evolution.

There is another evolution which is that the coupling constant also depends on the momentum transfer scale. This means that the strong coupling constant α_s "runs" in the sense that it is momentum transfer dependent.

$$\frac{1}{\alpha_s(q^2)} = \left[\frac{(33 - 2N_f)}{12\pi}\right] \ln(q^2/\Lambda^2) \qquad (B.12)$$

$$\begin{matrix} \alpha_s[(10)^2] \sim 0.21 \\ \alpha_s[(100)^2] \sim 0.13 \end{matrix}, \quad \Lambda = 0.2 \text{ GeV}$$

For example, at $(10 \text{ GeV})^2$ α_s is 0.21 where at $(100 \text{ GeV})^2$ it is 0.13, assuming that the Λ parameter is 200 MeV, which is within the range of experimental determinations. Obviously, (see Eq. B.12) Λ is that scale where the strong interactions become strong. The reason for this running of the coupling constant is fairly straightforward to see. A schematic of the evolution of α_s is shown in Fig. B.7.
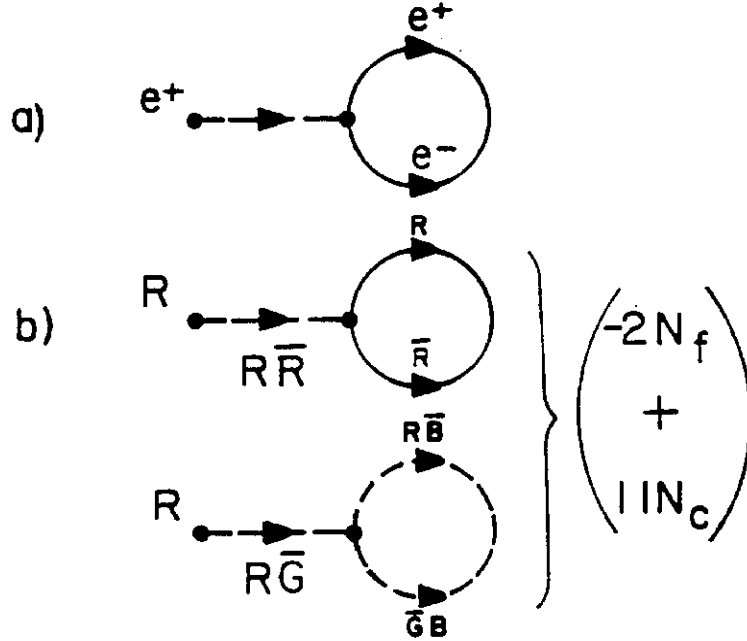

Figure B.7: Schematics for evolution of coupling constants. a) Vacuum polarization, b) Gluons with both fermion and gluon loops.

For photons, we have a vacuum polarization due to the cloud of virtual electron-positron pairs. This process also occurs for gluons making virtual colored pairs of

quarks and anti-quarks. However, gluons themselves (being "charged") can couple to gluon-gluon pairs. This dilutes the effect by carrying color off from the original color source. There is a competition between these two effects. For the appropriate number of fermions, the color dilution factor wins which means that the strong force gets weaker as one looks closer and closer. This behavior is called asymptotic freedom. We'll largely be operating at electroweak mass scales of 100 GeV, so we'll take α_s to be reasonably constant. Since the variation of α_s is logarithmic, and since we are only making hand estimates, it makes sense to also assume a constant strong interaction coupling constant.

Finally, if we are going to look at proton anti-proton collisions we need to specify how the quarks are distributed within the proton. Implicitly, what we are assuming is that we can use an impulse approximation, so there are no quantum mechanical phases involved. This is just a distribution function. Diagrammatically what is happening is that a parton in deep-inelastic scattering has some fraction, ϵ, of the hadron momentum and is scattered by a gauge boson where the distribution function is given by $f(\epsilon)$ as shown in Fig. B.8.

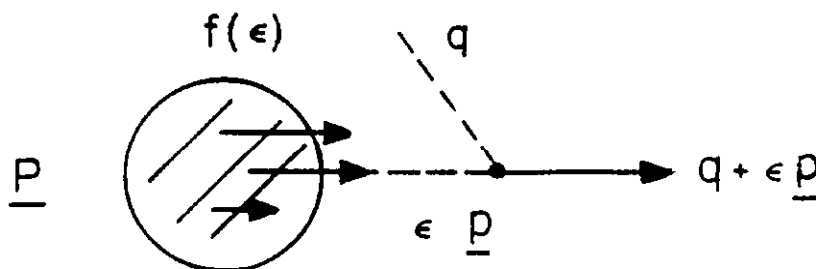Figure B.8: Parton with momentum fraction ϵ of the hadron $\underline{p}$ scatters a gauge boson q. $f(\epsilon)$ is the distribution function of the parton.

If we work out the kinematics for that process as seen in Eq. B.13:

$$
\begin{aligned}
(\epsilon \underline{p} + q)^2 &= m_Q^2 \\
\epsilon^2 M^2 + q^2 + 2\epsilon \underline{p} \cdot q - m_Q^2 &= 0 \\
\epsilon &\simeq \frac{-q^2}{2\underline{p} \cdot q}(1 + m_Q^2/q^2) \\
&\simeq x_{Bj}(1 + m_Q^2/q^2)
\end{aligned}
\tag{B.13}
$$

We can see that if we ignore all mass scales (at high values of q^2), then ϵ is in fact proportional to Bjorken x. Bjorken x is defined to be some function of the two kinematic invariants in the problem. Since these invariants can be determined by only making measurements of the lepton, we can measure the quark momentum distribution by measuring the incoming and outgoing lepton in deep-inelastic scattering. Note that if the quark is not heavy, then Bjorken's x parameter is in fact identically the momentum fraction of the parton in the proton.

The reason we resort to mere data to find this distribution is that it is a non perturbative effect. Hence, at the moment, it is uncalculable although it is in principle a solvable problem in quantum chromodynamics. However, since the coupling constant becomes large at low values of q^2 (characterized by the 200 MeV value for Λ), perturbative calculational techniques break down. For the moment we will simply take the distribution functions as found from the deep inelastic scattering of electrons, muons, and neutrinos on nucleons. These distributions are shown in Fig. B.9.
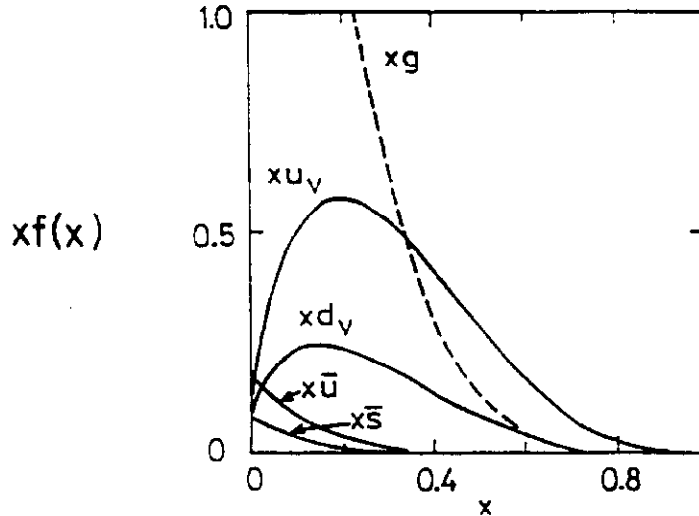

Figure B.9: Parton momentum distribution functions for the proton, $xf(x)$.

If there were three and only three valance quarks in a proton, we would expect the distribution function to be a δ function at an x value of 1/3. However, there are radiative processes where the valance quark could radiate a gluon. Due to momentum conservation this interaction lowers the average value of the x of the

valance quarks below 1/3. There are also higher order processes where a gluon radiates and before it is reabsorbed a quark anti-quark virtual pair materializes. Hence, there are anti-quarks in a proton. These are called the sea distributions. We use a parameterization of the momentum fraction, $xf(x)$ to be a power law in x times a power law in $(1-x)$:

$$
\begin{aligned}
xf(x) &= ax^\alpha(1-x)^\beta \\
xu_v(x) &\simeq 1.8\sqrt{x}(1-x)^3 \\
xd_v(x) &\simeq 0.7\sqrt{x}(1-x)^4 \\
x\bar{u}(x) &= x\bar{d}(x) = 2x\bar{s}(x) \\
&\sim 0.2(1-x)^8
\end{aligned}
\tag{B.14}
$$

There are two valance up quarks and one valance down quark in the proton. Their average x value is somewhat less than 1/3. The sea quark distributions have a number density proportional to one over x, as we expect for objects which are radiatively created. $f(x)$ is defined to be a distribution function, which means that $f(x)dx$ is the number of partons between x and $x + dx$. Since we know that x is also the momentum fraction, $xf(x)dx$ is the momentum distribution of partons between x and $x + dx$.

The gluon exists in the hadron only due to a radiative process. It therefore has a number distribution which goes as one over x just as the sea partons do. In particular, we know from deep inelastic scattering that the quarks account for only half of the momentum carried by the proton. The rest is neutral and is not seen in electromagnetic scattering. Hence the neutral gluons have a momentum distribution which is normalized to 1/2.

$$
\begin{aligned}
xg(x) &= 7/2(1-x)^6 \\
\int xg(x)dx &\equiv 1/2
\end{aligned}
\tag{B.15}
$$

It is obvious from the distribution functions that the number of radiative sea partons is infinite; there are an infinite number of soft partons. This is exactly the same situation (for the same reason); there are an infinite number of soft photons in a radiative process. On the other hand, the number of valance quarks is finite and the sum of up plus down number distributions is equal to three. That is

27

the valance quark sum rule. We will use these distribution functions in all our subsequent calculations where we will assume that they have not evolved in any way.

Given that there are partons distributed in the proton, we need not only the distribution functions but we need to relate the kinematics of the subprocess to that of the hadron-hadron scattering. The kinematics are illustrated in Fig. B.10.
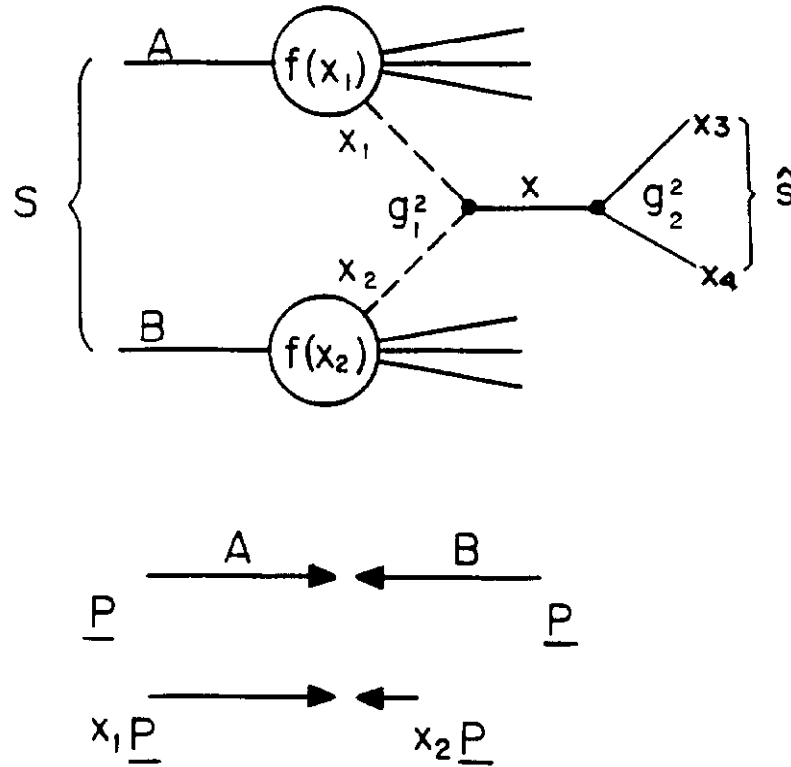

Figure B.10: Kinematics of parton-parton processes in hadron-hadron collisions.

A parton with momentum fraction x_1 from hadron A (with some distribution function) and a parton with momentum fraction x_2 from hadron B scatter into a system with sub mass $\hat{s}$ and momentum fraction x.

$$s = (p_A + p_B)^2 \sim 4p_A p_B \sim 4\underline{p}^2$$

$$\hat{s} \sim 4p_1 p_2 \sim 4x_1 x_2 \underline{p}^2 \sim x_1 x_2 s$$

$$x \equiv 2p_{11}^\star/\sqrt{s} = 2(x_1 - x_2)\underline{p}/\sqrt{s} \qquad \text{(B.16)}$$

$$= x_1 - x_2$$

$$\tau \equiv \hat{s}/s = x_1 x_2$$

It is fairly easy to see from the kinematics that x_1 and x_2 are tagged by the two-body mass $\hat{s}$ and the Feynman x value of the produced system. We define a parameter τ which is the ratio to the sub energy of the partonic process to the total center-of-mass energy of the hadronic process. We will see in Section C that $\sqrt{\tau}$ is, as a rule of thumb, a typical x value for the parton (see also Eq. B.16).

The final state orientation is characterized by some scattering angle $\hat{\theta}$ through the Lorentz invariants $\hat{t}$ or $\hat{u}$. The initial state x and mass are specified by x_1 and x_2, while the final state is determined by the two-body scattering angle $\hat{\theta}$.

$$\hat{t} = (p_3 - p_1)^2$$

$$\sim -2p_1 p_3(1 - \cos\hat{\theta})$$

$$\sim -\hat{s}/2(1 - \cos\hat{\theta}) \qquad \text{(B.17)}$$

$$\hat{u} = (p_3 - p_2)^2$$

$$\sim -\hat{s}/2(1 + \cos\hat{\theta})$$

Assuming no intrinsic transverse momentum for the quarks, the final state kinematics are such that x_3 and x_4 are back-to-back in azimuth but not in polar angle. We know that confinement means that intrinsic transverse momenta of scale $\sim \Lambda$ must exist. We will ignore this in all that follows, and almost always deal with scales $>> \Lambda$. One can think of a particle of mass $\sqrt{\hat{s}}$ and momentum x decay with angle $\hat{\theta}$. It is easy to see that γ and β of this particle in the $\bar{p}p$ center-of-mass frame are:

$$\gamma = (x_1 + x_2)/2\sqrt{\tau} \qquad \text{(B.18)}$$

$$\beta = (x_1 - x_2)/(x_1 + x_2)$$

29

After the "decay," the daughters have $p_\perp = (\frac{\sqrt{\hat{s}}}{2})\sin\hat{\theta}$ and longitudinal momentum $x_3\atop 4$.

$$x_{3\atop 4} = \frac{1}{2}\left[(x_1 - x_2) \pm \cos\hat{\theta}(x_1 + x_2)\right] \tag{B.19}$$

$$\tan\theta_{3\atop 4} = 2\sqrt{\tau}\sin\hat{\theta}/x_{3\atop 4}$$

For example, at a mass of 400 GeV in 2 TeV $\bar{p}p$ collisions, $x_1 = x_2 = 0.2$ at $x = 0$. Then $\theta_{34} = 180^0 = \hat{\theta}_{34}$. However at $x = 0.3$, $x_1 = 0.4$, $x_2 = 0.1$ and $\theta_{34} = 106^0$ (if $\hat{\theta} = 90^0$). These kinematic relations are useful in finding jet-jet angular distributions and the like. In Section D, we will assume that $\hat{\theta}$ can be extracted from energy and angle measurements of the jets.

In this Section, we have discussed the pointlike behavior of quarks as seen in electromagnetic, weak, and strong interactions. We have also tabulated the $2 \to 2$ processes which will be used in discussing $\bar{p}p$ interactions and have briefly touched on $2 \to 3$ radiative processes using the well known electromagnetic process of bremsstrahlung as a paradigm. Lastly, we have discussed the number density distribution of the quarks and gluons which will be used in subsequent Sections. The basic kinematics relating parton-parton processes to hadron-hadron processes have been outlined. These first two Sections give us all the tools that we need to go forth and estimate proton anti-proton collider physics processes.

C. HADRON-HADRON PRODUCTION OF PARTICLES

Since we now know that specification of x_1 and x_2 defines the initial state, it is clear that the hadron-hadron cross-section is just the joint probability for a parton in hadron A and a parton in hadron B times the partonic cross-section. The probability is just the number distribution $f(x)dx$ which gets us the probability of a parton having an x between x and $x + dx$.

$$d\sigma = P_A P_B d\hat{\sigma} = C\ f(x_1)\bar{f}(x_2)dx_1 dx_2 d\hat{\sigma} \tag{C.1}$$

$$P(x_1) \equiv \sqrt{C}f(x_1)dx_1$$

There is also a color factor, C, which takes into account the fact that all possible colors of quarks and gluons within a proton exist, but that asymptotic freedom

tells us that color is absolutely bound so that the asymptotic hadron states need
to be colorless. We are only allowed certain combinations of partons from hadron
A and partons from hadron B. This color factor for quarks is shown in Fig. C.1;
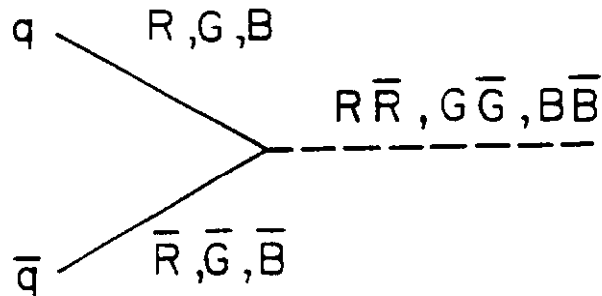for quarks $C = 3$, while for gluons C is clearly $= 8$.

Figure C.1: Color factor for colored quark and antiquark fusing into a colorless
final state.

For convenience we will write the differential cross-section not in terms of x_1
and x_2 to specify the initial state, but in terms of rapidity and invariant mass.
Using the relationships that we derived in Section B, it is simple to write down the
Jacobean relating those two quantities. In fact, the differential element $dx_1 \, dx_2$ is
just $d\tau dy$.

$$
\begin{aligned}
x &\equiv 2p_{11}^{*}/\sqrt{s} = 2M_\perp \sinh(y)/\sqrt{s} \\
dx_1 dx_2 &= \left(\frac{d\hat{s}}{s}\right) dy = d\tau dy \\
d\sigma &= C f(x_1)\bar{f}(x_2) d\tau dy d\hat{\sigma}
\end{aligned}
\tag{C.2}
$$

In most of what we do we will use the differential cross-section at rapidity
value of zero, which is 90^0 in the center-of-mass frame. The equations simplify in
that case and what we are looking for is a simple straight forward evaluation of
the relevant formula. Note that, most cross-sections are on a "rapidity plateau,"
where the maximum value of the cross-section occurs at $y = 0$.

31

$$x_1 x_2 \;=\; \tau$$
$$x_1 - x_2 \;=\; x \qquad\qquad (C.3)$$
$$x_1 = x_2 \;=\; \sqrt{\tau} = M/\sqrt{s} = \sqrt{\hat{s}/s}\ \Big|_{y=x=0}$$

At rapidity 0, x_1 is equal to x_2 which makes the differential cross-section particularly simple.

$$\left(\frac{d\sigma}{dy\,d\tau}\right)_{y=0} \;=\; C f(\sqrt{\tau})\bar{f}(\sqrt{\tau})\,d\hat{\sigma} \qquad\qquad (C.4)$$

Note that in Eq. C.4 there is an implicit sum over all possible partons in hadron A and hadron B which can contribute to the process which is schematically indicated by $d\hat{\sigma}$. Rearranging Eq. C.4, we can get the expression given in Eq. C.5.b where the left-hand side is dimensionless. The right-hand side depends only on the source distributions of partons in the hadron, color factors, and the coupling constants, because (recall Section B) $d\hat{\sigma}$ is by dimensional arguments proportional to $1/\hat{s}$.

$$a) \qquad \left(\frac{d\sigma}{dy\,d\hat{s}}\right)_{y=o} \;=\; C[xf(x)x\bar{f}(x)]_{x=\sqrt{\tau}}(d\hat{\sigma}/\hat{s})$$

$$\qquad\qquad\qquad\qquad\qquad\qquad\qquad\qquad (C.5)$$

$$b) \qquad M^3 \left(\frac{d\sigma}{dy\,dM}\right)_{y=0} \;=\; 2C\left[xf(x)x\bar{f}(x)\right]_{x=\sqrt{\tau}}[d\hat{\sigma}\hat{s}]$$

In this Section, we will concentrate on particle production. We are thinking of parton-parton formation of a resonance specified by a central mass M and width Γ. If you recall from elementary books on quantum mechanics, a finite lifetime of a state implies that the Fourier transform has a Brite-Wigner form in the energy domain. In particular, since unitarity requires that the cross-section in some particular partial wave be limited:

$$\hat{\sigma} \;<\; 4\pi\,\lambda^2(2J+1)$$
$$\int \hat{\sigma}\,d\hat{s} \;=\; \pi^2(2J+1)(\Gamma/M) \qquad\qquad (C.6)$$
$$d\hat{\sigma} \;\sim\; \pi^2(2J+1)(\Gamma/M)\delta(\hat{s}-M^2)$$

32

Integrating the Brite-Wigner shape one gets an inverse tangent function for a nonrelativistic Brite-Wigner because one goes once around the Argand diagram. The integral over all center-of-mass energies is given in Eq. C.6. If the width of the resonance is narrow with respect to its central mass value, we can replace the Brite-Wigner form (which has a full width of Γ) by a δ function in energy space. The constants are chosen so as to give the same integral value over all center-of-mass energies. In this narrow width approximation we can integrate the double differential cross-section given in Eq. C.5 over all values of $\hat{s}$. The result is given below.

$$\left(\frac{d\sigma}{dy}\right)_{y=0} = C\left[xf(x)x\bar{f}(x)\right]_{x=\sqrt{\tau}}\left[\frac{\pi^2\Gamma_{ff}(2J+1)}{M^3}\right] \qquad (\text{C.7})$$

$$\Gamma_{gg} \rightarrow \Gamma_{q\bar{q}}(4/3)$$

It seems clear that the cross-section should be proportional to the formation width Γ_{ff}. C is the color factor relevant to the source functions specified by $f(x)$. The width in Eq. C.7 refers to the partial width for formation by the sources indicated by f and $\bar{f}$. There is also a spin sum over initial states and a spin average over final states which leads to a factor of 4/3 if the sources are quarks with respect to a factor of 1 if these sources are gluons.

We define a dimensionless luminosity, L, such that the scaled cross-sections, i.e. dimensionless quantities, are particularly simple. The luminosity absorbs all the source distributions leaving only the elementary couplings.

$$L \equiv C[xf(x)x\bar{f}(x)]_{x=\sqrt{\tau}} \qquad (\text{C.8})$$

Then one finds that, if $d\hat{\sigma} \sim \pi(\text{``}\alpha\text{''})^2/\hat{s}$ or if $\Gamma \sim (\text{``}\alpha\text{''})M$ the formulae are very simple.

$$a) \qquad M^4\left(\frac{d\sigma}{dM^2dy}\right)_{y=0} = L(d\hat{\sigma}\hat{s})$$

$$\sim L[\pi(\text{``}\alpha\text{''})^2]$$

$$(\text{C.9})$$

$$b) \qquad M^2\left(\frac{d\sigma}{dy}\right)_{y=0} = L\left[\pi^2(2J+1)\frac{\Gamma}{M}\right]$$

$$\sim L[\pi^2(2J+1)\text{``}\alpha\text{''}]$$

33

These are our two basic formulae which we will apply over and over again in different formation and scattering applications.

When one wants to estimate the total cross-section and not just the differential cross-section we can use the definitions of rapidity given in Eq. C.2. We estimate the rapidity range for a given mass when the limit in x of $\pm\,1$ is reached. The quantity Δy is roughly the width of the rapidity "plateau."

$$x = \pm 1, \; x \sim (M/\sqrt{s})e^y, \; y = \pm \, \ln(\sqrt{s}/M) \qquad (C.10)$$
$$\Delta y \sim 2 \, \ln(\sqrt{s}/M) = 2 \, \ln(1/\sqrt{\tau})$$

Using Eqs. C.9 and C.10, one can make the crude assumption that the cross-section is just $(d\sigma dy)_{y=0}$ times the allowed kinematic range Δy, i.e., the value on the plateau times the width of the plateau.

$$\sigma \sim \left(\frac{d\sigma}{dy}\right)_{y=0} \Delta y \qquad (C.11)$$
$$\sim \left(\frac{\Gamma}{M^3}\right)\left[\pi^2(2J+1)2 \, \ln\left(\frac{1}{\sqrt{\tau}}\right)\right] L$$

The first thing we notice looking at Eq. C.11 is that we can predict a scaling behavior. The quantity $M^3\sigma/\Gamma$ should be a function only of the parameter τ. In order to test this scaling prediction and also the absolute value of the cross-section shown in Eq. C.11 we plot in Fig. C.2 the cross-section for the production of vector mesons in pp collisions.
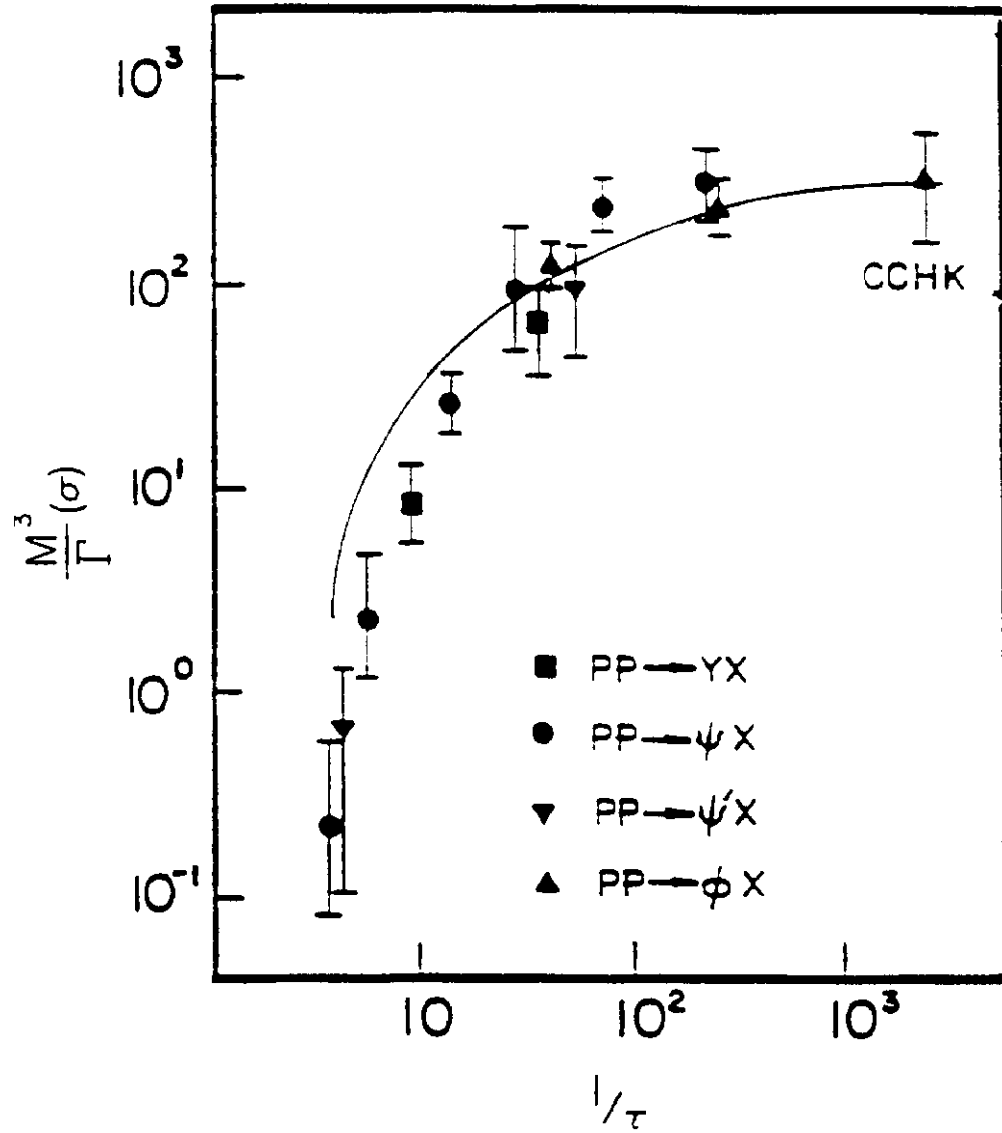
Figure C.2: Scaling behavior in pp production of vector mesons. The smooth curve is the hand estimate.

In this case, we use Eq. C.12 which explicitly assumes gluon-gluon formation of these resonances.

$$\sigma \sim \left(\frac{\Gamma}{M^3}\right) \left[\frac{\pi^2(2J+1)}{4} \ln\left(\frac{1}{\sqrt{\tau}}\right)\right] \left[\left(\frac{7}{2}\right)\left(1 - \sqrt{\tau}\right)^6\right]^2 \qquad \text{(C.12)}$$

Obviously, the scaling prediction is well verified. In particular, assuming gluons as the source functions, we reproduce the threshold behavior of the processes very well. In these excitation curves, increasing s at fixed M means decreasing τ. Since

35

$\sqrt{\tau} \sim x_1 \sim x_2$, decreasing $\sqrt{\tau}$ means decreasing x or increasing source luminosity. Hence, the rapid rise. Last, but not least, the absolute value of the cross-sections is very nicely reproduced using the distribution functions which we have taken for the gluons.

This correspondence of the simple estimate with the data is very encouraging and leads us to go on and try to apply these formulae to other processes. In particular, we know that heavy quark-antiquark bound systems couple to two and three gluons. For example, the η_c coupling to two gluons means that η_c will have a shorter lifetime than the ψ, just as is the case for ortho and para positronium. Therefore the η_c should have a larger width by something roughly like the strong coupling constant. Hence it will be more copiously produced since the production cross-section is proportional to Γ.

$$\eta_c \rightarrow gg$$
$$\psi \rightarrow ggg \tag{C.13}$$
$$\Gamma_{\eta_c} > \Gamma_\psi \sim \Gamma_{\eta_c}(\alpha_s)$$

A complete calculation of the predicted $\bar{p}p$ cross-sections of quarkonium bound states vs. center-of-mass energy is shown in Fig. C.3.

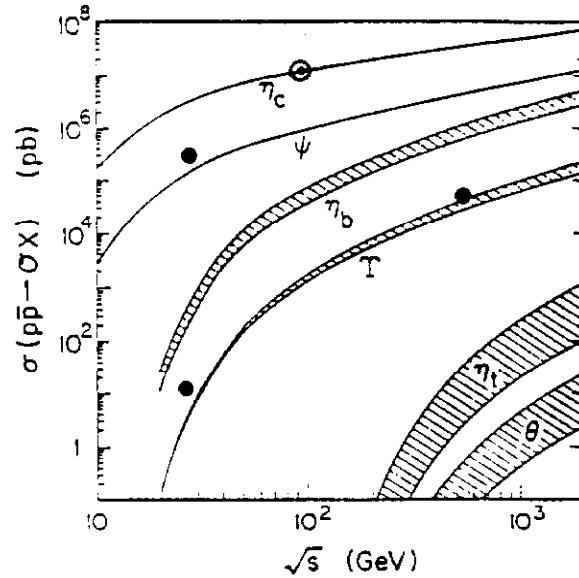Figure C.3: Predicted $\bar{p}p$ cross-sections for $(Q\bar{Q})$ bound states vs c.m. energy $\sqrt{s}$. The point, $\odot$, is a hand estimate, while the points, $\bullet$, are 400 GeV pp data and UA1 data.

For comparison one can use Eq. C.12 as a hand estimate of η_c production at a center-of-mass energy of 100 GeV. The result is a cross-section of 11 microbarns.

$$\eta_c :$$
$$\sqrt{s} \;=\; 100 \text{ GeV}, \; \sqrt{\tau} = 0.03$$
$$\Gamma \;\sim\; 10 \text{ MeV}, \; \Delta y \sim 7 \qquad\qquad (\text{C.14})$$
$$\sigma(\eta_c) \;\sim\; 11 \; \mu b$$

This hand estimate is also indicated in Fig. C.3 and is in good agreement with the exact predictions. We again have a steeply rising curve due to the fact that at fixed mass, larger $\sqrt{s}$ means smaller x and hence higher luminosity L.

If the widths are the same, since Δy is only logarithmically dependent on τ, we expect that the η_c to η_b cross-sections, at very high energies, are in the ratio of the cube of their masses. Note also that ψ production is suppressed relative to η_c production. The essential reason is that the formation width is larger for the η_c than the ψ. The η_c couples to two gluons while the ψ (because of C number conservation) must couple to three gluons. The 400-GeV pp data which is plotted on this graph seems to confirm this suppression of ψs, although η_c production has not yet been observed. Extrapolating using Eq. C.12 to the Fermilab Collider at center-of-mass energy of 2 TeV, one expects the η_c cross-section to be about 80 microbarns and the η_b cross-section to be about 3 microbarns. Certainly these are all large cross-sections.

At the CERN Collider, in the UA1 experiment, both ψs and Υs have been seen in events with isolated dimuons. However the trigger requires high $p_\perp$, which causes a large reduction of the cross-section. The data is hence difficult to absolutely normalize so as to check the cross-section predictions for ψ and Υ at higher collider energies. Within large errors, it does appear that these cross-sections are consistent with the predictions. One can consider that agreement as weak confirmation of the predictions shown in Fig. C.3.

We now move on to the production of the W and Z gauge bosons in proton antiproton collisions. The coupling of the Ws to fermions and leptons was discussed in

Section A along with the KM matrix. A rough approximation to that matrix (with a Cabbibo angle of about a fifth) was also given in Section A. Adapting the color factor of 1/8 in Eq. C.9 to that for quark anti-quark production and the spin sum for the formation width we get the expression given in Eq. C.15 for the differential production cross-section for vector bosons formed in quark anti-quark collisions.

$$(C.9) \rightarrow$$

$$
\begin{aligned}
\left(\frac{d\sigma}{dy}\right)_{y=0} &= \frac{1}{3}\left[xq(x)x\bar{q}(x)\right]_{x=\sqrt{\tau}}\left[\frac{4\pi^2\Gamma_{q\bar{q}}(2J+1)}{3M^3}\right] &\quad (C.15)\\
&= L_{q\bar{q}}\left[\frac{4\pi^2\Gamma(W \rightarrow q\bar{q})}{M^3}\right]
\end{aligned}
$$

We clearly need the width for quark anti-quark coupling to the gauge bosons. In Section A, we noted on dimensional grounds (and on the grounds of electroweak unification) that the width would be dominated by quark anti-quark decays due to the color factors. It should be of order α times the mass of the bosons. The exact result for the partial width will merely be quoted in Eq. C.16. The amplitude is proportional to the coupling constant times the quark coupling matrix. The dynamics is that the vector boson polarization is dotted into the leptonic final state current.

$$
\begin{aligned}
A &\sim g_W V_{q\bar{q}} \vec{\epsilon}_W \cdot \vec{J}^\ell \\
\Gamma &\sim g_W^2 M, \\
\Gamma(W \rightarrow e\nu) &= \frac{\Gamma(W \rightarrow u\bar{d})}{3} &\quad (C.16)\\
&= \left[\frac{g_W^2}{48\pi}\right]M_W = \left[\frac{GM_W^3}{6\sqrt{2}\pi}\right] = \left[\frac{\alpha_W}{12}\right]M_W \\
&\sim 1/3 \text{ GeV}
\end{aligned}
$$

Indeed the width is proportional to the weak coupling constant squared times the mass of the W. The partial widths for quark decays relative to leptonic decays are in the ratio of 3 to 1 due to the color factors.

The way that the leptons from the decay of the produced W are detected is to use the Jacobean peak method. One assumes that there is no intrinsic parton transverse momentum, so that the $\bar{u}$ and d fuse into a W boson with no transverse momentum. That means the scale of transverse momentum in the final state is naturally that of the mass of the W itself.

$$\hat{p}_\perp^2 = \frac{\hat{s}}{4}\sin^2\hat{\theta} \sim p_\perp^2$$

$$d(\hat{p}_\perp^2) = \frac{\hat{s}}{2}\cos\hat{\theta}d(\cos\hat{\theta}) \qquad (C.17)$$

$$\hat{p}_\perp = M/2$$

At 90° in fact the transverse momentum is equal to half the mass of the W. The distribution of transverse momentum peaks at 90°. This is a very strong peak, $1/\cos\hat{\theta}$, which is washed out only by the transverse momentum of the parent quarks or by initial state radiation. UA1 data from CERN on the Jacobean peak for electrons is shown in Fig. C.4. Indeed there is a very strong peaking at about half the W mass. We can take this data as a posteriori justification for the neglect of "intrinsic" transverse momentum of the partons.
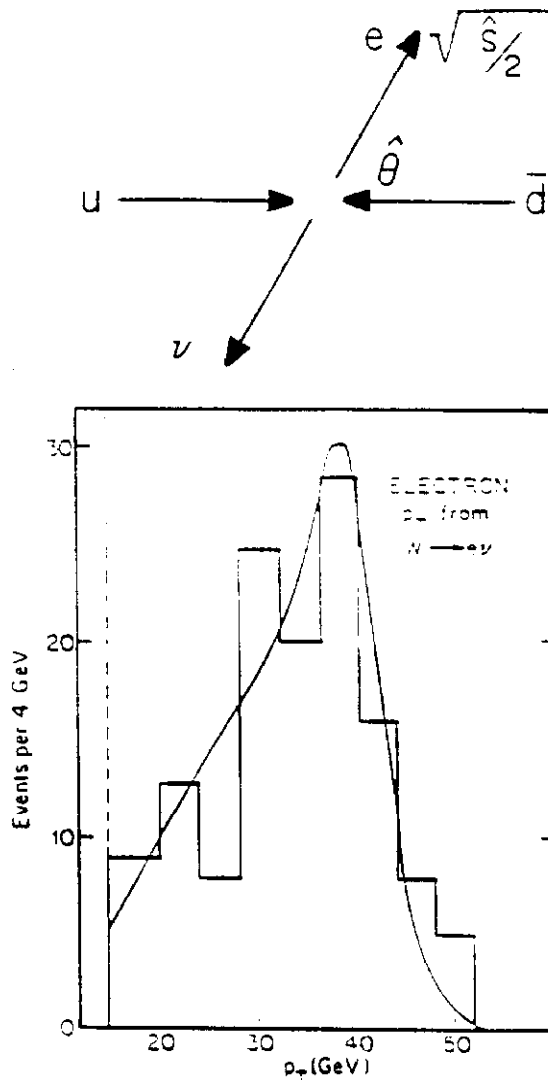
Figure C.4: Jacobean peak in UA1 data for electrons.

The W was observed at CERN in data samples with isolated leptons accompanied by large missing transverse momentum indicating that a neutrino had carried off momentum outside of a hermetic detector. By comparison, the Z boson was found by calculating the invariant mass of isolated dielectrons. Data from UA1 is shown in Fig. C.5. The background in Fig. C.5 comes from a process (called Drell-Yan) which will be discussed in Section D.
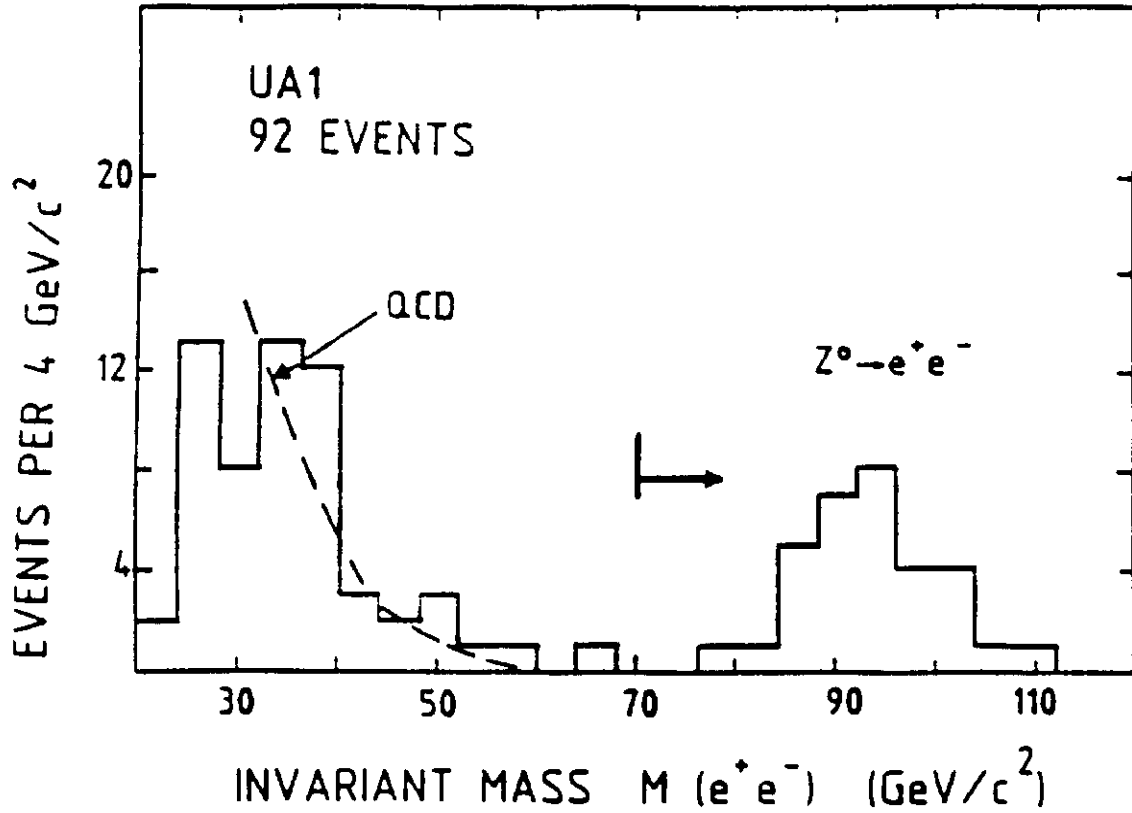
Figure C.5: Dielectron invariant mass, UA1 data.

The masses of both the W and Z were predicted before their discovery. If we look back at Eqs. A.4 and A.8 we see that the W mass is proportional to the coupling constant times the vacuum expectation value. You remember that the vacuum expectation value was evaluated in terms of the Fermi constant. The coupling constant in turn was unified to be proportional to the electromagnetic coupling constant. Therefore, the only thing that was left was the Weinberg angle of rotation. That angle was measured in weak neutral-current interactions in neutrino scattering (see Eq. A.5 and Fig. A.2) to have a value, $\sin^2 \theta_W$ roughly 1/5. Therefore the masses were predicted and their subsequent confirmation was a great triumph for the Standard Model. The width, Γ_Z would tell us the number of light neutrino generations. Until now, the measurements of Γ_Z (see Fig. C.5) have been dominated by experimental errors.

Let's turn our attention now to the cross-section for production and decay of the W bosons. Color counting of the Cabibbo allowed elements of the KM mixing

41

matrix lead us to estimate that the branching ratio into electron plus neutrino is about 1/9.

$$\frac{1}{e\nu_e} \quad : \quad \frac{1}{\mu\nu_\mu} \quad : \quad \frac{1}{\tau\nu_\tau} \quad : \quad \frac{3}{u\bar{d}} \quad : \quad \frac{3}{c\bar{s}} \qquad \qquad \text{(C.18)}$$
$$B \sim 1/9$$

This leads us to a crude estimate (see Eq. C.15) of the cross-section times branching ratio given below.

$$\sigma B \quad \sim \quad \frac{4\pi^2 \Gamma(W \to u\bar{d})}{3M^3} \left(\frac{1}{9}\right) = 1.1 \; nb \qquad \qquad \text{(C.19)}$$

The scale at Tevatron energies is clearly nanobarns. In looking at the threshold behavior for W boson production we use the differential cross-section at $y = 0$ from Eq. C.15, the rapidity interval from Eq. C.10, the width from Eq. C.16, and the branching ratio from Eq. C.18. Putting all this together we still have different source functions. There are valance-valance interactions for W^-, $\bar{u}$ from the anti-proton and a d from the proton. There are also valance sea and sea-sea interactions which obviously become more important at higher energy where the τ value is small. Very near threshold, the valance quarks will dominate since the τ value is large.

$$
\begin{aligned}
xu_v x d_v &\sim \sqrt{\tau}(1 - \sqrt{\tau})^7 & \text{vv} \\
xu_v x\bar{d} &\sim (\tau)^{1/4}(1 - \sqrt{\tau})^{11} & \text{vs} \\
x\bar{u} x\bar{d} &\sim (1 - \sqrt{\tau})^{16} & \text{ss}
\end{aligned}
\qquad \qquad \text{(C.20)}
$$

These various hand estimates of the cross-section are given in Table C.1.

Table C.1.
Hand estimated cross-sections for W
production at 3 values of $\sqrt{s}$.

$\sqrt{s}$(TeV)	$\sqrt{\tau}$	Δy	$\sigma B(nb)$			
			vv	vs	ss	Total
0.5	0.16	3.6	0.50	0.17	0.09	0.52
1.0	0.08	5.0	0.63	0.42	0.11	1.20
2.0	0.04	6.4	0.55	0.63	0.29	1.50

The data and "exact" predictions are shown in Fig. C.6 along with the hand estimates. Clearly the hand estimates work fairly well and there is a complicated energy dependence between the CERN experiments and the Tevatron. In the UA experiments, it is clear that one is dominated by valance-valance whereas at the Tevatron valance-sea is certainly of comparable importance and the sea-sea contribution is rising very rapidly. It is also clear that the absolute value of σB is reasonably well predicted by the hand estimates and is in plausible agreement with the actual data points.
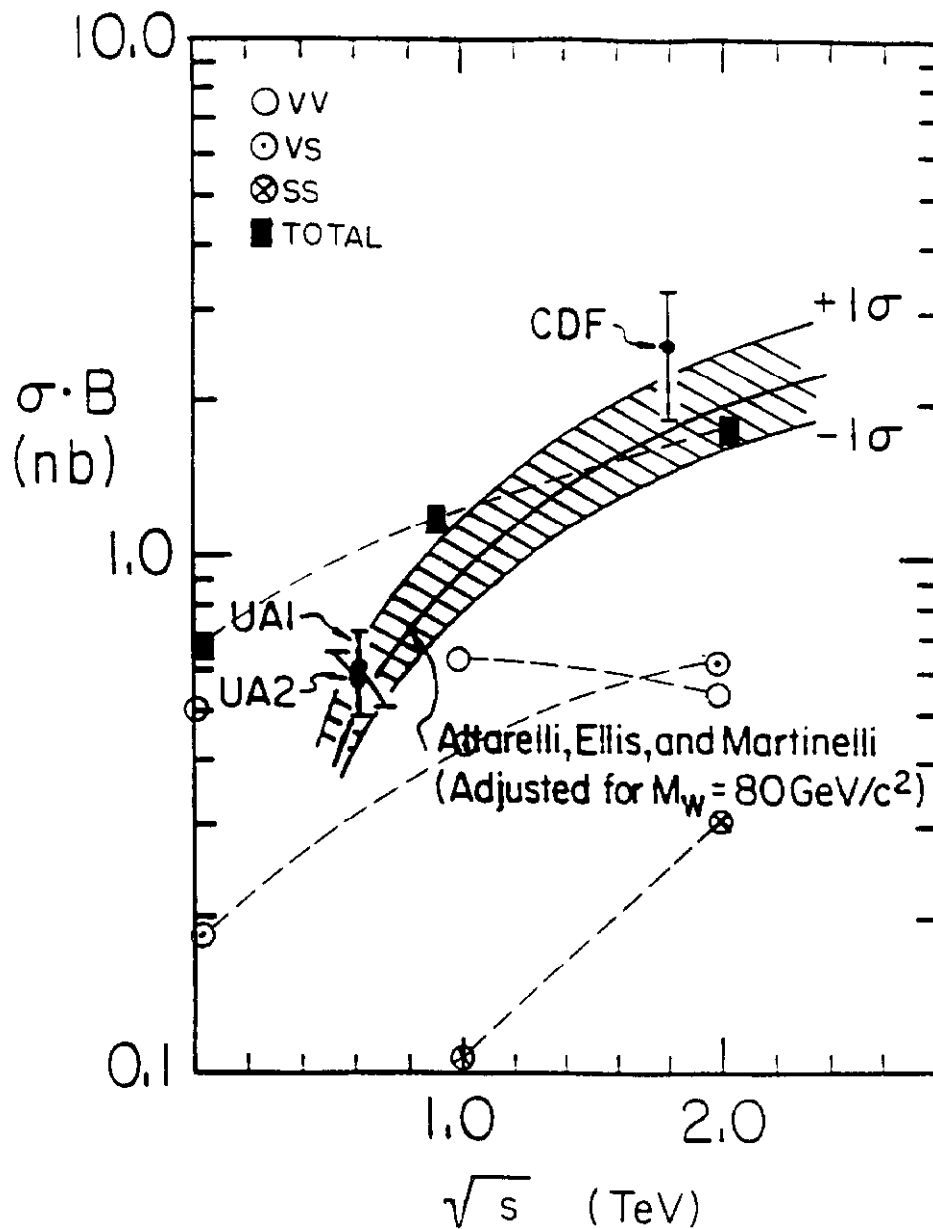
Figure C.6: Data from UA1, UA2, and CDF along with estimates from Table C.1.

Consider now the angular distribution of the leptons in the decays of W bosons. You recall that in the electroweak theory we put in the V-A structure essentially by hand. That structure forces fermions to be left-handed and anti-fermions to be right-handed. Thus, quarks are left-handed, anti-quarks are right-handed, elec-

trons are left-handed, positrons are right-handed, anti-neutrinos are right-handed and neutrinos are left-handed. The data from UA1 on the angular distribution of the decays is shown in Fig. C.7. Also shown in that figure is the helicity structure of valance-valance production. If valance-valance scattering dominates (as it does from our expectations of hand estimates) then we find that positrons preferentially go in the anti-proton direction and electrons go in the proton direction. The data is not only a confirmation of the V-A structure of the charged-weak interactions but is confirmation of the valance-valance character of W production at the CERN Collider.
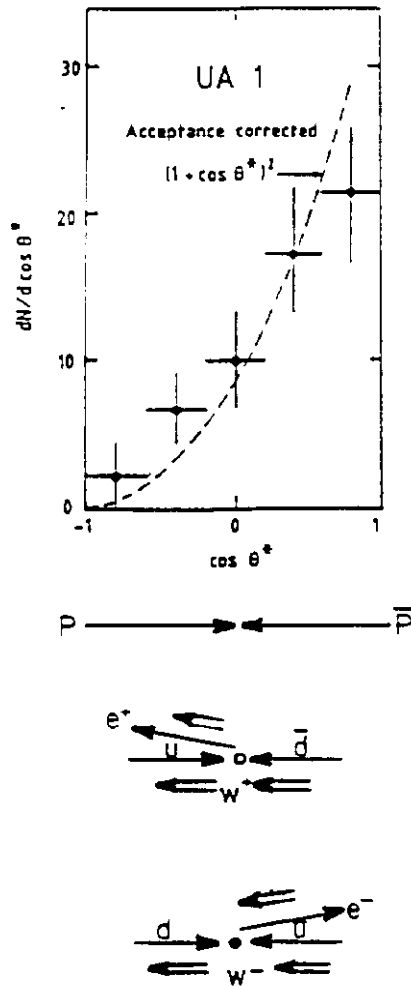
Figure C.7: UA1 data on the angular distribution of $W \to e\nu$ decays.

Another observable in W production is the x distribution. We have two equations relating x_1 and x_2 to the Feynman x and the mass of the system. We can

invert those equations and solve for x_1 and x_2 as a function of τ and x. The minimum value for x_1 occurs when $x = 0$, $x_1 = \sqrt{\tau}$.

$$
\begin{aligned}
x_1 x_2 &= \hat{s}/s = \tau \\
x_1 - x_2 &= x \\
x_{1,2} &= \frac{1}{2}\left[\sqrt{x^2 + 4\tau} \pm x\right] \\
x_{1,2}\big|_{x \gg \tau} &\rightarrow x + \tau/x \\
&\quad\, 0 + \tau/x
\end{aligned}
\tag{C.21}
$$

It is easy to see that for x much greater than τ, x_1 approaches x and x_2 approaches zero. In the CERN Collider data we are dominated by valance-valance production. We know the differential cross-section is basically the product of the parton distribution in the proton as a function of x_1 times the parton distribution in the anti-proton as a function of x_2. In the limit where x is much greater than τ we find that the x distribution of the W is in fact, just the x distribution of the partons. Assuming valance-valance production, the form of $d\sigma/dy$ is simple.

$$
\begin{aligned}
\frac{d\sigma}{dy} &\sim f(x_1)\bar{f}(\tau/x_1) \\
&\sim (1 - x_1)^\alpha (1 - \tau/x_1)^\beta \\
&\rightarrow (1 - x)^3 (1)
\end{aligned}
\tag{C.22}
$$

Data on the x distribution of the produced W bosons from the CERN Collider are shown in Fig. C.8. On top of that data and exact calculations we have plotted a hand calculation which is the product of the valance distributions. The agreement is impressive in both cases. Obviously this is a cross check of our understanding of the way the W bosons are produced at UA1. We expect that they are dominated by $\bar{u}d$ for the W^- and $u\bar{d}$ for the W^+ and that the sources are valance quarks in the proton and anti-proton.
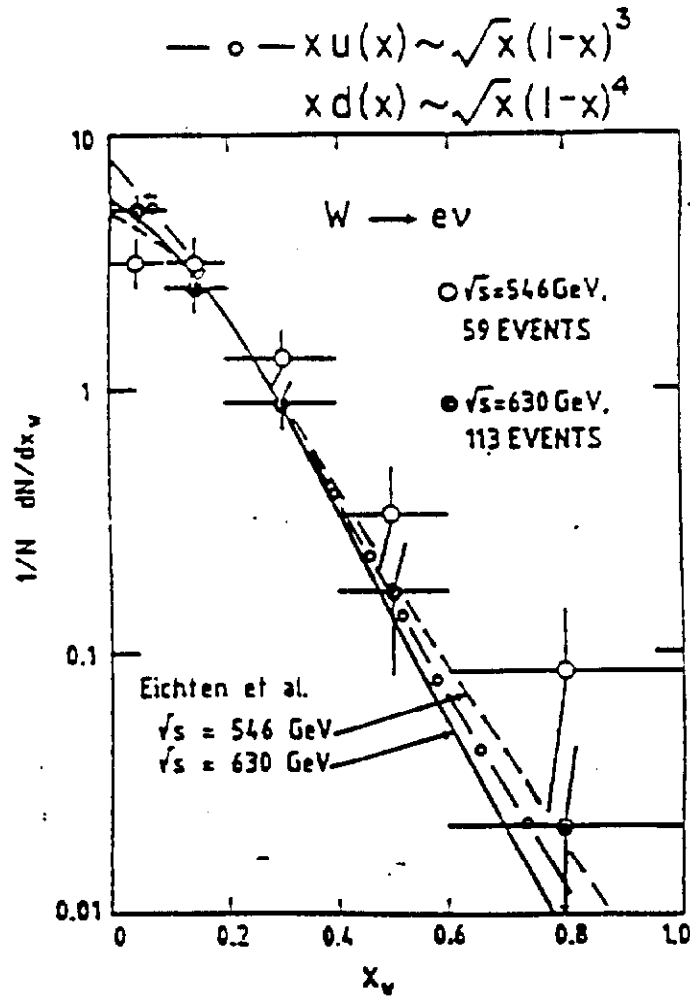
Figure C.8: UA1 data on the x distribution of W production.

Another kinematic variable that is accessible is the transverse momentum of the W boson. We have already said that since the partons have no or limited transverse momentum, the W will come out with small transverse momentum. This is indeed the case. However, there are higher order processes where quarks radiate gluons or scatter off gluon distributions in either the proton or anti-proton. The amplitudes in this case are reduced by a factor α_s with respect to that for W production with no jets.

Data for the distribution of transverse momentum in W production at the CERN Collider is shown in Fig. C.9. The data is plotted so that only the tail (in W transverse momentum) is shown. Indeed the transverse momentum is reasonably

limited. almost all of the data is contained below the characteristic mass for partonic scattering which would be the W mass. This data tells us why we can see a Jacobean peak in the lepton spectrum. The line corresponds to a calculation of higher order radiative processes.
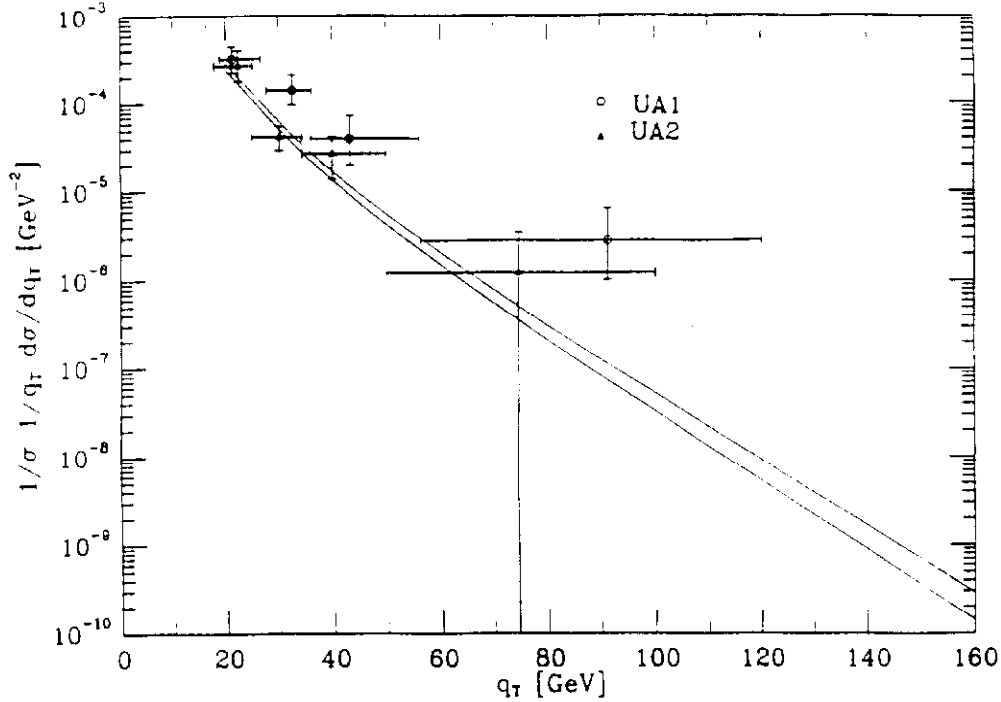
Figure C.9: UA1 and UA2 data on the $p_\perp$ distribution of W production.

It appears that the ratio of the cross-section for W plus jets to the cross-section for W without jet activity is a very clean way to extract the strong coupling constant. That ratio should be something like α_s and it is measured at the CERN Collider to be 0.13 (presumably at a scale q^2 equal to M_W^2). This value agrees with other measurements of α_s, and is our first indication that more complicated $2 \to 3$ partonic processes exist.

If we look back at Fig. A.3 it should be reasonably clear that a direct measurement of the Z width would tell us the number of light neutrinos. We could compare that number to the cosmological estimates based on the primordial deuterium abundance. Obviously, the number of replicated generations is a funda-

mental quantity in physics. However, since the Z mass resolution is not adequate at present, we must rely on a more indirect method. Take the experimental ratio of the cross-section times branching ratio for Ws into lepton plus neutrino and Zs into lepton pairs and compare them with theoretical expectations. One assumes that one can make a plausible calculation of the relative cross-sections because one needs only the relative up and down valance quark distributions. The couplings are defined by neutral current measurements $(\sin\theta_W)$ so there is some minor theoretical uncertainty in the ratio of the cross-section times branching ratio but it is not particularly large. Whether the top is kinematically accessible for W and Z decays is unknown and that sets the basic uncertainty. The cosmological limit on the number of generations i.e., the number of light neutrino types is roughly three. At the 90% confidence level, if the top quark mass is heavy, the data from the CERN Collider imply that the total number of generations is also three. However, we should note that top quark masses above about 40 GeV are not yet excluded by direct measurement. Data from the Tevatron Collider will push the top mass limit up and reduce the statistical error on $\frac{(\sigma B)_z}{(\sigma B)_W}$ in the very near future. This new data will greatly improve the determination of the number of generations.

We should also note that there is no compelling reason why the neutrino need be massless. In fact, the closure density from cosmology only requires that a light stable neutrino have a mass roughly 50 electron volts or less. If succeeding generations have heavy neutrinos which are unstable, these bounds are not relevant.

Having discussed the production of W and Z gauge bosons let's turn our attention now to Higgs scalars. If you recall from Section A, the interaction LaGrangian of Higgs scalars with fermions was a fairly standard Yukawa type interaction with a coupling constant, modified by the ratio of the fermion to the W mass. This, of course, means that the Higgs couples to the heaviest available fermion. Relative to say, the W boson, the width of the Higgs is proportional to the Higgs mass itself (as it has to be on dimensional grounds) times the ratio of the mass of the fermion divided by the mass of the W squared. This means that direct proton anti-proton production of the Higgs via $q\bar{q}$ is intolerably weak.

$$\Gamma(H \to q\bar{q}) = \left[\frac{\alpha_W}{8} \left(\frac{m_q}{M_W} \right)^2 \right] M_H$$

$$\Gamma(H \to gg) = \left[\frac{\alpha_W}{9} \left(\frac{M_H}{M_W} \right)^2 \right] \left[\left(\frac{\alpha_s}{\pi} \right)^2 \frac{|I|^2}{8} \right] M_H \qquad (C.23)$$

$$\Gamma(H \to WW) = \left[\frac{\alpha_W}{16} \left(\frac{M_H}{M_W} \right)^2 \right] M_H$$

What about gluonic formation? There is no direct coupling of the gluons to the Higgs because flavor is the weak charge, not color. However, the gluons can virtually decay into quark anti-quark pairs via the color coupling followed by quark anti-quark fusion into the Higgs. Since quarks have both color and flavor they can bridge strong to weak interactions. The Feynman diagram is shown in Fig. C.10.
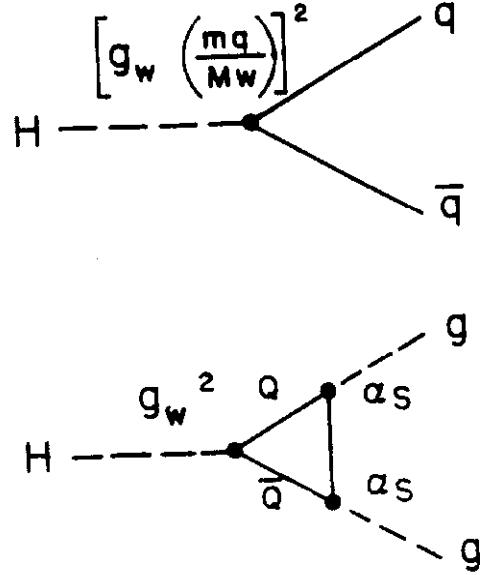
Figure C.10 Diagrams and coupling factors for Higgs boson couplings to quarks and gluons.

The relative width for the gluon decays is given in Eq. C.23. It's similar to the functional form of the width of Higgs to quark anti-quark. However, there is an additional vertex factor of α_s^2, and there is a loop integral over the internal momenta which is represented by the symbol I^2. Obviously, for a heavy Higgs the reduction factor due to the internal loop $(\alpha_s I/\pi)^2$ can still be comparable to Higgs

coupling to fermion-antifermion. A plot of the loop factor can be found in Ref. 1; it is a quantity of order unity.

We use the couplings of Higgs to W and Z pairs to estimate in Eq. C.23 the width of Higgs to W boson pairs. Since there is no loop integral or coupling constant suppression, decays into W pairs are the dominant decay mode for heavy Higgs. These considerations lead us to believe that the dominant production mechanism for Higgs will be gluon-gluon fusion via a triangle graph. We can use Eq. C.11 to estimate the rate for that process using Eq. C.23 for the evaluation of the partial width of Higgs into two gluons.

$$\sigma(H) \sim \left[\frac{\Gamma(H \to gg)}{M^3} \right] \left[2\pi^2 \ln\left(\frac{1}{\sqrt{\tau}} \right) \right] L_{gg} \qquad (C.24)$$

An exact calculation of the cross-section for various center-of-mass energy values as a function of Higgs mass is shown in Fig. C.11. The point at 2 TeV and 200 GeV Higgs mass is a hand estimate. We have taken the loop integral I to be 1. The Higgs width to W pairs is about 2 GeV for 200 GeV Higgs and the partial width into gluon pairs is only about 1 MeV. The typical scale for Higgs is picobarns.

$$\begin{aligned}
\sqrt{s} &= 2 \text{ TeV}, \ M_H = 200 \text{ GeV} \\
\sqrt{\tau} &= 0.1, \ \Gamma_H \sim 2 \text{ GeV}, \ \Gamma(H \to gg) \sim 1 \text{ MeV} \\
\Gamma(H &\to gg)/M^3 \sim 0.5 \ pb
\end{aligned} \qquad (C.25)$$

The hand estimate appears to be quite close to the calculation. Note that even with a Tevatron Upgrade, which would have a luminosity of $5 \times 10^{31} cm^2/\text{sec}$, or an integrated luminosity of $5 \times 10^{38} cm^2/\text{run}$ one would only create 100 Higgs of 200 GeV mass in a year. Given branching ratios and detection efficiencies, this is obviously rather an elusive particle due to its weak coupling to ordinary matter. It is equally clear what the SSC advantage is; at 200 GeV for M_H, the cross-section is ~ 1000 times larger at the SSC than at the Tevatron.
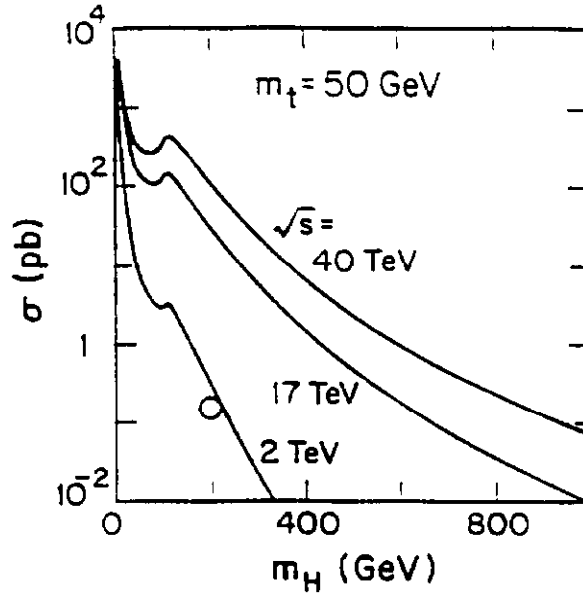
Figure C.11: Cross-section for Higgs boson production for various $\sqrt{s}$ values as a function of Higgs mass. The point $\odot$ is a hand estimate for $\sqrt{s} = 2$ TeV.

Another possible source for Higgs are the Ws radiated by the quarks in the proton. The estimate we make is very much in the spirit of two photon physics, using the $W - W$ approximation i.e., $e^+e^- \rightarrow e^+e^-\gamma\gamma$ is like $u\bar{u} \rightarrow d\bar{d}W^+W^-$. The kinematics is illustrated in Fig. C.12.
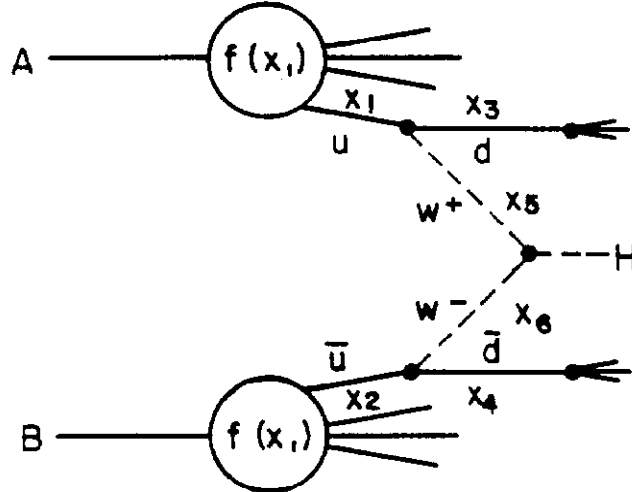

Figure C.12: WW radiation by $u\bar{u}$ with subsequent fusion into a Higgs scalar.

A crude estimate of the cross-section follows from our discussion of bremsstrahlung in Section B. We assume collinear W's since the process is analagous to the

bremsstrahlung of collinear photons. The distribution function is now perturbatively calculable, i.e., $f(x)dx \sim (\alpha/\pi)dx/x$ as in Eq. B.9.

The joint probability of finding x_1, x_2, x_5, and x_6 is:

$$
\begin{aligned}
d\sigma &\sim C[dx_1 f(x_1)dx_2 f(x_2)]\left[dx_5 \frac{(\alpha_W/4\pi)}{x_5} dx_6 \frac{(\alpha_W/4\pi)}{x_6} \tilde{\sigma}(M^2)\right] \\
\tau' &= x_1 x_2 = \hat{s}/s \\
z &\equiv x_5 x_6 = M^2/\hat{s} \\
\tau &= M_o^2/s \\
d\sigma &\sim C[d\tau' dy f(x_1)f(x_2)]\left(\frac{\alpha_W}{4\pi}\right)^2 \left[\frac{dz}{z}\text{``}dy\text{''}\tilde{\sigma}(M^2)\right]
\end{aligned}
\tag{C.26}
$$

After integrating over "dy" (rather like $dy \to \Delta y$), and assuming small z we have:

$$
\int \frac{dz\,\text{``}dy\text{''}}{z} \quad \sim \quad [\ln(1/z)]/z
\tag{C.27}
$$

Then using Eq. C.6 in the narrow width approximation one can perform the integration over z.

$$
\left(\frac{d\sigma}{dy}\right)_{y=0} \sim C \int \left[d\tau' f(\sqrt{\tau'})\bar{f}(\sqrt{\tau'})\right]\left(\frac{\alpha_W}{4\pi}\right)^2 \left[\ln(\tau'/\tau)\frac{\pi^2\Gamma_0}{M_0^3}\right]
\tag{C.28}
$$

We still have to integrate over τ', $\tau < \tau' < 1$. If we take the valance distribution, $u_v(x)$ for $f(x)$, then an extremely approximate result is,

$$
M^2\left(\frac{d\sigma}{dy}\right)_{y=0} \sim L_{u\bar{u}}[\pi^2\Gamma/M]\left[\frac{2(\alpha_W/4\pi)^2 \ln\left(\frac{1}{\tau}\right)}{\sqrt{\tau}}\right]
\tag{C.29}
$$

Comparing to the previous result for gluon fusion we find a ratio:

53

$$\frac{\sigma^{WW}(H)}{\sigma^{gg}(H)} \quad \sim \quad \left[\frac{Lu\bar{u}}{Lgg}\right] \left[\frac{2\frac{\ln(1/\tau)}{\sqrt{\tau}}\left(\frac{\alpha_W}{4\pi}\right)^2}{\frac{|I|^2}{8}\left(\frac{\alpha_s}{\pi}\right)^2}\right] \tag{C.30}$$

Clearly, this latter mechanism will become important at higher τ, since $L_{u\bar{u}}/L_{gg}$ increases with τ so as to overcome the coupling constant ratio. Numerically Eq. C.30 is $O(1)/(1 - \sqrt{\tau})^6$, so the WW fusion mechanism dominates at large τ. This mechanism is then the most important one near threshold.

A very heavy Higgs becomes difficult to detect since the width given in Eq. C.23 is increasing as the cube of the mass of the Higgs. The width is comparable to the mass for Higgs masses of about 1 TeV, which means that the weak interactions are becoming strong. This fact is the basis for the statement that some new physics will appear at the 1 TeV mass range. It also means that the Higgs will be undetectable if it is that heavy. We will have further comment on this subject in Section D after we have evaluated one of the backgrounds to a Higgs search.

$$\begin{aligned}\Gamma \quad &\sim \quad \left(\alpha_W/M_W^2\right) M^3, \ \Gamma/M \sim 1 \text{ for} \\ M \quad &\sim \quad M_W/\sqrt{\alpha} \sim 1 \text{ TeV}\end{aligned} \tag{C.31}$$

Recently there has been a lot of discussion about possible modes of Upgrade for the Fermilab Collider. Three options that have been discussed are; pp at high luminosity at 2 TeV, $\bar{p}p$ at 2 TeV which is what we have now, and upgrading to $\bar{p}p$ at 3 TeV center-of-mass energy. For pp obviously we would use Eq. C.15 to estimate production cross-sections of sequential neutral weak bosons (Z's) via valance-sea whereas for $\bar{p}p$ at the two possible energies we would use a valance-valance estimate (at very high masses the valance quarks are dominant). A plot of the Z' production cross-section as a function of Z' mass for the three different Upgrade options is shown in Fig. C.13. The smooth lines are exact calculations while the discrete points are the various hand estimates based on Eq. C.15 and the valance and sea distributions. It is clear that at very high masses the valance anti-quarks available in the anti-proton are crucial. For this particular kind of physics, the possible luminosity increase of proton-proton over the proton anti-proton option would

54

probably not overcome the cross-section advantage of the $\bar{p}p$ option. Another point is that if the energy is increased rather than the luminosity, then one need not upgrade the detectors. A detector upgrade would be an expensive proposition.
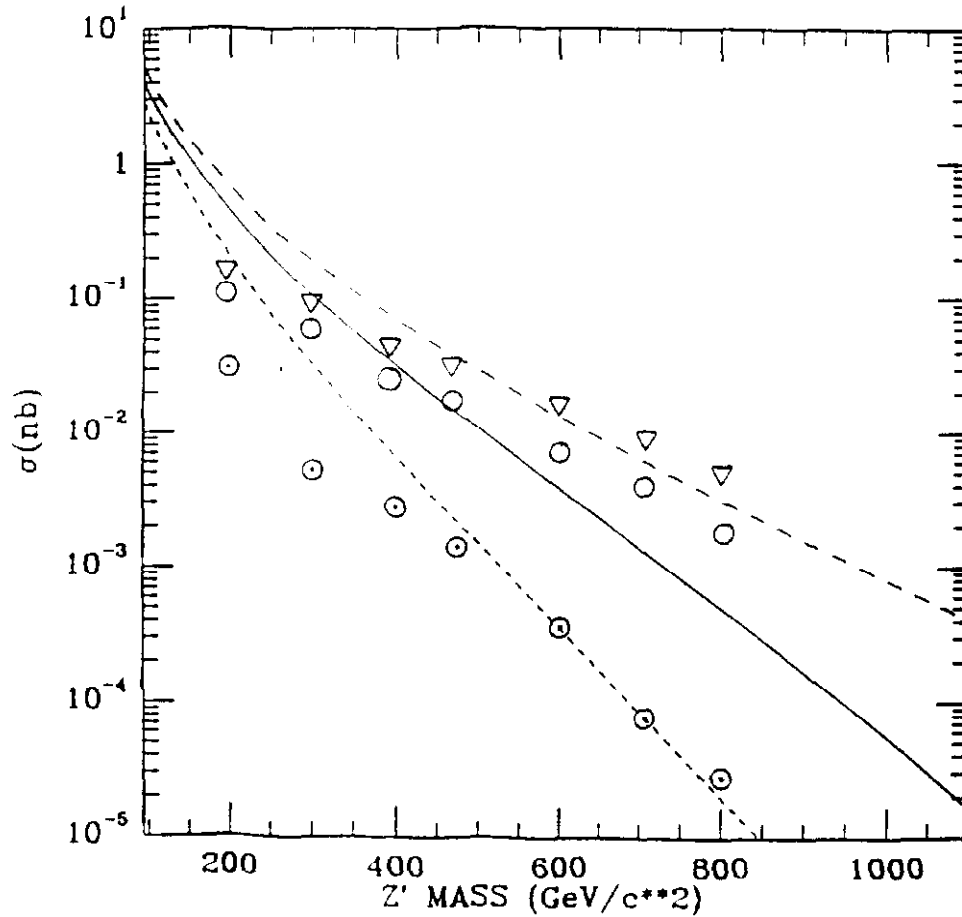

Figure 13: Z' production cross-section as a function of Z' mass for pp at 2 TeV $\sqrt{s}$ (- -) $\bar{p}p$ at 2 TeV (—) and $\bar{p}p$ at 3 TeV (- -). Hand estimates are also shown as points $\odot$, O, and $\triangledown$, respectively.

This hand estimate for sequential Z' production completes our discussion of proton anti-proton formation of well defined resonance states. We have looked at gluonic formation of vector mesons, quark anti-quark production of W and Z bosons, and estimates of gluon-gluon and $W - W$ formation of Higgs scalars. In all

cases, we have been able to make a reasonable hand estimate of the cross-section level and the cross-section shape as a function of center-of-mass energy. In the case of the W and Z bosons we have been able to look in detail at the x and $p_\perp$ distribution of the initial state Ws and the decay distributions. We can thus have some confidence that when we extrapolate to higher mass states like the Z', our hand estimates will give us a reasonable expectation of what the discovery limits are.

Finally, we finish this Section with estimates of typical cross-sections for the production of objects whose mass is near the discovery limit of the Tevatron. Using the formulae derived in this Section, the reader can make his own hand estimate for the relevant process. In this case, we pick a mass of 300 GeV. We use our generic formula for $(d\sigma/dy)$ at $y = 0$ which we derived in Eq. C.9. This leads us to the generic estimate for the differential cross-section shown in Eq. C.32.

$$
\begin{aligned}
\left(\frac{d\sigma}{dy}\right)_{y=0} &\sim L_{f\bar{f}}\left(\frac{\pi^2\Gamma}{M^3}\right)(2J+1) \\
\Gamma &\sim \text{``}\alpha\text{''}M, \quad xf(x) \equiv a(1-x)^\alpha x^\beta \\
\left(\frac{d\sigma}{dy}\right)_{y=0} &\sim C\left[a(1-\sqrt{\tau})^\alpha\sqrt{\tau}^\beta\right]^2\left[\frac{\pi^2\text{``}\alpha\text{''}}{M^2}\right](2J+1)
\end{aligned}
\tag{C.32}
$$

For gluon fusion production of a state of mass M, the cross-section just based on a mass scale of 300 GeV is about 4.4 nanobarns. The coupling constant to that mass is of order the strong coupling constant, and if it were a vector particle then the differential cross-section at $y = 0$ would be about 3 nb for $\sqrt{s} = 2$ TeV.

$$
\begin{aligned}
gg \to M, \quad & \frac{1}{M^2} = 4.4 \; nb \\
\alpha_s &\sim 0.1, \; J = 1, \; \sqrt{\tau} = 0.15 \\
\left(\frac{d\sigma}{dy}\right)_{y=0} &\sim 2.8 \; nb
\end{aligned}
\tag{C.33}
$$

That cross-section would be a plausible estimate for say a strongly interacting η_t resonance if it were to exist at 300 GeV (with a top quark mass of $\sim$150 GeV). In the case of electroweak production of a 300 GeV mass, say by $u\bar{u}$ annihilation, the differential cross-section at $y = 0$ is of order 1 nanobarn. Formulae to estimate

the total cross-section are shown in Eq. C.34 below:

$$u\bar{u} \quad \to \quad M, \quad \left(\frac{d\sigma}{dy}\right)_{y=0} \sim 1 \; nb$$

(C.34)

$$\sigma \quad \sim \quad \frac{\pi^2 \alpha}{M^2} \; [xu(x)x\bar{u}(x)]_{x=\sqrt{\tau}}$$

Such formulae can be used to estimate production rates of new particles which have strong or electroweak couplings.

D. HADRON-HADRON SCATTERING IN THE POINTLIKE DOMAIN

We now begin to examine the pointlike scattering observed in hadron-hadron colliders. The cross-section which we derived in Section C was the joint probability of getting a parton with momentum fraction x_1 from hadron A and a parton with momentum fraction x_2 from hadron B. Initially, we are going to consider quark anti-quark annihilation into virtual photons of variable mass, which is called the Drell-Yan process. We get the equations seen below:

$$\left(\frac{d\sigma}{dy\,d\tau}\right)_{y=0} = C f(\sqrt{\tau})\bar{f}(\sqrt{\tau})d\hat{\sigma}$$

(D.1)

$$= \frac{1}{3} [u(x)u(x)]_{x=\sqrt{\tau}} \left(\frac{4\pi\alpha^2}{3\hat{s}}\right) Q_u^2$$

These equations are formally the same as Eq. C.5.b with a color factor of 1/3 for quarks instead of a color factor of 1/8 for gluons. The source functions are the distribution function of up quarks in the proton and anti-up quarks in the anti-proton. This assumes that the process proceeds through EM coupling, so that Qu = 2/3 dominates.

$$M^3 \left(\frac{d\sigma}{dy\,dM}\right)_{y=0} = F(\tau)$$

(D.2)

$$= 2L_{u\bar{u}}\,(d\hat{\sigma}\hat{s})$$

57

Clearly the simplest prediction is that of scaling; that M^3 times the differential cross-section $(d\sigma/dM)$ is a function only of the scaling variable τ. In addition, if we put in the pointlike cross-section (which we have already quoted in Eq. B.1) we get the numerical prediction shown below which goes beyond the scaling prediction:

$$M^3 \left(\frac{d\sigma}{dy\,dM} \right)_{y=0} = 2L_{u\bar{u}} \left[\frac{4\pi\alpha^2}{3} Q_u^2 \right]$$

(D.3)

$$(\hbar c)^2 \alpha^2 = 2.1 \times 10^{-32} cm^2 \text{ GeV}^2 = 21 \ nb \text{ GeV}^2$$

Since the proton is a broadband beam of partons containing all momenta, and since x_1 and x_2 specify the mass of the initial state, all possible masses of the virtual photon are excited simultaneously. Since the weight given to the partonic cross-section is α^2 times the square of the quark charge, effectively we are measuring only $u\bar{u}$ annihilation. Other quarks of one third charge contribute a correction factor of only about 1/4. Data for dilepton production in pp and $\bar{p}p$ collisions is shown in Fig. D.1. This data was taken at a variety of center-of-mass energies and is shown as a function of the scaling variable $\sqrt{\tau}$.
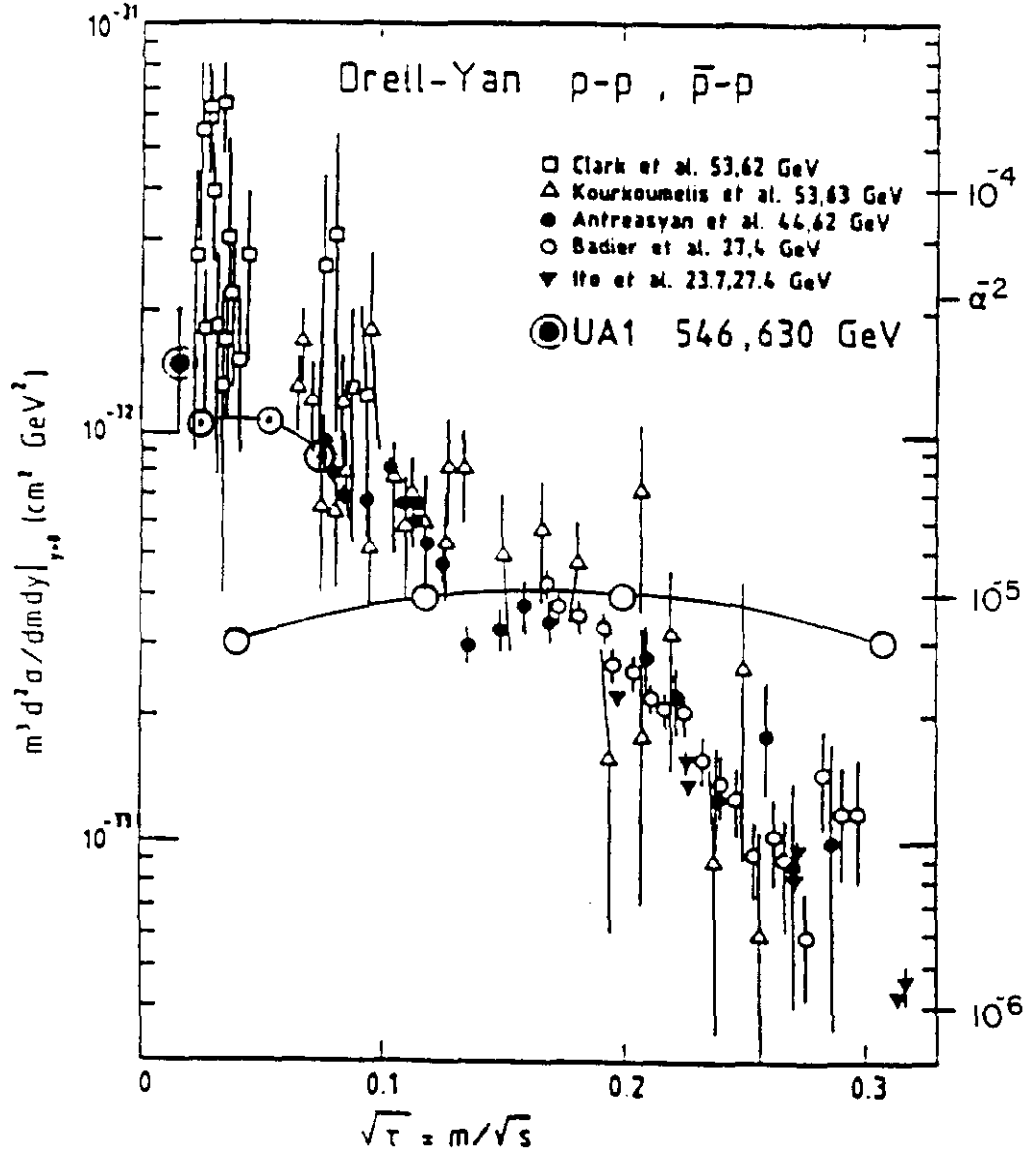
Figure D.1: Dilepton data in pp and $\bar{p}p$ collisions. Hand estimates for sv and vv are plotted as ⊙ and o, respectively.

Note that the vertical scale is dimensionless. Since it is effectively the partonic cross-section its scale is α^2. In fact, $(\hbar c)^2 \alpha^2$ is 21 nanobarn GeV^2 which is a dimensionless number. It is gratifying to find that scaling works and that the vertical scale in the Drell-Yan data, at small $\sqrt{\tau}$ where $L_{u\bar{u}}$ is a number O(1), is of that order of magnitude. In more detail, one can use Eq. D.3 to make hand estimates of the Drell-Yan data. The two curves shown in Fig. D.1 are valance-valance and valance-sea cross-sections. It is good to see that not only is the scaling behavior

59

predicted but that the size and shape of the scaling cross-section is consistent with the electromagnetic cross-section. Moreover, the detailed hand estimates come within factors of two of the actual data. At moderate τ values the sea-valance and valance-valance cross-sections are sufficient. Obviously the peaking at very low values of τ is the sea-sea contribution.

The transverse momentum of the virtual photon γ^* can be found from that of the $\mu^+\mu^-$ pair. We take it as a posteriori evidence for small intrinsic transverse momentum that $p_\perp(\mu^+\mu^-) \sim \Lambda$. At higher values of $M(\mu^+\mu^-)$, initial state bremsstrahlung will also contribute to $p_\perp(\mu^+\mu^-)$. The measurements of Drell-Yan dimuons serve to confirm the assumptions we have already made.

Emboldened by success one can try to use the Drell-Yan process to estimate pair production of gauge bosons. You recall from Section A that the non-Abelian nature of the gauge bosons resulted in triple gauge boson couplings. Electroweak unification meant that those couplings were of order α. Hence one can use the Drell-Yan mechanism at a threshold mass of twice the boson mass to look at pair production of Ws by virtual photons. Looked at another way the Drell-Yan virtual photon can decay into a W pair. This means that instead of $u\bar{u}$ annhilating into a virtual photon and then decaying into lepton pairs (which has a cross-section $\sim \alpha^2 Q_u^2/\hat{s}$) the virtual photon in this case couples with strength α in decaying into W pairs. We take the Drell-Yan cross-section at 2 TeV at a mass of twice the W mass, in which case $\sqrt{\tau}$ is 0.08. The total cross-section is the differential cross-section integrated over all masses with a rapidity range Δy as we have already estimated for other processes.

$$
\sigma_{WW} \sim \int_{2M_W}^{\infty} \left(\frac{d\sigma}{dM\,dy} \right)_{y=0}^{DY} dM(\Delta y)
$$

$$
\sigma_{WW} \sim \left(\frac{d\sigma}{dM\,dy} \right)_{\substack{M=2M_W \\ y=0}}^{DY} \Delta y \left(\frac{2M_W}{2} \right)
$$

(D.4)

The Drell-Yan cross-section (Fig. D.1) is about 10 nanobarn GeV^2 at twice the W mass. The rapidity interval is about 6. This leads us to a cross-section estimate for W pairs in the one picobarn range.

60

$$\sqrt{s} \;=\; 2 \text{ TeV, } \sqrt{\tau} = 0.08$$

$$M^3 \left(\frac{d\sigma}{dM\,dy} \right)^{DY}_{\substack{M=2M_W \\ y=0}} \;\sim\; 10\; nb\; \text{GeV}^2 \tag{D.5}$$

$$\Delta y \;\sim\; 6$$

$$\sigma_{WW} \;\sim\; 1.2\; pb$$

For a luminosity of 10^{31} cm^2 per second, assuming that there are $\pi \times 10^7$ seconds per year with an efficiency of one over π, in a one year run one would get 120 produced W pairs. That means one and a half W pairs where both Ws decay into μ plus neutrino. Obviously the study of boson pairs will be a feature of improved luminosity running in the Tevatron Collider in the future. Clearly, establishing the triple boson couplings shown in Fig. A.7 will be of crucial importance in validating the Standard Model. Note that the $WW\gamma$ coupling (Fig. A.7) means that virtual $W^\star$ production (Fig. C.4) followed by the decay $W^\star \rightarrow W\gamma$ has a cross-section larger than that for WW. Because the mass of the $W\gamma$ is less than a WW, one need not pay as large a $1/M^2$ price, and the cross-section is larger. The biggest triple boson process then leads to $W\gamma$ in the final state.

We show in Fig. D.2 exact predictions for the cross-sections for W and Z pairs as a function of center-of-mass energy.
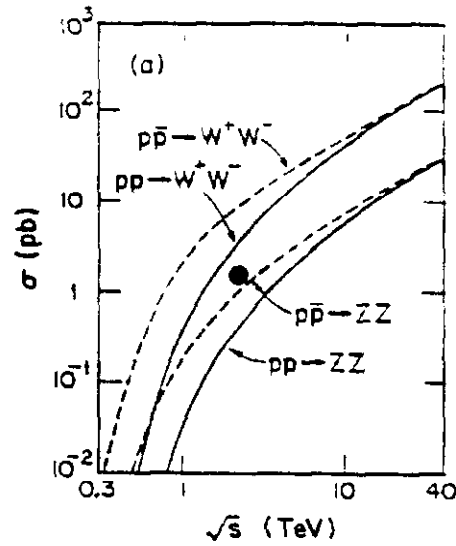
Figure D.2: Predicted cross-section for WW and ZZ pair production as a function of $\sqrt{s}$. The point o is a hand estimate for $\sqrt{s} = 2$ TeV.

It is clear that the hand estimate we have made is sufficient to give us a plausible order-of-magnitude for the cross-section. It is also clear that near threshold (which means at large τ), $\bar{p}p$ production has a much larger cross-section than pp because at large τ the valance quark contributions are important. This is perhaps another argument for using enhanced energy in $\bar{p}p$ collisions as opposed to enhanced luminosity in pp collisions in order to push the discovery threshold.

Of course, as we discussed in Section C, another possible source of electroweak boson pairs comes from the decays of Higgs particles. Feynman diagrams for Drell-Yan dilepton production, Drell-Yan W pair production, and gluon-gluon fusion production of Higgs with subsequent decay into W pairs are shown in Fig. D.3. The arguments for Z pairs are somewhat different as we will mention later. Basically the processes are shown in Fig. B.4 for $gg \to Q\bar{Q}$ if the initial and final states are reversed. The fermion exchange diagram leads to say, $u\bar{u} \to ZZ$, while the boson annihilation diagram leads to say $u\bar{u} \to \gamma^* \to W^+W^-$, or $u\bar{u} \to Z^* \to W^+W^-$ (see Fig. A.7). Since the latter graph does not allow Z pairs in the final state, it is not surprising that the cross-section for W pairs exceeds that for Z pairs.
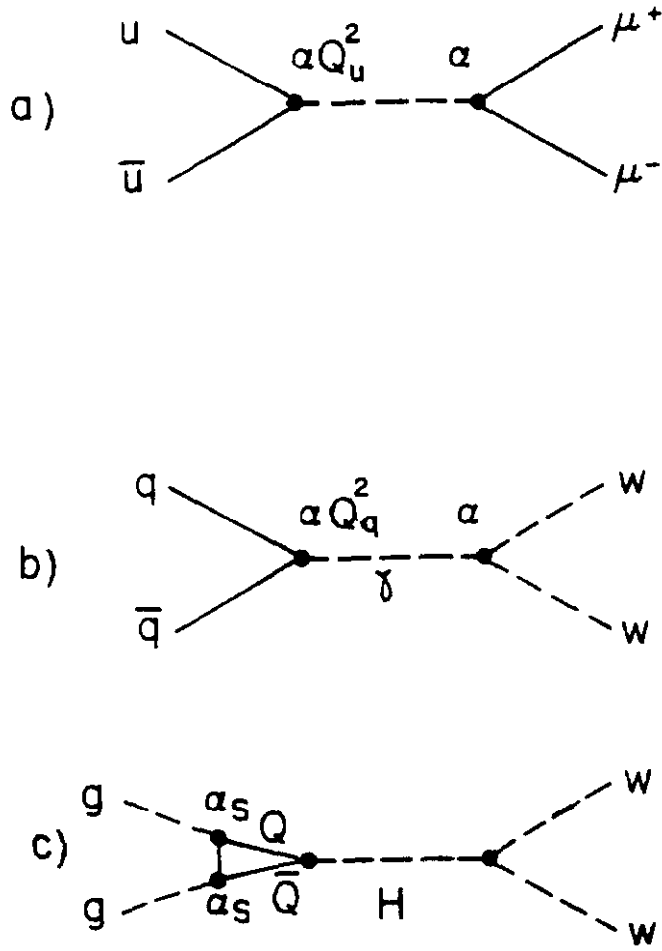
Figure D.3: a) Drell-Yan dilepton diagram. b) Drell-Yan W pair diagram. c) Gluon-gluon fusion diagram for W pair production.

For comparison the Drell-Yan production cross-section has already been evaluated at a $\sqrt{\tau}$ of 0.1. At that value we saw that we are dominated by valance-valance. We get a differential cross-section as a function of mass of 0.6 femtobarns per GeV. In the case of the gluonic production of Higgs we've already evaluated (for 200 GeV Higgs) the total width into W pairs to be 2 GeV. The width into gluon pairs is 1 MeV. Thus, the production cross-section is roughly 0.1 picobarn per GeV.

63

$$\left(d\sigma/dM\,dy\right)^{DY}_{\substack{M=200 \\ y=0}} \quad \sim \quad 0.6 \ fb/\text{GeV}$$

$$M \quad = \quad 200 \ \text{GeV}$$

$$\Gamma_H \quad \sim \quad \Gamma(H \to WW) \sim 2 \ \text{GeV} \ \sim dM \qquad (\text{D.6})$$

$$\Gamma(H \to gg) \quad \sim \quad 1 \ \text{MeV} \sim B_{gg}\,dM$$

$$\left(d\sigma/dM\,dy\right)^{H}_{y=0} \quad \sim \quad 0.1 \ pb/\text{GeV}$$

As we will see later, WW production is probably dominated by heavy $t\bar{t}$ pairs. Still, let us compare WW events from Drell-Yan to those from Higgs, assuming $B(H \to WW) \sim 1/2$. Using our previous results, with $dM \sim \Gamma$:

$$\frac{\left(d\sigma/dM\,dy\right)^{H}}{\left(d\sigma/dM\,dy\right)^{DY}} \quad \sim \quad \left(\frac{\alpha_s|I|}{\alpha Q_u}\right)^2 \left[\frac{3}{64\pi}\right]\left[\frac{L_{gg}}{L_{u\bar{u}}}\right] \qquad (\text{D.7})$$
$$\gg 1$$

Comparing the two Feynman diagrams in Fig. D.3, the ratio has a term of α^2 for Drell-Yan due to the coupling vs. the branching fraction into gluons due to the internal heavy quark anti-quark loop integral, $(\alpha_s|I|)^2$. There is also a term involving the ratio of the source terms of gluons to up quarks. Taking $|I|^2 \sim 1$, we get the ratio shown in Fig. D.4.a. Clearly $H \to WW$ exceeds Drell-Yan backgrounds for $M_H \stackrel{<}{\sim} 1$ TeV, with $\sqrt{s} = 2$ TeV. However, as shown in Fig. D.4.b, the Higgs width, $\Gamma_H \sim 2\Gamma(H \to WW) \sim \left(\frac{\alpha}{\sin^2\theta_W}\right)\left[\frac{1}{8}\left(\frac{M_H}{M_W}\right)^2\right]M_H$, is $\sim M_H$ at a mass of ~ 1.0 TeV. Thus the narrow width approximation is clearly not justified and in any case, with a width of 1 TeV, the concept of "resonance" is no longer valid.
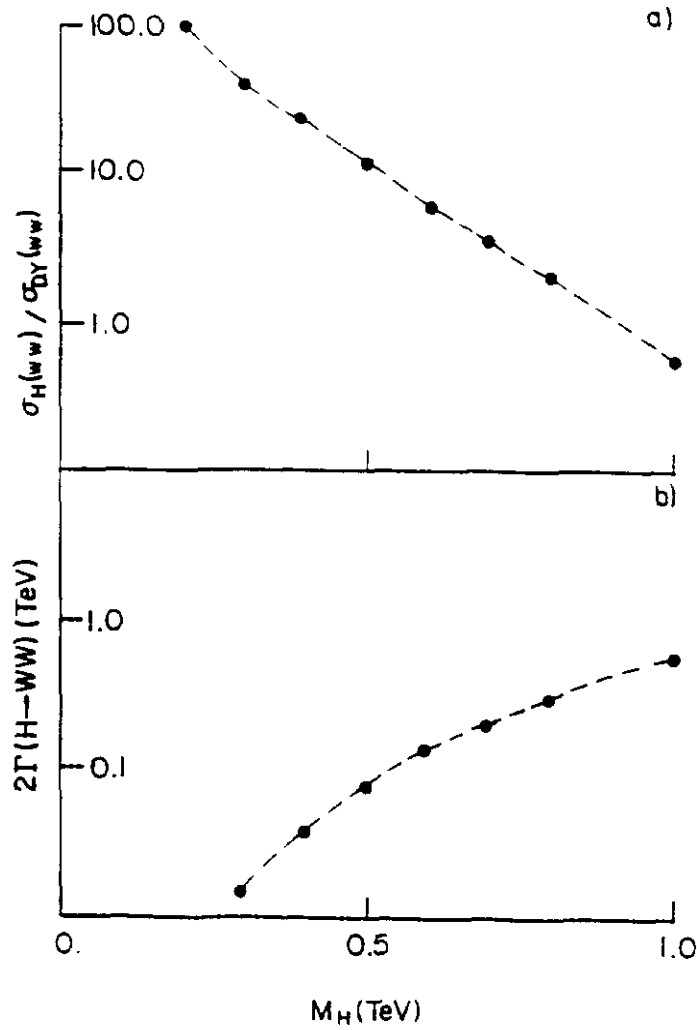
Figure D.4: a) Ratio of Drell-Yan to Higgs cross-sections. b) Higgs width as a function of Higgs mass.

Another point to make is that there is another D-Y like contribution, rather like the Higgs graph (Fig. D.3.c) where gluon-gluon fusion into quarks forms a virtual γ which decays into W pairs. This graph, with respect to the classical D-Y graph is in the ratio

$$\frac{\sigma_{gg}^{DY}}{\sigma_{u\bar{u}}^{DY}} \sim \left(\frac{\alpha_s}{\pi}\right)^2 |I'|^2 [L_{gg}/L_{u\bar{u}}] \tag{D.8}$$

Obviously, looking at Eq. D.7, this higher order contribution to D-Y yields WW pairs which are of O(1) with respect to the Higgs. It is a good search strategy to look for a heavy Higgs decaying into gauge pairs if one has the luminosity available to actually observe those decays. Remember that the observable branching ratio of Ws and Zs into leptons is small, which makes the overall detection rate for Higgs rather small. This implies that one needs a substantial luminosity increase in order to have a chance to observe these kinds of decays.

We note that in W pairs D-Y is comparable to Higgs (especially in light of Eq. D.8) and we will soon see that top decay (if top is heavy) will dominate all sources of W pairs. In Z pairs, photons and top do not contribute (see Fig. A.7). However, there is a contribution from $q\bar{q} \to ZZ$ (see Fig. B.4) which we will evaluate in the discussion of heavy flavors ($gg \to Q\bar{Q}$). The graph is responsible for the ZZ cross-section shown in Fig. D.2. Obviously if W pair backgrounds to Higgs from D-Y are substantial, Z pair backgrounds from $q\bar{q}$ are also. Finding the Higgs will be a formidable task.

We now consider gluon-gluon scattering. The topic is then strong interactions and jets. You recall in Section B we wrote down the pointlike cross-section for gluon elastic scattering. It is slightly complicated because there are exchange peaks which are familiar from Rutherford scattering. That makes it a more complicated topic than the Drell-Yan formation process. We need to come to terms with the exchange peaks which give a diverging total cross-section. At 90^0 the coupling constants and Feynman diagrams are such that gluon-gluon elastic scattering dominates other processes. The gluon source at most accessible values of Feynman x is also the largest source. This means that we can consider in most cases that jet phenomena come exclusively from gluon elastic scattering. The special case of the elastic differential cross-section at 90^0 is given below.

$$\hat{s} + u + \hat{t} = 0$$

$$\hat{\theta} = 90^0, \qquad \hat{t} = \hat{u} = -\hat{s}/2 \tag{D.9}$$

$$\frac{d\hat{\sigma}_{gg}}{d\hat{t}} \simeq \frac{9\pi\alpha_s^2}{2\hat{s}^2}\left(\frac{27}{4}\right)$$

On the other hand, at 0^0 the exchange piece gives a one over $\hat{t}^2$ behavior which dominates. We then have a differential cross-section which is very similar, except for numerical constants, to Eq. B.2 for Rutherford scattering.

$$\hat{\theta} \sim 0^0, \qquad \hat{t} \sim 0, \;\; \hat{u} \sim -\hat{s} \tag{D.10}$$

$$\frac{d\hat{\sigma}_{gg}}{d\hat{t}} \sim \frac{9\pi\alpha_s^2}{2\hat{t}^2}$$

What evidence do we have that we are indeed seeing Rutherford like scattering in jet production? If one measures the jet angles and momenta by calorimetry, those kinematic variables are sufficient to define the Feynman x of the dijet system and its invariant mass. The transverse momentum tells you the scattering angle as we derived in Eqs. B.16 and B.17. This is experimentally how you determine the parton-parton scattering angle. A convenient variable for two-body Rutherford like scattering is χ, which is defined below:

$$\chi \equiv \left(\frac{1 + \cos\hat{\theta}}{1 - \cos\hat{\theta}}\right) = \left(\hat{u}/\hat{t}\right) = \cot^2\left(\hat{\theta}/2\right)$$

$$\hat{t} \sim (1 - \cos\hat{\theta})$$

$$d\hat{t} \sim d(\cos\hat{\theta}) \tag{D.11}$$

$$d\chi/d\cos\hat{\theta} \sim 1/\hat{t}^2$$

$$\frac{d\hat{\sigma}}{d\chi} \sim \frac{d\hat{\sigma}}{d\hat{t}}\left(\frac{d\hat{t}}{d\chi}\right) \sim \text{const}$$

Note that we simply assert that the outgoing two gluon state is identified as a dijet state. We do not yet discuss how this is accomplished. The fragmentation of partons into jets of hadrons is discussed only later in Section E. As we show in Eq. D.11, the differential cross-section for partonic scattering as a function of χ is constant if we have Rutherford like behavior. Data from the CERN collider on the angular distribution of dijet events as a function of the variable of χ is

shown in Fig. D.5. Obviously the basic behavior is that the distribution is flat in χ, which as we have said, indicates Rutherford like partonic scattering. More detailed exact calculations give you a better fit to the data. The mostly uniform distribution in χ seems to confirm that we have two body scattering. However, the data only extends to scattering angles $\cos \hat{\theta} \lesssim 0.5$ due to the experimental problem of resolving the jets from the beam fragments.
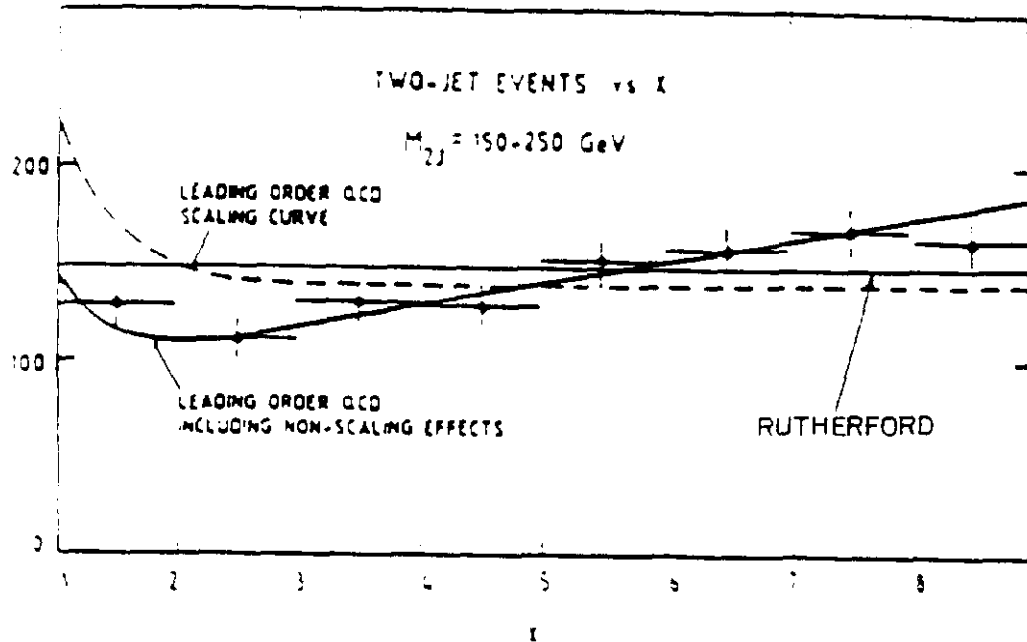

Figure D.5: Angular distribution for 2 jet events as a function of χ.

What about the full structure of a dijet event? The initial state, its mass, and longitudinal momentum are determined by the Feynman x values of the incident partons. The orientation of the jets in the final state is defined by the third variable, the parton-parton scattering angle. Modifying Eq. D.2 for the color factors and sources associated with gluons we can write down the triply differential cross-section for jet production as in Eq. D.12:

$$M^3 \left(\frac{d\sigma}{dM\,dy\,dp_\perp^2} \right)_{y=0} \sim 2L_{gg}\,(d\hat{\sigma}\hat{s})$$

$$\hat{p}_\perp = \frac{\sqrt{\hat{s}}}{2}\sin\hat{\theta} \sim p_\perp \qquad \text{(D.12)}$$

$$d\hat{\sigma}/dp_\perp^2 = d\hat{\sigma}/d\hat{t} \left(\frac{1}{\cos\hat{\theta}} \right)$$

$$M^3 \left(d\sigma/dM\,dy\,dp_\perp^2 \right)_{y=0} \sim 2L_{gg} \left[\hat{s}\frac{d\hat{\sigma}}{d\hat{t}} \left(\frac{1}{\cos\hat{\theta}} \right) \right]$$

We have assumed that there is no transverse momentum due to the partons; it is all due to the two-body scattering process. This assumption implies that jets are back to back in azimuth. If we want to specialize to doubly differential cross-sections, (specifically at $y = 0$), we need to integrate over the unobserved variable. There is a minor technical difficulty in that, in distinction to say Drell-Yan processes without exchange peaks; the integral diverges. This is not a surprise; it is the same divergence which shows up in Rutherford scattering and one merely has to cut it off. One can do that by defining a minimum scattering angle for which you can observe jets. That minimum angle happens because there is a minimum transverse momentum for which jets are operationally observable amid the debris of the proton and antiproton fragments. Doing the integral implied in Fig. B.4 and Eq. D.12 exactly:

$$M^3 \left(d\sigma/dM\,dy \right)_{y=0} = 2L_{gg} \left(\frac{9\pi\alpha_s^2}{2} \right) \cdot \left[\frac{34}{6} \right] \left[1 + \frac{6}{17} \left(\frac{2}{1 - Z_{min}} - 1 \right) \right] \text{(D.13)}$$

$$Z_{min} \equiv \cos\hat{\theta}_{min} = \sqrt{1 - (2p_\perp^{min}/M)^2}$$

If we just ignore the problem of defining the minimum transverse momentum, numerically it turns out that we can use the differential scattering cross-section at 90°. This assumption is numerically within 85% of the full integral if we set $Z_{min} = 0$ in our definition of the minimum transverse momentum.

$$M^3(d\sigma/dM\,dy)_{y=0} \sim 2L_{gg} \left[d\hat{\sigma}_{gg}\hat{s} \right] \qquad \text{(D.14)}$$

$$\sim 2L_{gg} \left[\frac{9\pi\alpha_s^2}{2} \left(\frac{27}{4} \right) \right]$$

Given the uncertainties in the gluon distributions themselves, their evolution, the value of q^2 at which the running coupling constant should be evaluated, and other uncertainties, the theoretical quantities are not well defined to within factors $\pm$ 2. That being the case, we might as well just make a rough estimate as in Eq. D.14 and see how well this hand estimate compares with the data itself. Data on the invariant mass and transverse momentum distributions of 2 jet events from the CERN Collider are shown in Fig. D.6.
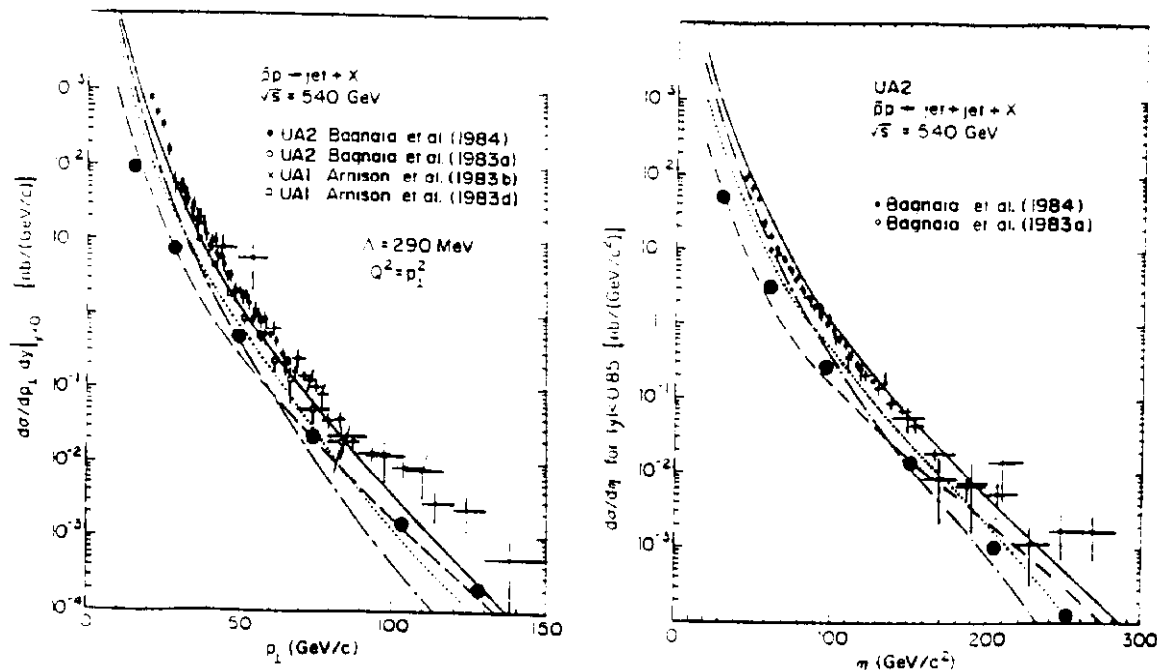
Figure D.6: Invariant mass and $p_\perp$ distributions of 2 jet events from UA2. Hand estimates are shown as $\odot$ points. Both jets have $|y| < 0.85$.

The jet distribution figure illustrates the reasons why we have adopted a simple minded approach which ignores evolution of $f(x)$ and "running" of α_s. There exists an order of magnitude uncertainty in "exact" cross-section estimates. These unknowns make hand estimates as accurate as anything, and lead us to mentally assign large errors to any "exact" calculation.

The hand estimates that are made using Eq. D.14 are also shown in the figures. At a center-of-mass energy of 540 GeV we took a strong coupling constant α_s equal

to 0.15. Looking at Fig. D.6, we see that the hand estimates are in reasonable agreement with the data. It is worth noting that without the $(1 - \sqrt{\tau})^{12}$ gluon factor we would just have $1/M^3$ for the differential cross-section as a function of jet-jet mass. A mass of 250 GeV would have a cross-section three orders of magnitude higher, so in fact the gluon distributions are very important. Note that in this data from UA2, both jets are required to come out at wide angles. This is equivalent to a cut on the minimum transverse momentum.

Turning to the doubly differential cross-section for jets as a function of rapidity and transverse momentum, we need to integrate over the invariant mass of the dijet system. The relationship between transverse momentum, mass, and scattering angle is given below:

$$M \;=\; (2p_\perp)/\sin\hat\theta \tag{D.15}$$
$$(d\sigma/dp_\perp\, dy)_{y=0} \;=\; \int dM[d\sigma/dM\, dp_\perp\, dy]_{y=0}$$

Integrating over the dijet mass we again have divergences associated with the t channel and u channel exchange peaks. We find that, ignoring those divergences and setting $Z_{min} = 0$, we can set the transverse momentum equal to half the invariant mass. We then use our results as found in D.14 along with the relationship appropriate at the Jacobean peak. The differential cross-section for dijets as a function of the transverse momentum of one of the jets can be exactly integrated for cutoff Z_{min}:

$$p_\perp^3 \left(\frac{d\sigma}{dp_\perp\, dy} \right)_{y=0} \;\sim\; 2L_{gg} \left(\frac{9\pi\alpha_s^2}{16} \right) \left[\left(4 - \frac{8}{30}\right) - 4\,\ln(1 - Z_{min}) \right]$$
$$\sim\; M^3 \left(\frac{d\sigma}{dM\, dy} \right)_{y=0} (1/14),\ p_\perp = M/2 \tag{D.16}$$

As we see, from looking at Fig. D.6, this expression is a reasonable representation of the CERN collider data on the transverse momentum of dijet events; it is just the mass distribution scaled down by a factor of 2, $p_\perp \sim M/2$.

What about scaling behavior as a function of $\bar{p}p$ center-of-mass energy? Looking at Eq. D.14 we expect that the cube of the mass times the differential cross-section should be a function of the scaling variable τ only. The Jacobean peak

relation between transverse momentum and invariant mass can also be used with $p_\perp$ distributions. I is defined in Fig. D.7.

$$
\begin{aligned}
2\pi(I) \equiv p_\perp^3 \left(\frac{d\sigma}{dp_\perp \, dy} \right)_{y=0} &= F(\sqrt{\tau}) \\
&= 2L_{gg} \left(\frac{9\pi\alpha_s^2}{8} \right) \left(\frac{27}{4} \right) \\
&\sim (1 - 2p_\perp/\sqrt{s})^{12}
\end{aligned}
\tag{D.17}
$$

The invariant scaled cross-section is shown in Fig. D.7 along with Collider data. The relationship of D.17 to (I) is proven only later in Section E. Clearly scaling holds, and both the shape and the absolute magnitude are adequately represented by the hand estimate. Note that $(\hbar c)^2 = 4 \times 10^5 \ nb \cdot GeV^2$, so that the vertical scale is indeed dimensionless and of order $\pi\alpha_s^2$ (with $\alpha_s = 0.2$). Note also the divergence of the data at low $p_\perp$ with respect to the hand estimates. This effect (due to gluon evolution) is discussed later.
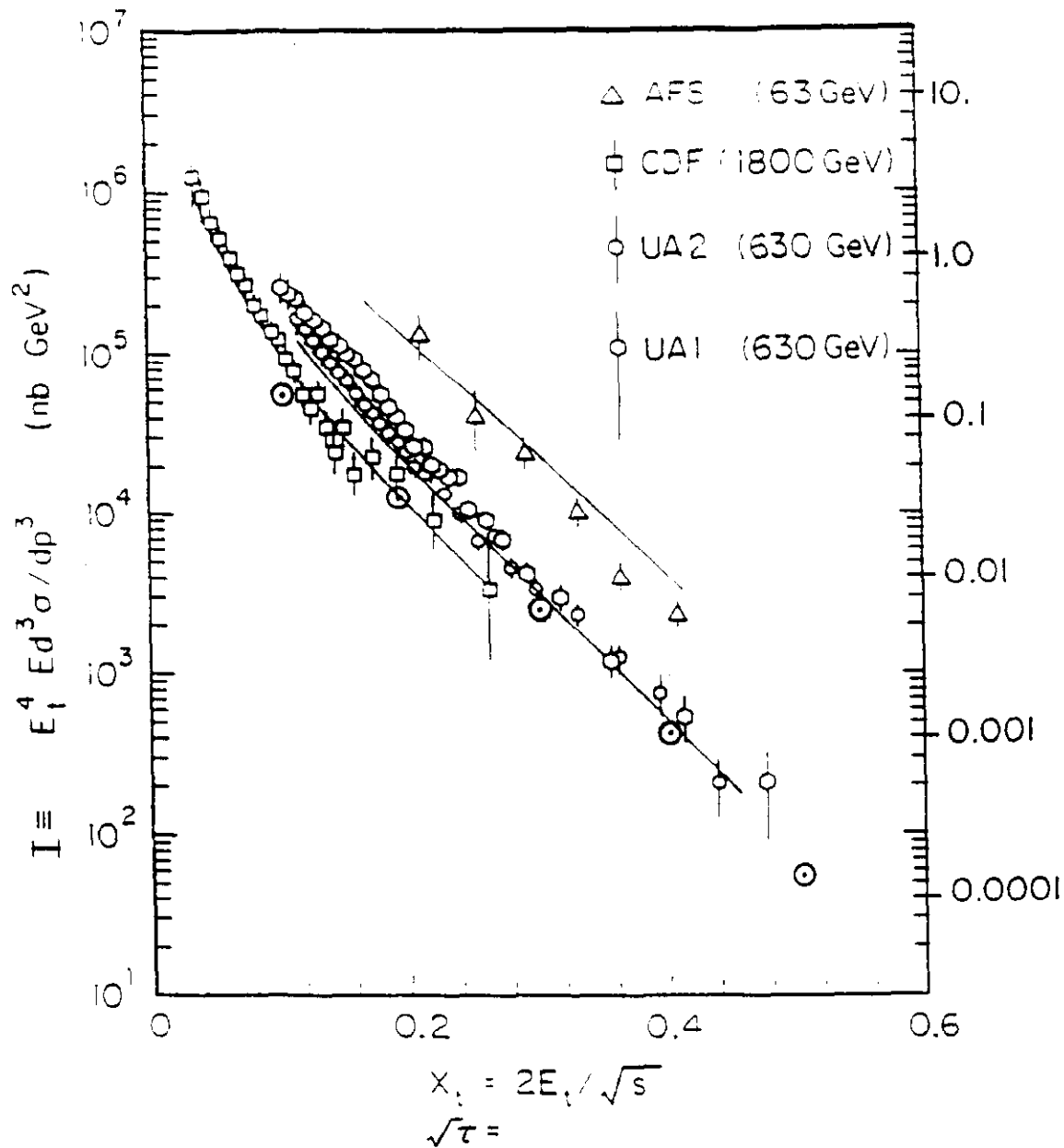
Figure D.7: Scaling of jet data from $\sqrt{s} = 0.063$ TeV to $\sqrt{s} = 1.8$ TeV. Hand estimates are shown as ⊙ points.

Indeed, the data are in reasonable agreement with the scaling prediction. This means that not only do we observe scaling of jet production as a function of center-of-mass energy, but that the functional form of that scaling can be gotten using the gluon distributions. Note that the transverse momenta only go out to about 200 GeV for the Tevatron data, which means that the masses go out to about 400

GeV or x values of about 0.2. As we know from looking at the source distributions (see Fig. B.9), this data is in the regime where the gluon sources dominate. Since in addition we know that the gluon-gluon cross-section is much larger than the quark anti-quark cross-section, this is a posteriori justification for the assumption that the dijet data is dominated by gluon-gluon scattering.

Thus far we appear to have successfully estimated the mass and transverse momentum distribution of dijet events, the angular distributions, and the center-of-mass energy scaling behavior. We can also ask about the "low" transverse momentum cross-section. Looking at Eq. D.16, under the approximation that we're dominated by transverse momenta near the Jacobean peak we expect the doubly differential cross-section as a function of the square of the transverse momentum to go like one over the transverse momentum to the fourth power times some scaling function. Obviously that transverse momentum to the fourth power is a residual reflection of the underlying Rutherford scattering process.

$$
\left(\frac{d\sigma}{dp_\perp^2 \, dy} \right)_{y=0} \sim \frac{1}{p_\perp^4} \left[F(\sqrt{\tau}) \right] \tag{D.18}
$$
$$
\tau = 2p_\perp / \sqrt{s}
$$

At fixed transverse momentum as the center-of-mass energy increases, the x value of the gluon source decreases. Therefore the cross-section at fixed transverse momentum rises very rapidly because the gluon source distribution rises rapidly with x. At low transverse momenta we take the strong fine structure constant, α_s, to be 0.5 since we are at a lower q^2 value. If the scale of transverse momenta is a few GeV, the cross-section is mb. This is, of course, the same order-of-magnitude as the total inelastic cross-section, which means that at very high center-of-mass energies we expect substantial contributions to the total cross-section due to minijets with transverse momenta of the order of a few GeV.

$$\alpha_s \sim 0.5 \tag{D.19}$$

$$\left(\frac{d\sigma}{dp_\perp \, dy}\right)_{y=0} = \frac{7.3 \, mb}{p_\perp^3} \left[1 - \frac{2p_\perp}{\sqrt{s}}\right]^{12}$$

In fact, this is just what is observed. In Fig. D.8 we show the inclusive jet cross-section as a function of transverse momentum for low transverse momentum jets. As shown in the figure, those jets dominate over the single particle data. We also make a hand estimate at low transverse momentum using Eq. D.19. At least on the scale of 20 GeV and above it is a reasonable ballpark estimate of the actual data. A complete calculation is shown as the smooth curve in Fig. D.8. The total cross-section for jets above say 3 GeV transverse momentum is predicted to be of order 20 mb at the Fermilab Collider. This means that jets are comparable to the total inelastic cross-section. Note that, as before, our hand estimate (which ignores evolution) falls below the data at low $p_\perp$.
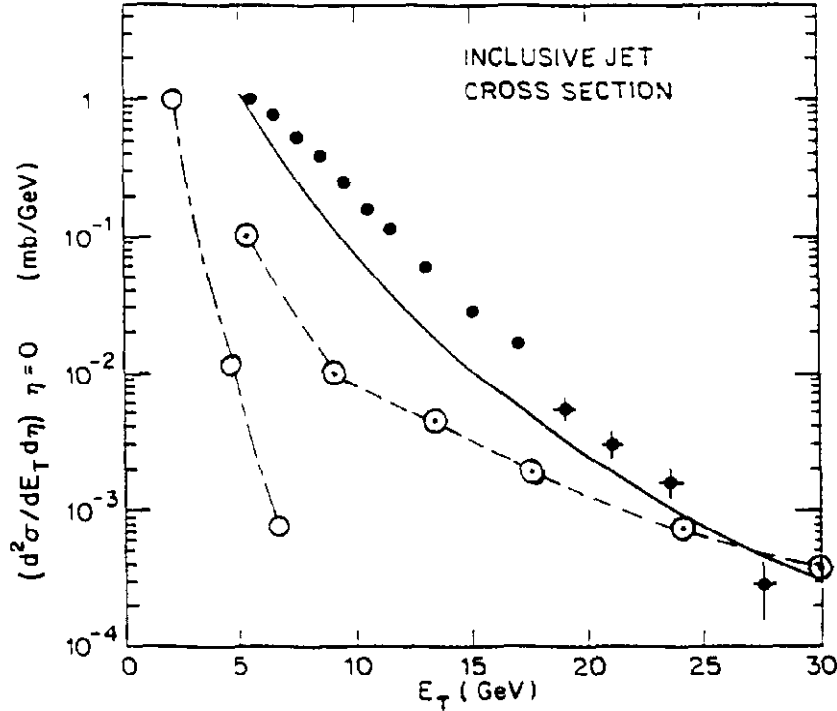
Figure D.8: Jet distributions from UA1 for low $p_\perp$. Also indicated are a QCD calculation (—), single particle data (O) and a hand estimate (⊙).

A propos of the rising cross-section for jets at fixed transverse momentum

75

as a function of center-of-mass energy, we should note that we have assumed a particular form for the gluon distribution. This choice of form was guided by classical bremsstrahlung in that the momentum distribution for gluons at low x approaches a constant. That is certainly true in lowest order, but as you recall the gluon distributions evolve through various radiative and pair production processes. In general, that evolution will tend to reduce all the distributions at high x and have them pile up (due to radiative processes) at low x. For example, we derived the form shown in Eq. B.11, $xg(x) \sim \exp\left[d\ln\left(\frac{x_0}{x}\right)\right]$, which diverges as $x \to 0$. If the gluon number distribution diverges as x approaches 0 faster than one over x, the minijet distribution at fixed transverse momentum rises rapidly with s.

$$xg(x) = \frac{7}{2}(1-x)^6 \exp[\alpha_s b \, \ln(x_0/x)]$$

$$\left(\frac{d\sigma}{dydp_\perp}\right)_{y=0} \sim \frac{1}{p_\perp^3}\left[1 - \frac{2p_\perp}{\sqrt{s}}\right]^{12} e^{\left[2\alpha_s b \, \ln\left(\frac{\sqrt{s}}{p_\perp}\right)\right]}$$

(D.20)

Some authors call this the "gluon bomb," which means that the singular gluon distribution causes the minijet cross-section to rise very quickly with the center-of-mass energy. It will be interesting to see (at higher energy colliders) exactly what the center-of-mass energy dependence of low $p_\perp$ jets is. The fact that the cross-section might violate the Foissiart bound means that our assumptions based on the impulse approximation are breaking down.

Let us now look at a process of which is related to dijet production, the production of prompt photons. The Feynman diagrams for this process have already been shown in Fig. B.4. Recall that they have fermion propagators, the annihilation piece behaving as one over $\hat{s}$ and the exchange piece going as one over $\hat{u}$. Compared to the jet cross-section, we have a 2 → 2 process in both cases. For the jets we have an amplitude squared which has an α_s term at each vertex, whereas for the prompt photons we have an α_s at the gluon vertex and an α times the square of the quark charge at the photon vertex. Ignoring the other differences in the 2 → 2 process cross-sections, and just counting coupling constants and source functions we get a rough prediction for the prompt photon to dijet cross-section.

76

$$\sigma_{J\gamma} \sim \alpha Q_u^2 \alpha_s [xu(x)xg(x)]$$

$$\sigma_{JJ} \sim \alpha_s^2 [xg(x)xg(x)] \tag{D.21}$$

$$\sigma_{J\gamma}/\sigma_{JJ} \sim \left[\frac{\alpha Q_u^2}{\alpha_s}\right]\left[\frac{xu(x)}{xg(x)}\right] = \left[\frac{\alpha Q_u^2}{\alpha_s}\right]\left[\frac{L_{ug}}{L_{gg}}\right]$$

We again assume that the quark distribution is dominated by the up quarks because we have a quark charge squared factor that favors them. At low $p_\perp$, we are operating in the small τ region where we expect the sea to dominate even in $\bar{p}p$ collisions. That assumption leads to the estimate shown below:

$$\alpha_s \sim 0.2, \ \bar{u}(x) \ \text{sea} \tag{D.22}$$

$$\sigma_{J\gamma}/\sigma_{JJ} \sim 9.2 \times 10^{-4} \left[1 - \frac{2p_\perp}{\sqrt{s}}\right]^2$$

Data from the CERN collider on the differential cross-section as a function of transverse momentum for jets and prompt photons is shown in Fig. D.9. The hand estimate points come from Eq. D.22, using the measured jet distribution to scale down to the prompt photons. Clearly this relative scaling works out rather well and gives us confidence that our hand estimates will give us a reasonable estimation of the prompt photon cross-section.
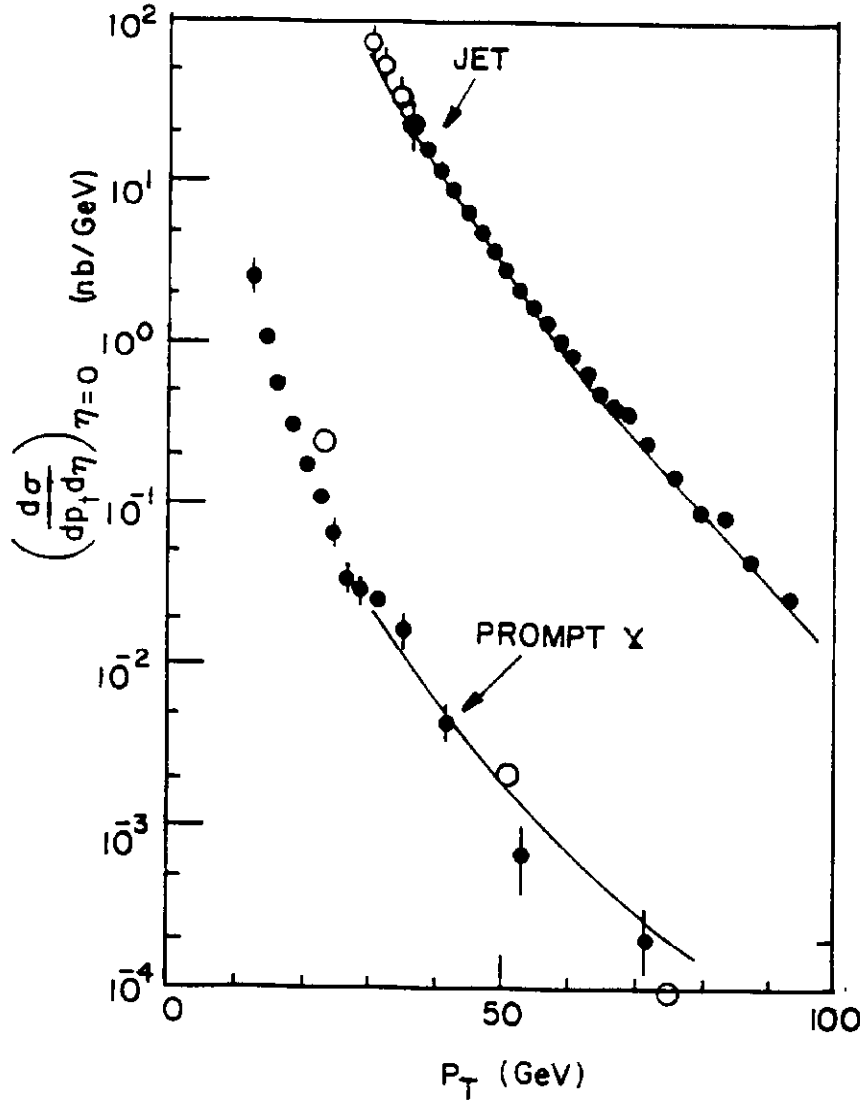
Figure D.9: Data from UA2 comparing $p_\perp$ distributions of jets and single prompt photons. Hand estimates are shown as o points.

There is a further point to be extracted from the data when we look at the angular distributions of the $2 \rightarrow 2$ processes. For a vector boson propagator we have an amplitude going like one over the momentum transfer squared, whereas for fermion propagator we get a dependence for the amplitude which goes like one over the momentum transfer. This means that the differential cross-section goes like one over $\hat{t}^2$ or one over $\hat{t}$ in the case of vector and spin or propagators respectively.

The angular distribution in the two cases is, in fact, different which is something we ignored in comparing the cross-sections.

$$A \sim 1/q^2, \ A \sim 1/(\not{q} + m)$$
$$d\hat{\sigma} \sim 1/\hat{t}^2, \quad \sim 1/\hat{t} \qquad \qquad (D.23)$$
$$d\hat{\sigma}_{J\gamma}/d\hat{\sigma}_{JJ} \sim (1 - \cos\hat{\theta})$$

CERN Collider data on the ratio of the angular distribution is shown in Fig. D.10. The smooth curve is an exact calculation whereas the hand estimate is the dotted curve which is simply a linear dependence on the cosine of the scattering angle. Note that the data does not extend down to small $\hat{\theta}$ because of the problem of identifying the jet in the beam direction. Obviously this data gives us extra confidence that we understand in some detail the $2 \to 2$ processes, which are different in the case of jets and prompt photons.
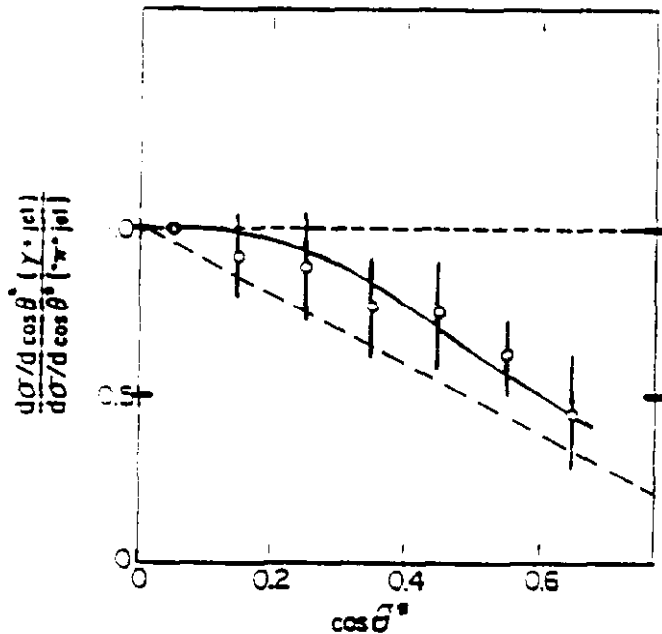
Figure D.10: Data from UA2 comparing the angular distributions of photons and jets. Hand estimates are shown as the (- - -) curve.

Another use of the jet distribution is to set limits on possible substructure of the partons. To begin, we make the observation that at 2 TeV a mass of 200 GeV for the dijet system implies an x value for the partons of 0.1. That means that we are dominated by gluons as a source distribution. We note that the present

79

Tevatron luminosity is such that we cannot yet study quark jets, because the maximum accessible x value for the partons is too low to be in a regime where quark jets dominate. When one gets to higher luminosity, one can vary the x value and study possible changes of jet composition as a function of x. That will be a more interesting and extensive data set. In the meantime, we know that pointlike elastic scattering gives us a transverse momentum distribution that goes like one over $p_\perp^3$ for Rutherford like scattering modified by a factor indicating the partonic distribution functions.

$$\frac{d\sigma}{dp_\perp} \sim \frac{1}{p_\perp^3}[1 - 2p_\perp/\sqrt{s}]^{12} \qquad (D.24)$$

In Fig. D.11 we show CERN Collider data on the transverse momentum distribution of jets at the highest available values of $p_\perp$. Hand estimate points come from taking the data point at 50 GeV transverse momentum as a normalization point and using Eq. D.24 to scale to the highest values from that point. Clearly they are in reasonable agreement with the actual data. The smooth curves are the result of an exact calculation for a composite scale for which the quarks have substructure. Obviously if the quarks have substructure then it is Rutherford scattering all over again. The cross-section at a fixed transverse momentum will be larger than that expected if there were no substructure. It is clear from this data, that that composite scale has a lower limit of a few hundred GeV. Subsequent Tevatron data will push up this limit.
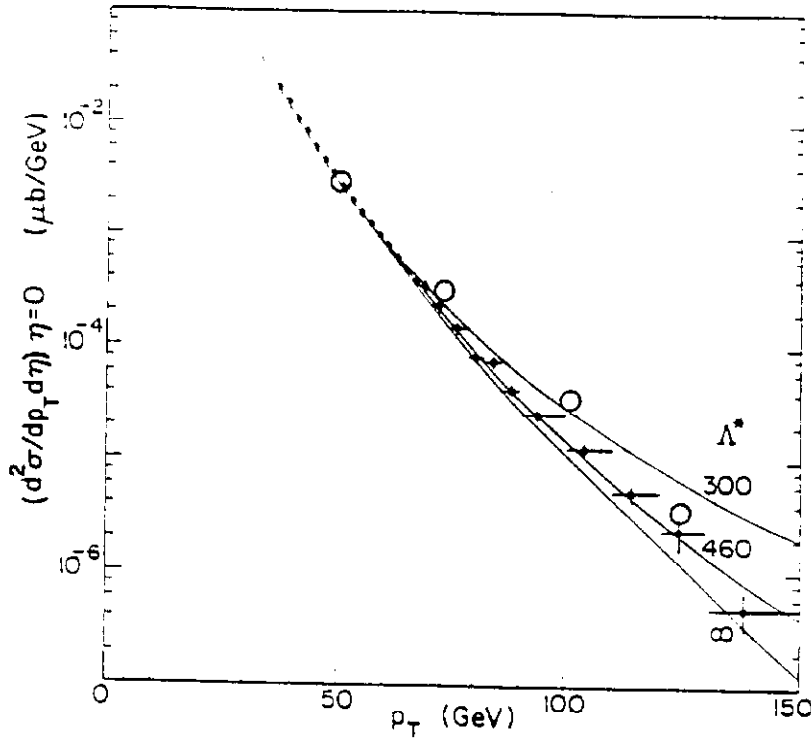
Figure D.11: UA2 data on high $p_\perp$ jet distributions. Hand estimates normalized to $p_\perp = 50$ GeV are shown as O points. Smooth curves are composite calculations.

The dijets are the jet topologies with the most copious rate. However, other topologies are easily observed. For example, in Fig. D.12 we have a three jet event from UA1 with a total transverse energy of 200 GeV. If one remembers two to three processes, the bremsstrahlung cross-section is down by a factor something like α_s with respect to the $2 \rightarrow 2$ process. However, α_s is a quantity of order 0.1, so the three jet to two jet cross-section is finite and a reasonably large number. In fact, one can try to make estimates and extract α_s from that ratio. The number one gets is comparable to that which one gets in looking at W plus jet topologies versus W without jet activity. However, in the latter case the systematics on the α_s determination are better. An additional point to make is that multijet events are experimentally common, but are not well understood theoretically. It is important to have as complete a theoretical treatment of these events as possible to confront the data.

$E_T = 68.2$ GeV

$E_T = 76.2$ GeV

$E_T = 54$ GeV
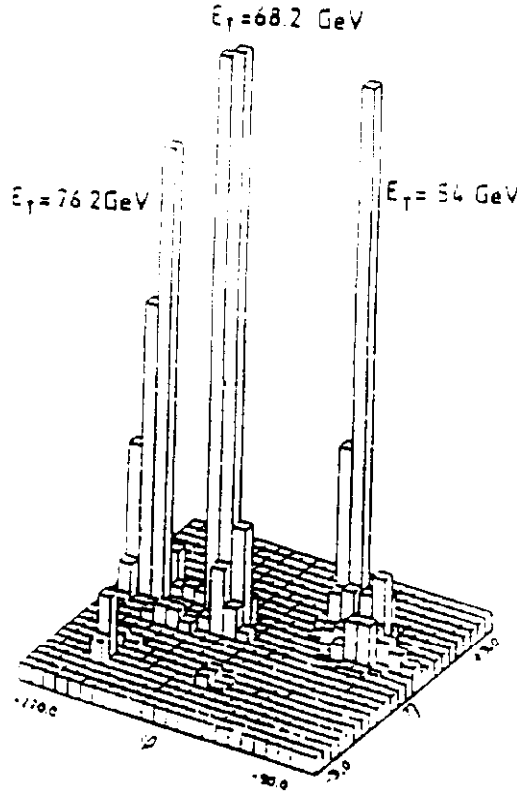
Figure D.12: Lego plot of a 3 jet event from UA1. Total E_T is ~ 200 GeV.

As a final topic for this Section we will consider heavy flavor production. The topic is open heavy flavor production, whereas in Section C we considered hidden heavy flavor production. In Section B we already tabulated the cross-section for gluon fusion production. There are two Feynman diagrams. One is annihilation into a gluon propagator which gives a one over $\hat{s}^2$ piece. The other one is the gluon fusion mechanism with exchanged heavy quark giving us a one over $\hat{t}$ or one over $\hat{u}$ piece. The cross-section for quark anti-quark pairs far above threshold is two orders-of-magnitude smaller than that for the elastic scattering of gluons off gluons (at $\hat{\theta} = 90^\circ$). This fact has implications for heavy flavor production when considering competitive $2 \to 3$ processes.

$$\frac{d\hat{\sigma}(gg \to gg)}{d\hat{\sigma}(gg \to Q\bar{Q})} = \frac{9/2[27/4]}{3/8[7/18]} \sim 200$$

$$\frac{d\sigma}{dM} = 2L_{gg}[\Delta y] \ [d\hat{\sigma}\hat{s}] \ /M^3 \qquad (D.25)$$

$$\sigma_{Q\bar{Q}} \sim 2L_{gg}[\Delta y] \ [d\hat{\sigma}\hat{s}] \ /(2)(2M_Q)^2$$

$$(d\hat{\sigma}\hat{s}) \simeq \frac{3\pi\alpha_s^2}{8}(7/18)$$

We will adapt our results for the dijet differential cross-section as a function of mass. We further assume that the cross-section at threshold rises very steeply to its value when $\hat{s} >> 2M_Q$. We then integrate over all masses above threshold to get the total quark anti-quark cross-section. In order to avoid exchange peaks, we assume that the partonic differential cross-section is just the cross-section at 90^0 far above threshold as we did in the jet case. Since we have been making some rather rash approximations, we expect the cross-section will only be good to an order of magnitude. Looking at Eq. D.25, we can see that if the τ value is small (so that the gluonic source functions are effectively constant), the cross-section for quark anti-quark just goes like one over the quark mass squared.

$$\sigma_{Q\bar{Q}} \sim 1/M_Q^2 \text{ at small } \sqrt{\tau}$$

$$(D.26)$$

$$\sqrt{\tau} \sim 2M_Q/\sqrt{s}$$

Predictions for heavy flavor production as a function of center-of-mass energy are shown in Fig. D.13. Also included in that figure are charm quark data and data on beauty particle production from both UA1 and a lower energy fixed-target experiment.
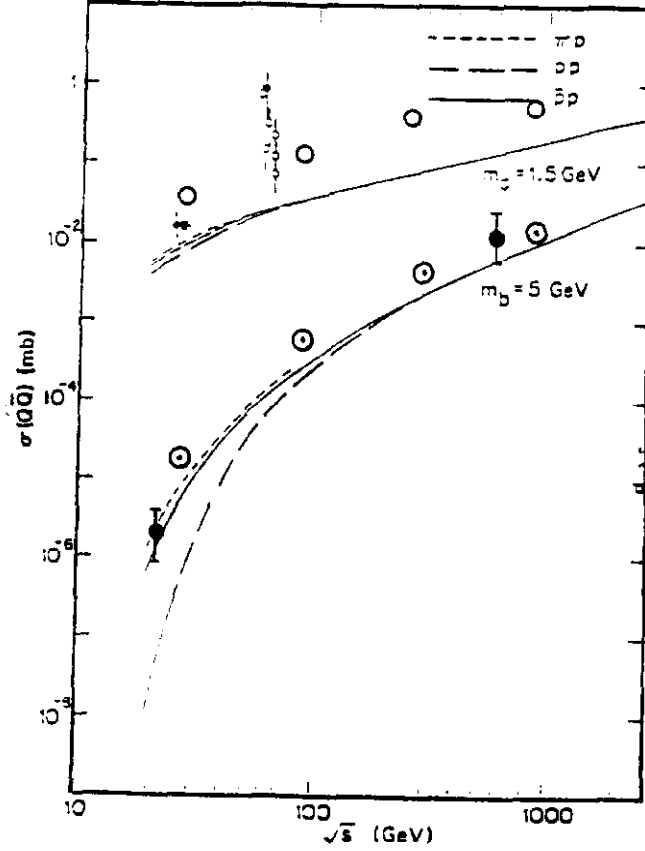
Figure D.13: Heavy flavor production as a function of $\sqrt{s}$. Charm data at $\sqrt{s} <$ 100 GeV are from Fixed-Target or ISR experiments. Beauty data come from UA1 and WA78. Hand estimates of $\bar{D}D$ are given as O points, while those for $\bar{B}B$ are scaled from the exact $\bar{D}D$ calculation and are given as ⊙ points.

For comparison to the exact calculations (shown by the smooth curves) we have made hand estimates of charm particle production using Eq. D.25. We have previously commented on the crude approximations. These hand estimates are surprisingly close to the data and to the exact prediction. This fact gives us some confidence in what we have done to obtain the hand estimate. In order to get hand estimates for the $B\bar{B}$ system we took the exact $D\bar{D}$ calculation and made a relative scaling using the formulae giving in Eq. D.25. This procedure yields points quite close to the data points. We can reproduce the sharp threshold behavior that we see for the $B\bar{B}$ cross-section in a simple way. Clearly at the Tevatron Collider light quarks such as c and b have low τ values and so scale like one over M^2 as one naively expects. At the Tevatron Collider, where the square root of τ is 0.0015 and 0.005 for Ds and Bs respectively, the cross-section is quite substantial. It is

about 300 microbarns for Ds and about 30 microbarns for Bs.

$$\sqrt{s} = 2 \text{ TeV} \qquad \sigma_{D\bar{D}} \sim 300 \ \mu b \qquad\qquad \text{(D.27)}$$

$$\sigma_{B\bar{B}} \sim 30 \ \mu b$$

Although the simple picture appears to be verified by data, and appears to be easy to hand estimate, there are some fine points in heavy quark production. As we see in Fig. D.14 for $D\bar{D}$ production, incident pions appear to be more efficient for making $D\bar{D}$ at low center-of-mass energy than incident protons.
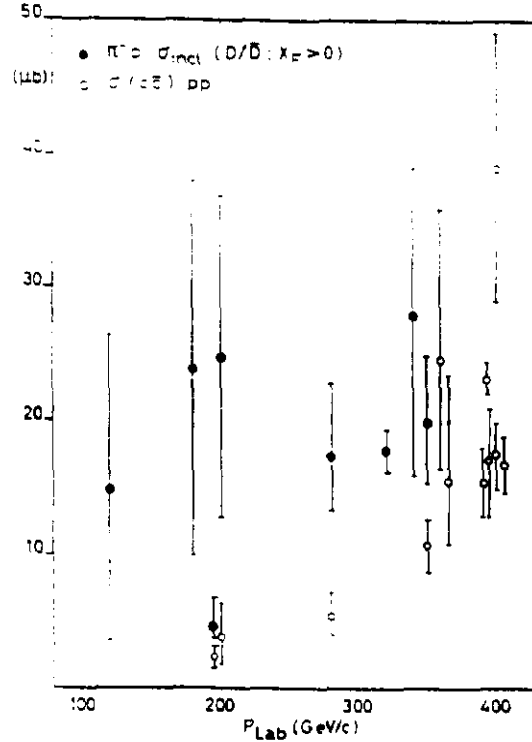

Figure D.14: $D/\bar{D}$ production in πp and pp interactions as a function of π or p momentum.

In fact, the partonic cross-section at 90^0 for light quark anti-quark annihilation into heavy quark anti-quark, relative to the cross-section for gluons fusing into heavy quark anti-quark has a ratio of order one. Thus at high mass (or large τ), i.e. near threshold, since the partonic cross-sections are comparable, the quark source functions will dominate over the gluon source functions. In that case, since the pions have valance anti-quarks to annihilate, whereas the protons require sea

85

anti-quarks, we expect the pions will be more efficient in making charm particle pairs.

$$\frac{d\hat{\sigma}(q\bar{q} \to Q\bar{Q})}{d\hat{\sigma}(gg \to Q\bar{Q})} = \frac{4/9}{3/8(7/18)} \sim 3.0$$

$$x \geq 0.3 \quad \sim \quad \sqrt{\tau} \sim 2M_Q/\sqrt{s} \qquad (D.28)$$

$$2\,TeV = \sqrt{s}, M_Q > 300\ GeV$$

At a center-of-mass energy of 2 TeV, the point where quark sources become important relative to gluon sources corresponds to masses of the heavy quark above 300 GeV. This fact is again an argument for $\bar{p}p$ vs. pp colliders.

There are other soft processes which are not calculated in perturbative QCD. In Fig. D.15 we show a schematic quark diagram for leading particle effects where a proton fragments into a proton, neutron, Λ^0, or Λ_c^+.
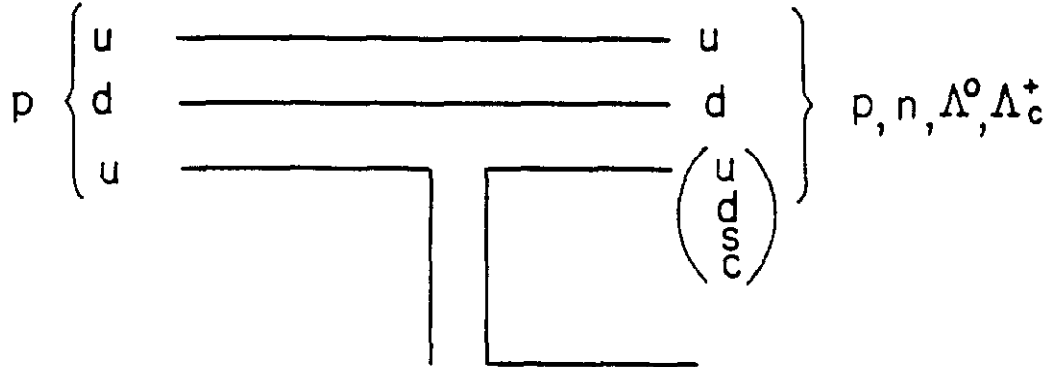
Figure D.15: Quark diagram for leading particle effects in $p \to p, n, \Lambda^0$, and Λ_c^+.

We know that for a proton fragmenting into a proton or neutron, the average x value (or the average inelasticity) in the event is about a half. That being the case you might expect to pick up a $c\bar{c}$ out of the sea of hadronic junk and find a fast forward Λ_c^+. Data on this process are not without some controversy. Data from the ISR at CERN on the x distribution of the Λ_c^+ are shown in Fig. D.16. Note that the scale for the differential cross-section is several hundred microbarns, which means that the cross-section for Λ_c^+ at the ISR for leading particles is at

least 100 microbarns. The size of the total charm cross-section then clashes with the cross-section estimates for $D\bar{D}$ which we saw back in Fig. D.13.
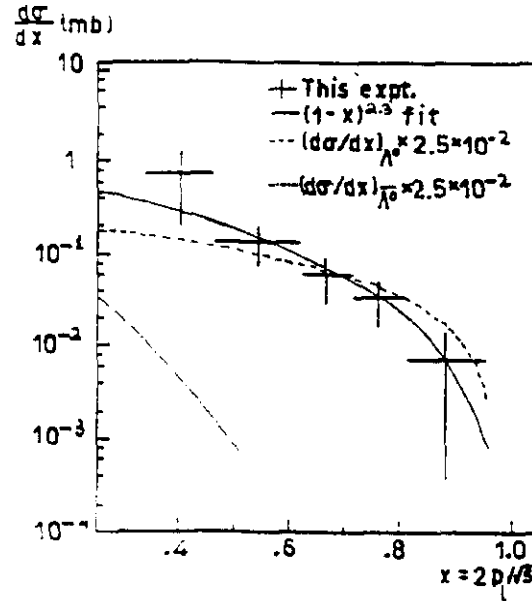

Figure D.16: CERN ISR data on the x distribution of Λ_c^+ baryons for $x > 0.3$.

Either this data is not correct or we need to take the soft leading particle effects into account. Since this topic is rather far afield for us, and since we have avoided all " lns" physics so far, we will now drop the subject.

So far in heavy flavors we've only talked about $2 \rightarrow 2$ processes. In fact, there are competitive $2 \rightarrow 3$ processes. For example, as seen in Fig. D.17, one can compare fusion to a diagram for gluon-gluon scattering followed by virtual gluon decay into a $Q\bar{Q}$ pair.
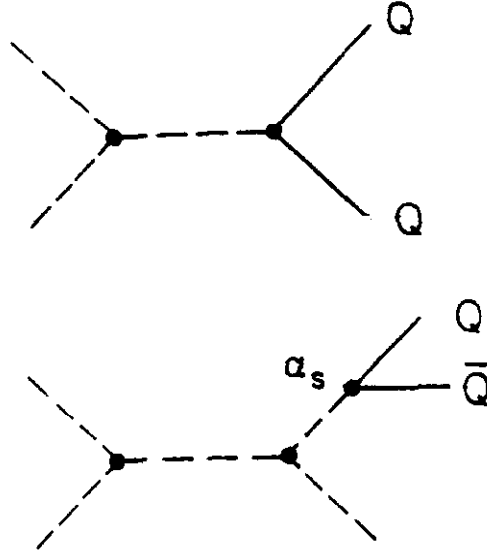
Figure D.17: Feynman diagrams for $Q\bar{Q}$ production in a 2 → 2 "fusion" process and in a 2 → 3 "gluon splitting" process.

The differential cross-section for gluon elastic scattering vs. gluon fusion into quark anti-quark pair at 90^0 is given in Eq. D.25. The ratio is about a factor of 200. Hence, the 2 → 3 process where an elastically scattered gluon can virtually disassociate into quark anti-quark pair leading to a three particle final state, is competitive with the 2 → 2 process because the coupling constant α_s is not overwhelmingly small relative to the 2 → 2 cross-section (see Eq. B.9). Note that aside from kinematic factors, all heavy quarks are produced equally because gluons are flavor blind.

$$\frac{\sigma(gg \to \bar{Q}Qg)}{\sigma(gg \to \bar{Q}Q)} \sim \frac{d\hat{\sigma}(gg \to gg)}{d\hat{\sigma}(gg \to QQ)} \left[\left(\frac{\alpha_s}{\pi}\right) \ln\left(\frac{\hat{s}}{(2M_Q)^2}\right) \right] \qquad (D.29)$$

This means, of course, that in evaluating the charm quark mass, which is a parameter in these calculations, one needs to take all the competitive processes into account. In Fig. D.18 there are a set of curves shown for the charm cross-section as a function of center-of-mass energy. For different values of the charm quark mass one assumes that only 2 → 2 processes contribute. It is obvious that

88

the data, in the context of a 2 → 2 theory, force you to a low value for the charm quark mass.
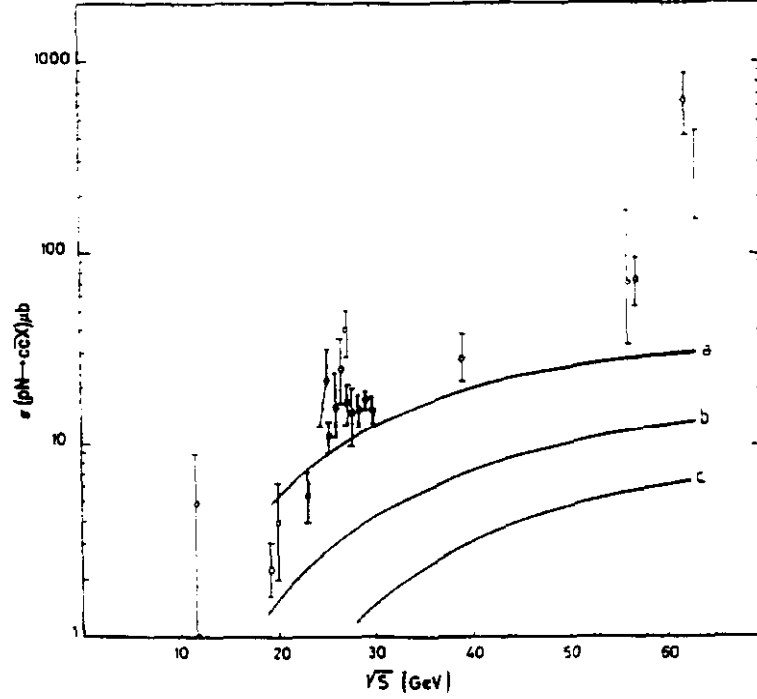

Figure D.18: Dependence of $\sigma(D\bar{D})$ as a function of $\sqrt{s}$ on the parameter m_c for 2 → 2 processes only. The curves labelled a, b, and c refer to $m_c = 1.2$, 1.5, and 1.8 GeV, respectively.

What we mean by low is low relative to say, half the ψ mass, which would lead you to believe that the charm quark has an effective mass of about one and a half GeV. But of course this is entirely spurious because that low value of the charm quark mass comes about by ignoring 2 → 3 processes in the calculation. When they are included, the rising of the cross-section due to the addition of those processes drives up the mass to a value which is compatible with the 1.5 GeV that one expects from spectroscopy. Independent evidence for the existence of this 2 → 3 process will be given in Section E.

One should make a comment about the relative scales of some of the different processes discussed in Sections C and D. The reason we talked about Ws going into lepton plus neutrino or Z going into dilepton was that the major branching ratio for W decays, W into $c\bar{s}$ or $u\bar{d}$, have enormous backgrounds due to dijets at the W

and Z mass which bury the W cross-section by roughly two orders of magnitude. One way to reduce this background is to use some sort of vertex detection scheme to find secondary vertices and identify the fact that there are heavy flavors in the jet which decay weakly. Using our previous estimates for heavy flavor production, we can estimate the $1/M^3$ tail of the gluon fusion mechanism. For $b\bar{b}$ pairs it is about 6 nanobarns per GeV for a mass of the $b\bar{b}$ system of 100 GeV.

$$
\frac{d\sigma(\bar{Q}Q)}{dM} \sim 1/M^3, \ M >> M_Q
$$

$W \to c\bar{s}, \ u\bar{d}$ background

$$
\begin{aligned}
\frac{d\sigma(\bar{Q}Q)}{dM} &\sim \sigma(Q\bar{Q})(8M_Q^2)/M^3 \qquad \text{(D.30)} \\
&\sim 6 \ nb/\text{GeV} \\
\sigma_W/\Gamma_W &\sim 0.7 \ nb/\text{GeV}
\end{aligned}
$$

This rate should be compared to the cross-section divided by the total W width which is still something like an order-of-magnitude smaller. Hence, even if one can achieve a mass resolution for dijets which is equal to the W natural width, and if one can cleanly detect D's in the final state, one is still buried by heavy flavors at the W mass by an order of magnitude. At this time, W's and Z's have only been definitively seen in leptonic final states.

There is at least one quark which is still to be discovered, the top quark. If $M_t < M_W$, then it confuses the limit on the number of light neturinos. A direct measure of V_{bu} would inform on the three generation unitarity of the KM matrix (see Fig. A.4). A measurement of M_Z/M_W limits M_t from being too large, $\lesssim$ 300 GeV, (radiative corrections). Direct limits require $M_t \gtrsim 45$ GeV. Recently, as we will discuss in Section E, large $B/\bar{B}$ mixing has been observed. As shown in Fig. D.19 large mixing means large M_t (propagator effect) or large V_{bu} (generalized GIM cancellation mechanism). If we knew V_{bu} (i.e. $b \to u$ decays) we could choose between the two effects. Note that, in an exactly similar fashion, before charm was found its mass was limited theoretically to $\lesssim 1.5$ GeV because otherwise the $K_S - K_L$ mass difference would be too large.
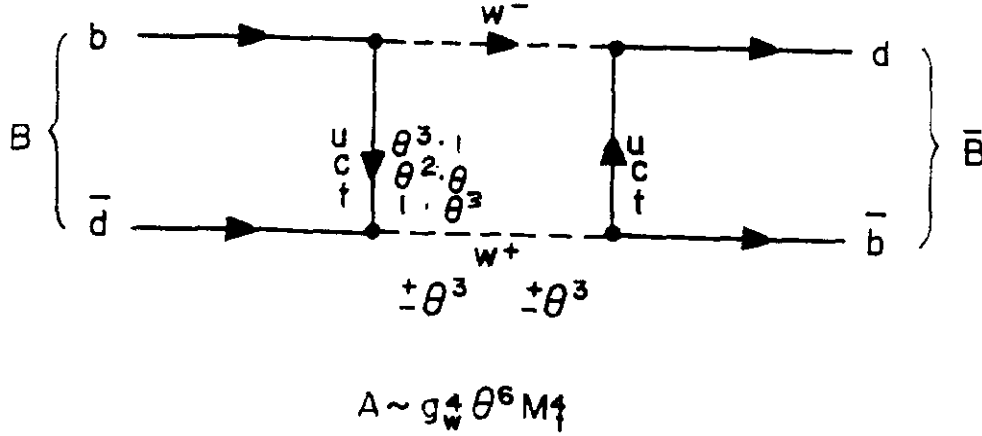
Figure: D.19: Box diagram for $B - \bar{B}$ mixing.

If the top quark is heavy $(M_t > M_W)$ then it decays into $Q \rightarrow Wq$. As we show below, a quark with $M_Q = 120$ GeV is produced at the Tevatron with $\sigma(Q\bar{Q}) = 20$ pb. By comparison, Fig. D.2, $\sigma^{DY}(WW) \sim 8$ pb. The Higgs cross-section, $\sigma^H(WW) \sim 0.2$ pb, is smaller yet again. It is observable (Fig. D.4) because its width is small, so that $(d\sigma/\Gamma)^H_{WW} >> (d\sigma/dM)^{DY}_{WW}$. Thus the biggest source of W pairs is a heavy top quark. For example, a Tevatron run with integrated luminosity of 10 pb^{-1} will yield 200 $t\bar{t}$ pairs (120 GeV top mass), or 200 WW pairs, or five events with μe and large missing transverse momentum.

What about the cross-section for very heavy quarks, a super heavy top or a forth generation. The predictions shown in Fig. D.20 are an exact calculation of heavy quark production as a function of the quark mass. Predictions at three different center-of-mass energies relevant to the CERN Collider and the Tevatron Collider at two different energies are shown. Also shown are hand estimates for a center-of-mass energy of 2 TeV which were calculated using Eq. D.25. It looks as if those estimates are within an order of magnitude of the exact calculation over most of the range of the plot. The estimate assumes gluon sources. We don't expect quark sources to be important until we get into the valance regime where x is say greater than 0.3, or a quark of mass greater than 300 GeV. Note that at 120

GeV quark mass, Fermilab has a 100 fold advantage over CERN in cross-section. It seems unlikely that such a factor can be compensated for by luminosity.
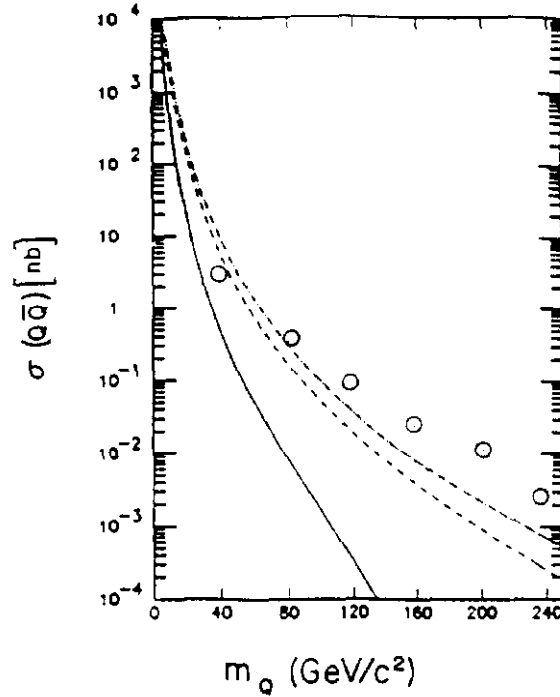

Figure D.20: Heavy flavor production cross-section as a function of quark mass. At $\sqrt{s} = 0.63$ TeV (—), 1.8 TeV (- - -) and 2.0 TeV ($- \cdot - \cdot - \cdot -$). Hand estimates for 2.0 TeV are shown as O points.

This brings our discussion in Section D to an end. In this Section, we have looked at Drell-Yan production of lepton pairs and, by extension, production of gauge boson pairs. We compared that to Higgs production and decay to boson pairs. The bulk of the Section was spent on jets; their angular distributions, their mass and transverse momentum distributions, their scaling properties at different center-of-mass energies, their low transverse momentum minijet cross-section, and whether the gluon bomb explodes at higher center-of-mass energies. We predicted the dijet to jet-direct photon ratio which tells us about the coupling constant and source distribution. We compared the angular distributions, which tells us about the elementary propagators for the two processes. Finally, heavy flavor production was looked at. It indicated the existence of $2 \rightarrow 3$ processes. Heavy flavors also act as backgrounds to other processes such as W and Z production. In all cases, we were able to make a plausible hand estimate for the process.

E. HADRON DECAY KINEMATICS AND POINT PARTICLE
FRAGMENTATION

So far we have been talking about wonderful things like partons; quarks and gluons. It is the nasty little secret of particle physics that the asymptotic states in the real world don't contain any of these objects but consist of color singlet hadrons or leptons. In fact, theoretically it is not at all clear how to write down a consistent field theory without referring to the asymptotically free states—as in the definition of the S matrix. Experimentally, we have to come to terms with the fact that our quarks and gluons, which are colored, fragment into hadrons before they appear to us. We need to be able to relate the jets of hadronic debris to the final state gluons and quarks which are unobservable.

First let's just think about a simplified decay kinematics. We already did two-body decay kinematics where we said that the Jacobean peak was such that the transverse momentum of any jet was half of the dijet mass. Now we have to worry about the jet break up into hadrons. We can think of this as an n body decay with a small transverse momentum ($q_\perp \sim \Lambda$) with respect to the jet axis. The kinematics for this process is shown in Fig. E.1.
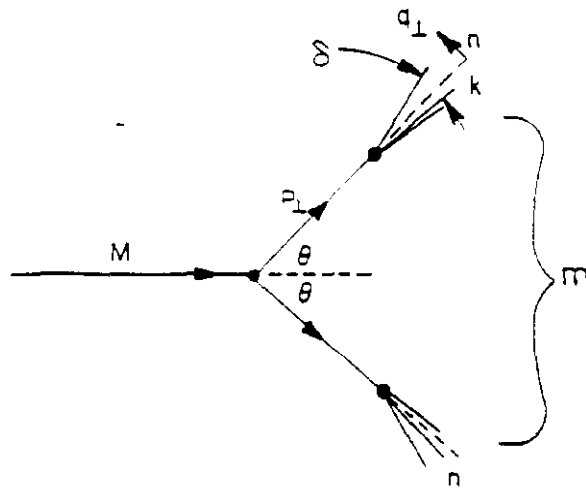
$P_\perp \sim M/2$

$k_\perp \sim P_\perp/n$

$k \sim P/n$

$m \sim M/n$

Figure E.1: Jet kinematics for fragments.

The fragments have a limited transverse momentum, $q_\perp$, with respect to the jet axis and we assume that they share the jet momentum roughly equally. This means that the angle of the fragment with respect to the jet axis is small and the mass of any pair of hadrons between the two jets is the dijet mass divided by the number of fragments.

This simple picture has some immediate consequences if you think about the kinematics. For example, you might ask, why didn't people see jets a long time ago? The answer is fairly simple. The transverse momentum which is intrinsic to the fragmentation processes is $q_\perp \sim \Lambda$ (when α_s becomes ~ 1) or $q_\perp$ about 500 MeV, which is a typical transverse momentum in a soft hadronic interaction. If we would like the two jets to be contained within cones of half angle of 10^0 (45^0) so that the jets take up 40^0 (180^0) out of the total phase space, then they will (not) be observable. The momentum of the fragment, if the jet fragments into five particles, is 2.8 (0.5) GeV. The jet has a transverse momentum of 14 (2.5) GeV. If the jet comes from a parton with x value of 0.2 then we need 70 GeV on 70 GeV

in the center-of-mass. This situation would only begin to obtain at a 10 (0.3) TeV Fixed-Target experiment.

$$
\begin{aligned}
q_\perp &\sim 0.5 \text{ GeV} \\
\delta &\leq \pm 10^0 \ (45^0) \\
k &\sim 2.8 \ (0.5) \text{ GeV}, \ n = 5 \\
p &\sim p_\perp \sim 14 \ (2.5) \text{ GeV} \\
< x > \sim 0.2 \Rightarrow \underline{P} &\sim 70 \ (12.5) \text{ GeV} \\
\sqrt{s} &= 140 \ (25) \text{ GeV}, \ P_0 = 10 \ (0.3) \text{ TeV}
\end{aligned}
\tag{E.1}
$$

What that kind of argument tells you is that at a Fixed-Target machine the jets will be overlapping. They will not stand out as distinct from the fragments of the initial hadrons just on a kinematic basis. In hadronic machines we need to go to the CERN or Fermilab Collider for jets stand out as obvious objects. These arguments are confirmed by the data sets gathered at Fixed-Target and Collider experiments.

As an example of three-body decays we can consider the semi-leptonic decays of B mesons. Typical values of the transverse momentum of the lepton will then be a third of the quark mass. The maximum value of the momentum of the lepton comes when it recoils against the light quark and the neutrino in a quasi two-body decay.

$$
\begin{aligned}
< p_\perp > &\sim M_Q/3 \\
(p_\perp)_{max} &\sim M_Q/2
\end{aligned}
\tag{E.2}
$$

This simple kinematic statement has some implication for determining the elements of the KM matrix. The maximum value of transverse momentum in semi-leptonic decay for an allowed b to c transition is smaller than that of a b to u transition. In particular, $(p_\perp)_{max}$ for $b \rightarrow u$ is half the quark mass of 2 1/2 GeV. The b to c transition cannot provide a lepton with that transverse momentum. The data shows that there is no evidence in semi-leptonic decays for $b \rightarrow$ u transitions. Data from e^+e^- collisions for the semi-leptonic decay distributions of leptons is shown in Fig. E.2. In that figure, the $b \rightarrow$ u curve cuts off at 2 GeV transverse

momentum because $b \rightarrow c + \mu + \nu$ has that value as its kinematic limit. The ratio V_{bu}/V_{bc} is $\sim \theta$ (see Fig. A.4), so that a definitive measurement of V_{bu} would test three generation unitarity of the KM matrix. As yet, this kinematic technique has only set lower limits on V_{bu}.
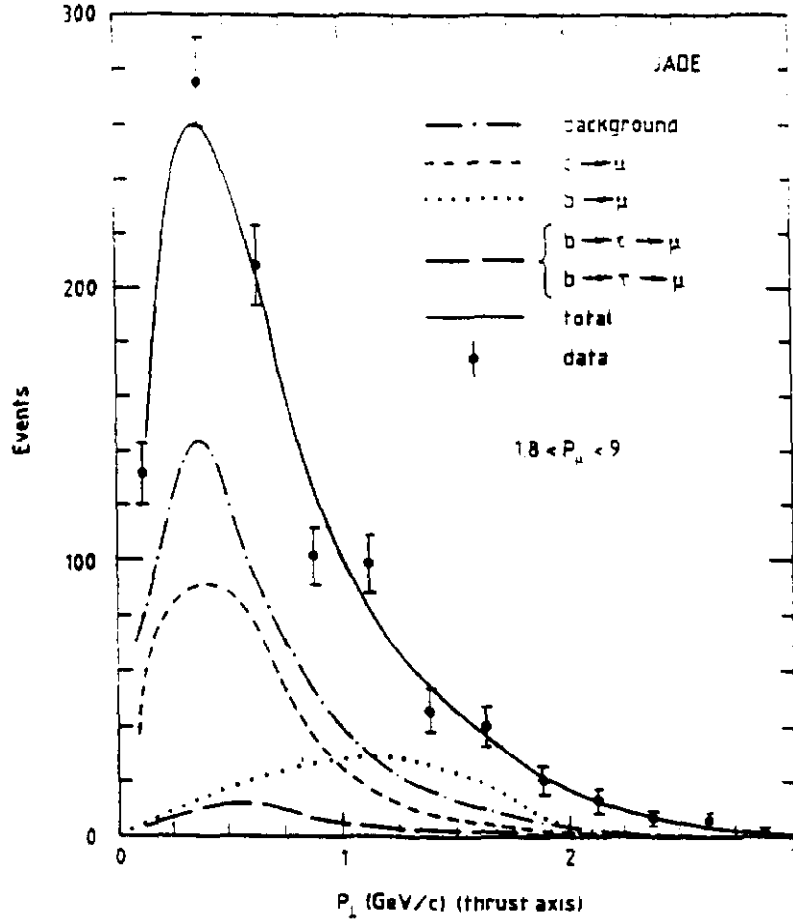

Figure E.2: Inclusive muon $p_{\perp}$ distribution in e^+e^- collisions with contributions from semileptonic decay distributions for $b \rightarrow c\mu\nu$, $c \rightarrow s\mu\nu$ plotted separately.

Turning to proton anti-proton collider data, in Fig. E.3 we show the muon transverse momentum relative to the jet axis for semi-leptonic decays of particles in jets. Using those distributions one can estimate the relative contributions of c and b quarks to the inclusive muon spectrum. Obviously the heavier quarks throw the muons off the axis of the jet and make them more isolated from the decay jet. That isolation is one of the ways that the cross-section for $B\bar{B}$ was measured in our discussion in Section D of the cross-section for heavy quarks as a function

of energy. Obviously heavier quarks will lead to larger transverse momenta with respect to the jet axis in semileptonic decays. That fact is part of the basis for top searches and general searches for fourth generation heavy quarks.
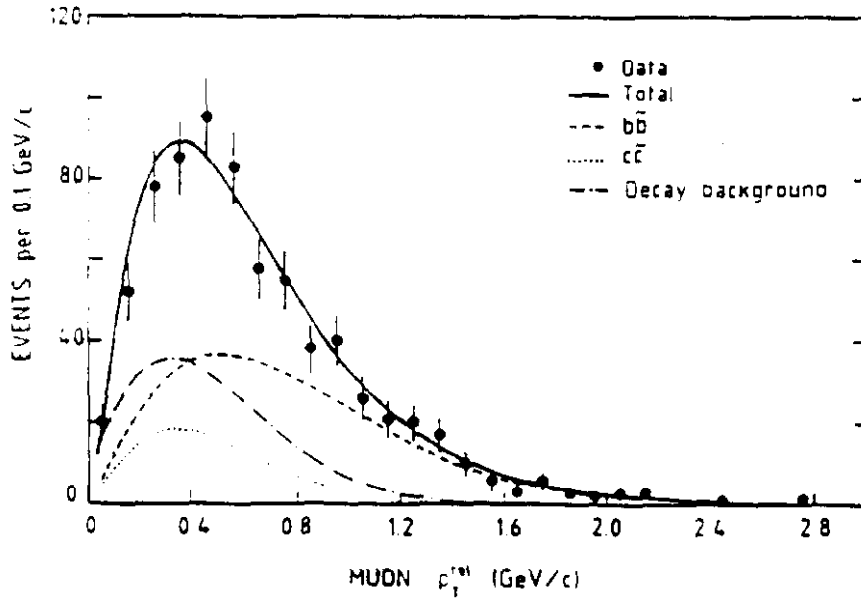

Figure E.3: UA1 data on muon $p_\perp$ relative to jet axis for $q' \to q\mu\nu$ decays.

So much for the leptons in the jet, what about the fragmentation of the jet into the light particles which form the bulk of the jet multiplicity? In Fig. E.4, we show collider data on the multiplicity in a jet as a function of the dijet mass. What we find out is that the jet multiplicity grows logarithmically with the dijet invariant mass.
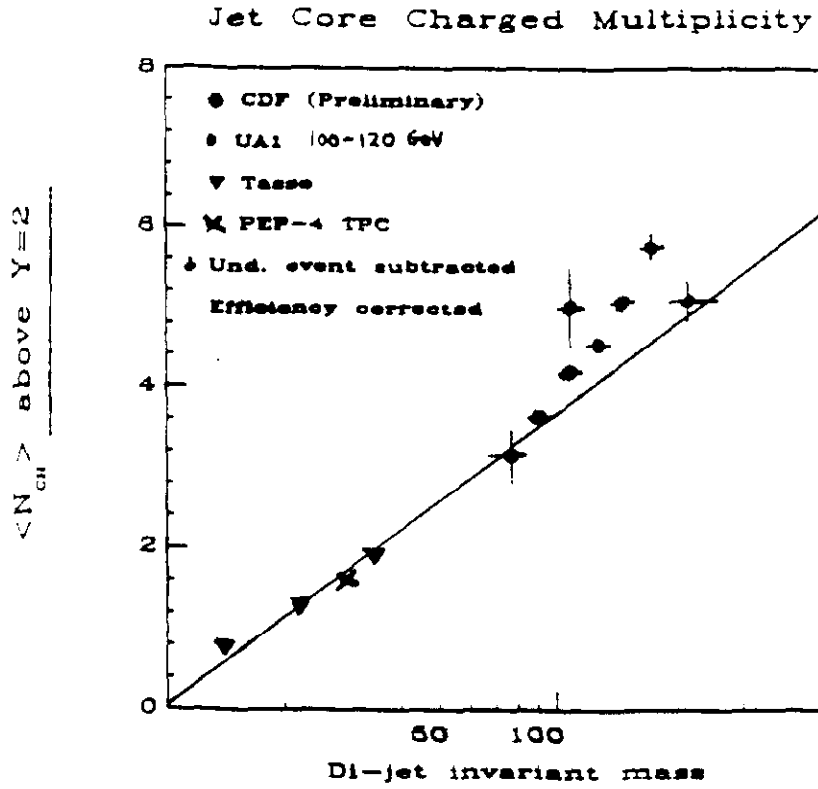
Figure E.4: Collider data on fragmentation multiplicity as a function of M_{JJ}. The line is $< n > \sim \ln(M_{JJ})$.

This behavior is very reminicent of that of the total inelastic multiplicity in colliders as a function of the total center-of-mass energy.

Shown in Fig. E.5 is CDF data from the Fermilab Collider on the rapidity distribution of fragmentation products with respect to the jet axis. What one finds is that there is an indication of a rapidity "plateau," in other words a uniform distribution of rapidity with a tail extending out some units beyond that.
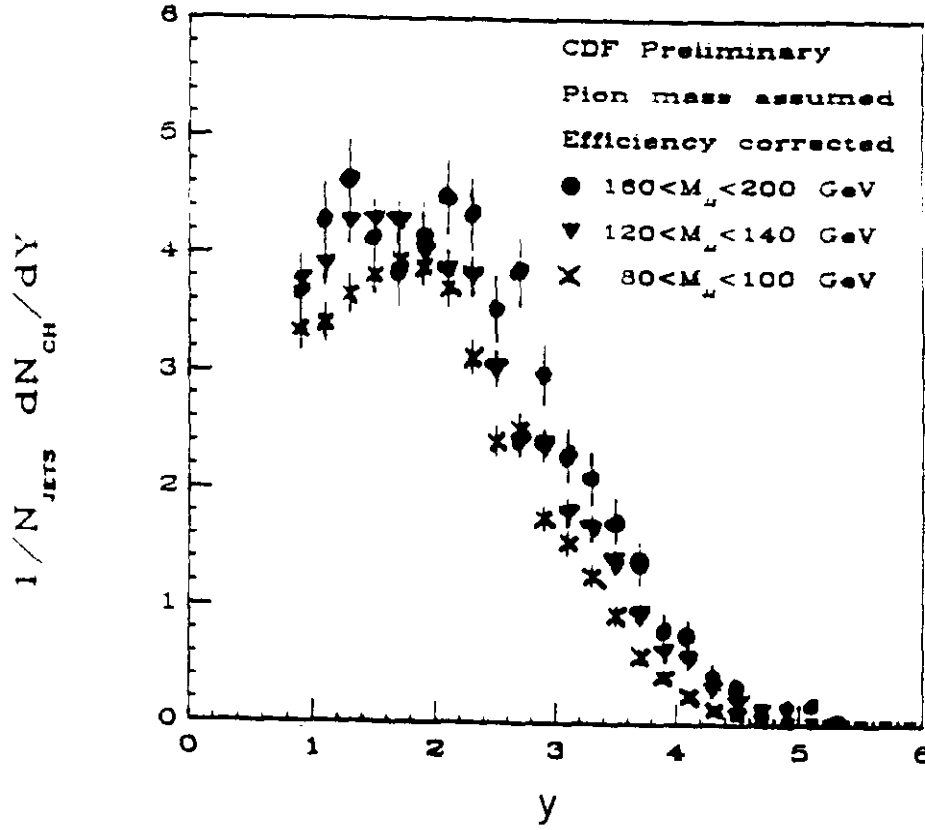
Figure E.5: CDF data on the rapidity distribution of the fragmentation products of jets.

Our job now is to explain those facts about the mean multiplicity and the rapidity distribution. Let's assume that the parton has a momentum p and it fragments into a hadron of momentum k. We define the momentum fraction to be z, so z ranges between 0 and one. These are the same kinematic definitions we have used throughout this note. We define a number density for fragmentation, $D(z)$ which is the probability to find a hadron as a fragment with z between z and $z + dz$. Note that, $D(z)$ describes inherently soft processes, which means that we will be forced to measure $D(z)$ rather than calculate it just as was the case for the "inverse" distribution $B(x) \rightarrow f(x)$.

$$z \equiv k/p, \qquad 0 < z < 1 \tag{E.3}$$

$$D(z)dz$$

This definition tells us that the momentum spectrum of fragments is the convolution over the fragmentation function $D(z)$ of the momentum spectrum of all the parents.

$$
\begin{aligned}
d\sigma/dk &\simeq \int \frac{d\sigma}{dp} D(k/p) \frac{dp}{p} \\
&\simeq \int \frac{d\sigma}{dp} D(z)dz
\end{aligned}
\tag{E.4}
$$

We take a fragmentation function which has a radiative like character similar to what we have assumed for gluons. Integrating the fragmentation function over all z we will get the mean multiplicity, since we have integrated over all the fragments in the jet.

$$
\begin{aligned}
zD(z) &\equiv a(1-z)^\alpha \\
<n> &= \int D(z)dz \simeq a \int_{m/p}^{1} dz/z \\
&\sim a \ln(p/m)
\end{aligned}
\tag{E.5}
$$

This integral is divergent just the way the total number of radiative partons was divergent at very small x. We cut off the integral by taking a lower limit which is defined by the mass of the particle. In that case we find that the mean multiplicity depends logarithmically on the jet momentum. In this way we can explain the logarithmic dependence that we saw in Fig. E.4.

What about the rapidity distribution? One particle phase space is just a four dimensional volume element with the constraint that the particle be on the mass shell. That turns out to be proportional to the rapidity interval, or dz/z. We have already used this result (without proof) in the discussion in Section D on jet scaling behavior.

$$
\begin{aligned}
d^4p\delta(p^2 - m^2) &= d\vec{p}/E = \pi dp_\perp^2 dy \\
\frac{dp_{11}}{E} &\sim dy \sim dz/z \\
<n> &\sim \Delta y \sim \ln(\sqrt{s}/M)
\end{aligned}
\tag{E.6}
$$

100

For light particles z, x, and rapidity are all equivalent variables. If particles are boiling out of the parton and fragmenting in a way controlled merely by phase space, we get a rapidity plateau. Of course, at a certain point one runs out of momentum, since one has to conserve total energy and momentum. In that case you fall off the plateau and are rapidly cut off by the kinematics, $|y| \overset{<}{\sim} \Delta y$. As a final note on kinematics, if you integrate over a uniform rapidity plateau you find the total rapidity interval which depends logarithmically on the center-of-mass energy as in Eq. C.8 which we already discussed. Since this is the inclusive cross-section, the integral is the mean multiplicity. The quantity $< n >$ is easily seen to be logarithmically dependent on the center-of-mass energy.

In Fig. E.6, we show ISR and CERN Collider data on the fragmentation function for light fragments. It is clear that $z \ D(z)$ fits reasonably well to an exponential form, which of course means that most of the fragments are of low momentum with respect to the jet. It is also clear that $D(z)$ is a scaling function, i.e., $D(z)$ is roughly independent of $\sqrt{s}$.
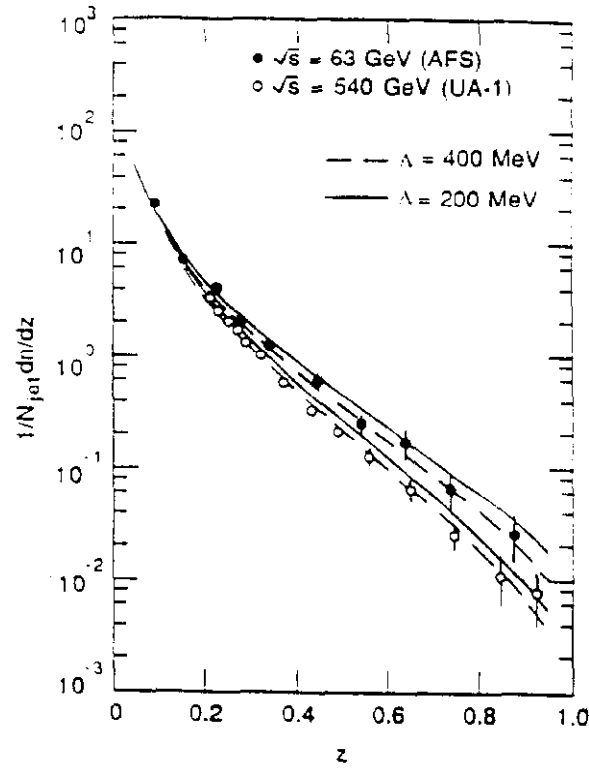
Figure E.6: Collider data on $D(z)$ for light fragments.

In Fig. E.7, we show CERN Collider data from UA2 for both jets and for isolated single particles, which are assumed to be pions in this case. What one sees is the basic shape is not too different between the two types of data. The fragmentation has merely renormalized the $p_\perp$ scale by some multiplicative factor.
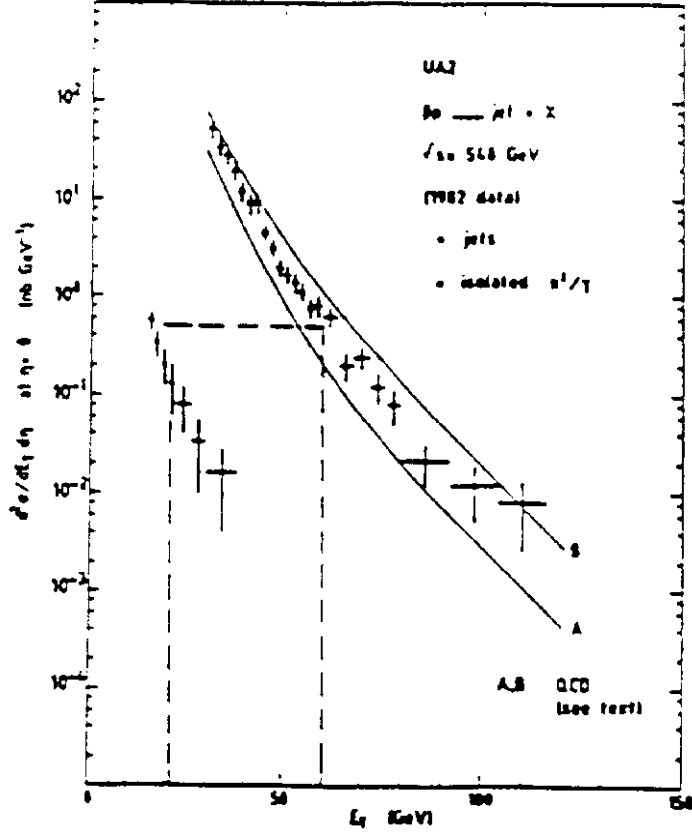
Figure E.7: UA2 data on jet and single particle $p_\perp$ distributions.

Doing the convolution of a simple exponential fragmentation (Fig. E.6) and a $1/p^3$ behavior for the parton momentum (which is what we expect for jet production as we saw in Section D), we get basically the same power law for the fragments. This is a nice simple way to see that the jet and single particle distributions typically look the same with regard to shape, but the single particles are softer because of fragmentation.

$$
\begin{aligned}
zD(z) &\equiv e^{-\beta z} \\
\frac{d\sigma}{dk} &\simeq \int \frac{d\sigma}{dp} D(k/p) dp/p \\
&\sim \int_k^\infty \frac{1}{p^3} \left[\frac{p}{k}\right] e^{-\beta k/p} dp/p \\
&\sim \frac{1}{k} \int_k^\infty \left(\frac{dp}{p^3}\right) e^{-\beta k/p} \\
&\sim \frac{1}{k^3}
\end{aligned}
$$

(E.7)

103

In this regard it is interesting to compare CERN Collider data on prompt photons and the single particles from jets as shown in Fig. E.8. We'll recall from our discussion of prompt photons that the rate of photons with respect to jets is down by both coupling constant and source function factors. The rate is down by a factor of α with respect to the jet cross-section. On the other hand, the jet to π^0 ratio is also down a couple of orders-of-magnitude due to the steepness of the fragmentation function as we saw already in Fig. E.7, although we expect similar shapes for jets (i.e., γ) and fragments.

As we see in Fig. E.8, at higher transverse momentum we expect that the photon (which is a point particle and itself a "jet") will cross the cross-section for π^0s which are hadronic fragments of jets. This means that the (γ/π^0) ratio as a function of transverse momentum will exceed one at high enough transverse momenta.
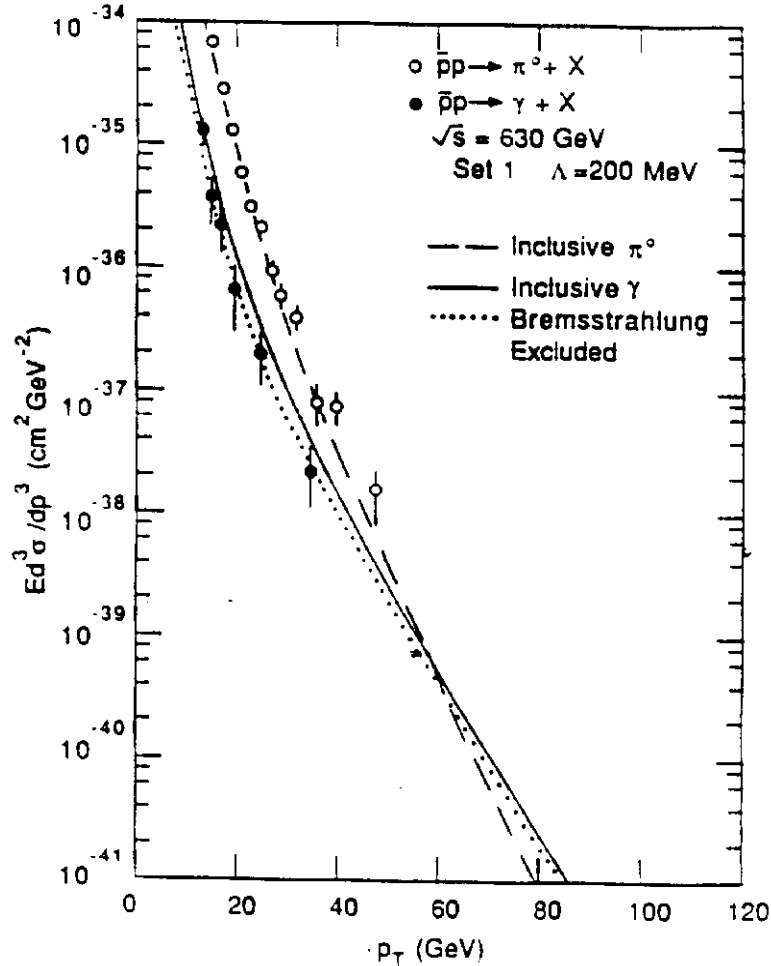

Figure E.8: UA2 data on $p_\perp$ distributions of π^0 and γ.

In Fig. E.9, we show Collider data on single particle inclusive production at low $p_\perp$ over a wide range of center-of-mass energies. This data is fit to a power law in transverse momentum. However, that power law is much steeper than the $1/p_\perp^4$ behavior that one expects for the inclusive jet distribution due to fragmentation effects.
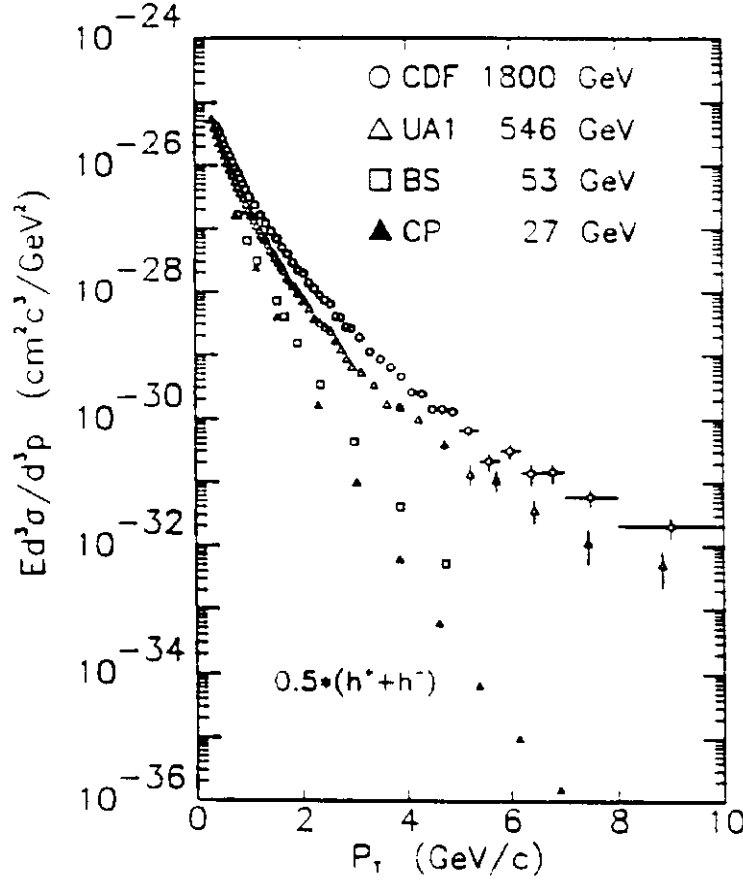

Figure E.9: Collider data on single particle inclusive production at low $p_\perp$.

Clearly, one can see that at a fixed transverse momentum the scaling behavior of jets feeds down into the behavior of single particles. At a fixed transverse momentum the cross-section rises rapidly as a function of energy. Looking at Fig. E.9, we can see that the cross-section is of the order millibarns at a transverse momentum of 2 GeV. This data was plotted along with the data from inclusive jet production in Section D. We saw that it fell much below the inclusive jet cross-section at moderate transverse momenta, which are 5 to 10 GeV and above. This

105

behavior is additional evidence for the soft fragmentation of light particles from jets.

$$\left(\frac{d\sigma}{\pi\,dy\,dp_\perp^2}\right)_{y=0} \sim A/(p_\perp + p_0)^n$$

$$A \sim 450 \; mb/\text{GeV}^2$$

$$p_0 \sim 1.3 \; \text{GeV} \qquad\qquad (\text{E.8})$$

$$n \sim 8.2$$

$$\left(\frac{d\sigma}{dy\,dp_\perp}\right)_{y=0} \sim \frac{2\pi p_\perp A}{(p_\perp + p_0)^n} \sim 0.3 \; mb/\text{GeV}\bigg|_{p_\perp = 2 \; \text{GeV}}$$

What about the fragmentation functions for heavy particles? They can be summed up in a kinematic statement that heavy particles in a decay carry off most of the momentum. This is familiar if one looks at say, Λ particle weak decay. The proton takes off essentially all of the momentum and the pion is soft. In Fig. E.10, we show a quark level schematic diagram for a heavy quark fragmenting into a meson consisting of a heavy quark and a light anti-quark which it picks up out of the sea.
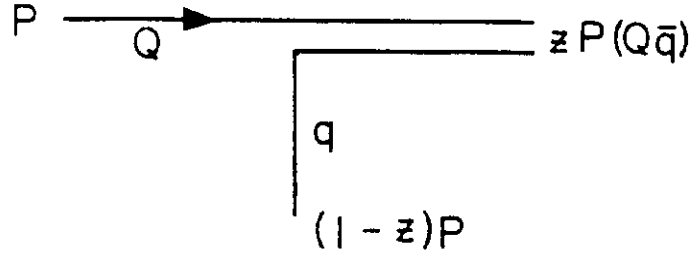

Figure E.10: Quark level diagram for heavy quark fragmentation into a $Q\bar{q}$ meson.

Just as we did in the case of looking at bremsstrahlung amplitudes in Eq. B.10, we look at the perturbation theory amplitude. The amplitude with the smallest virtuality is the largest, so that the amplitude is proportional to the inverse of the energy difference between the initial and final state. Assuming that the hadron or

meson has roughly the same mass as the heavy quark, we get a simple expression for the amplitude.

$$
\begin{aligned}
A &\sim 1/\Delta E \\
\Delta E &= E_Q - E_{Q\bar{q}} - E_q \\
&\simeq p + M_Q^2/2p - zp - (1-z)p - M_{Q\bar{q}}^2/2zp - M_q^2/2(1-z)p \\
&\simeq \left[M_Q^2/2 - M_{Q\bar{q}}^2/2z - M_q^2/2(1-z) \right]/p
\end{aligned}
\tag{E.9}
$$

This basically kinematic statement, in fact, seems to be borne out by the data in Fig. E.11 which is e^+e^- Collider data on the fragmentation of c and b quarks. In fact, in both cases these are fairly hard fragmentations which get harder as the mass increases from c to b. The average value of z for charm fragmentation is 0.6 whereas for b fragmentation it is 0.85.
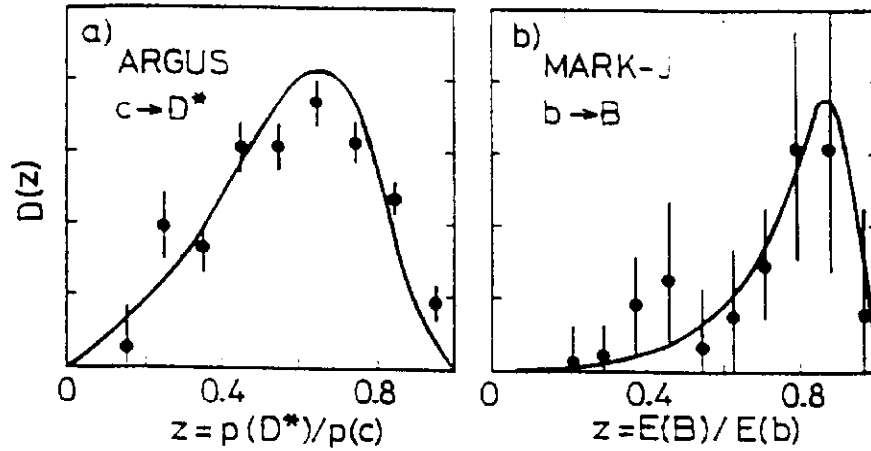

Figure E.11: e^+e^- Collider data on $c \to D$ and $b \to B$ fragmentation.

This behavior is in distinction to the soft exponential fragmentation of light pion fragments which presumably come from fragmentation of effectively massless up and down quarks or gluons. The data confirms a rough estimate given in Eq. E.10, which is called the Peterson form for the fragmentation functions.

$$\begin{aligned}
M_Q &\simeq M_{Q\bar{q}} \\
A &\sim \frac{2p}{M_Q^2}\left[1 - \frac{1}{z} - \frac{M_q^2/M_Q^2}{(1-z)}\right]^{-1} \\
zD(z) \sim |A|^2 &\sim 1/\left[1 - \frac{1}{z} - \frac{(M_q/M_Q)^2}{1-z}\right]^2 \\
&\rightarrow \left[z/(1-z)\right]^2 \big|_{M_Q \rightarrow \infty}
\end{aligned} \qquad (E.10)$$

In the limit that the heavy quark mass is much much greater than the light quark mass, we have a distribution function $zD(z)$, which goes like $1/(1-z)^2$. That means that the heavy quark takes off all of the momentum in fragmenting into a meson because it comes out at $z = 1$.

We are now ready to put together some of these fragmentation and decay ideas and look at the inclusive distribution of muons at the CERN Collider. The inclusive transverse momentum distribution of muons in a Monte Carlo model is shown in Fig. E.12. First we see the jet cross-section which is the largest cross-section of any of the ones we discussed at a given transverse momentum. We also show the Monte Carlo calculations for heavy flavor production and show the B cross-section. If you recall, the fragmentation function is quite hard, so that the relationship between the quark and the B meson distributions as a function of transverse momentum is reasonably closely coupled.
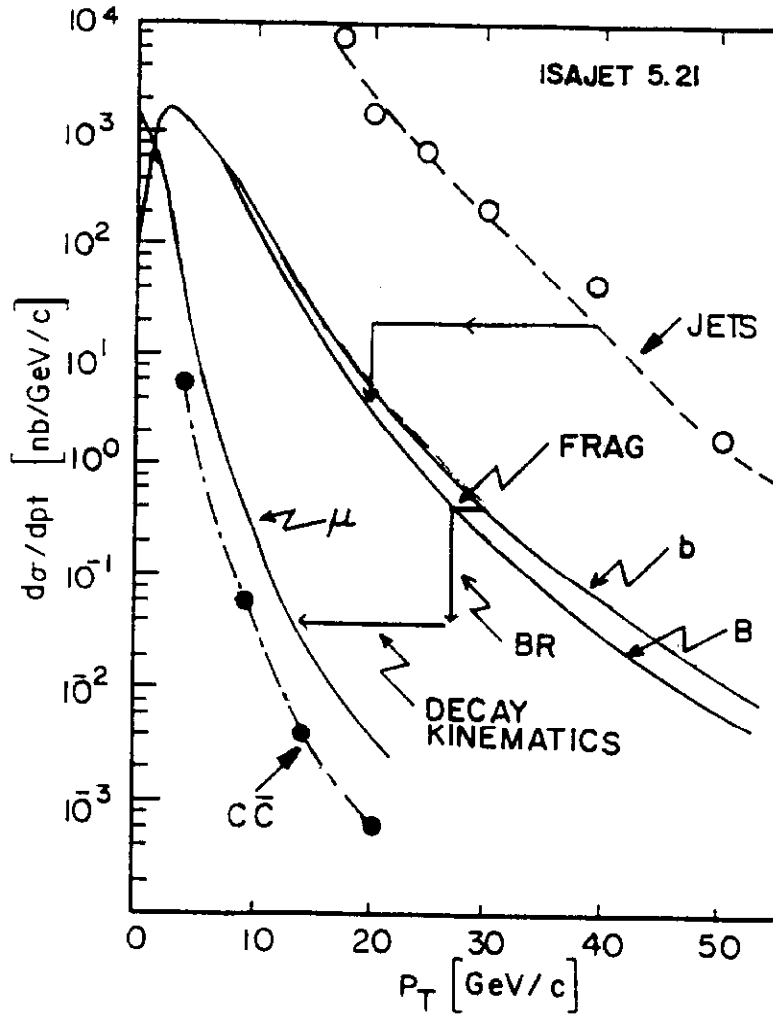
Figure E.12: Inclusive $p_\perp$ distributions of muons. Jets and b are also shown, along with $b \to B$ fragmentation. $B \to \mu$ decays are indicated. The yield from c quarks is also shown.

Note that the $2 \to 3$ process of gluon-gluon scattering followed by quark anti-quark pair creation may be thought of as a gluon jet decay into quark pairs. In discussing heavy flavors, we noted that $2 \to 3$ processes were comparable to $2 \to 2$ processes. Thus, it is perhaps not surprising that the relationship of $d\sigma/dp_\perp$ for jets to that for B mesons is characterized by the kinematics for $n = 2$ (i.e., $p_\perp \to p_\perp/2$) and a flavor independent branching fraction for gluon jets, $[B(J \to b) \sim b/(u+d+s+c+b) \sim 1/5]$. These relationships are also indicated in Fig. E.12.

The B mesons decay semileptonically into muons. There are again two effects. First, there is a quark counting result that the semileptonic branching ratio into

muons is one ninth. Then the decay kinematics are such that the transverse momentum is rescaled down by a factor of three. These two effects leads us to the muon distribution which is also shown in Fig. E.12. For comparison, we also show Monte Carlo results for muons from charm decays. If you recall from Section D on heavy flavor production, the ratio of $b \to c$ should go like the square of the quark masses. That would mean that there are about ten times more charm particles than b particles at asymptotic energies. However, we see that at 5 GeV transverse momentum and above, the muons from B decay dominate over those from D decay. The reason is that the softer fragmentation function from the D decays wipes out, at fixed $p_\perp$, the advantage one has in the production cross-section. That is interesting, because if one sits at a transverse momentum of a few GeV and triggers on muons, one is preferentially triggering on B decays and not D decays.

The UA1 data for the inclusive single muon transverse momentum distribution is shown in Fig. E.13. Above a transverse momentum of about 30 GeV one is dominated by the leptonic decays of the gauge bosons, basically because the Jacobean peak puts most of the cross-section at a tranverse momentum equal to half the mass of the gauge bosons. At lower transverse momenta (say 30 GeV and below) the muon rate is dominated by the semileptonic decays of B and D particles. There are other topological properties of the two types of processes which allow a clean separation between gauge bosons and heavy flavors.
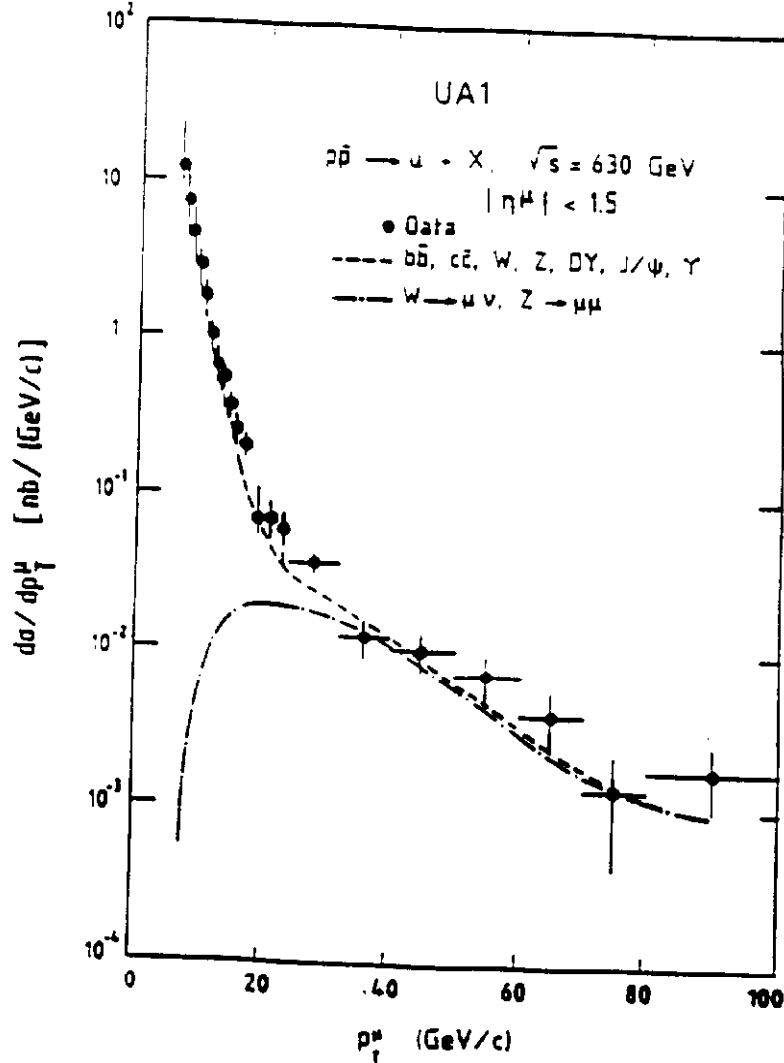
Figure E.13: UA1 data on the $p_\perp$ distribution of muons.

Let's turn now from single muons to dimuons and look at the UA1 data on high tranverse momentum production of ψ mesons as seen in Fig. E.14. Recall in Section C that the gluon fusion prediction for the total inclusive cross-section for ψ's was 10,000 nanobarns or 10 microbarns. This fusion process, however, leads to ψ's with very low transverse momentum, $\sim \Lambda$. By comparison the gluon-gluon fusion into a virtual gluon which then decays into a $B\bar{B}$ pair has a cross-section which is comparable and of order 10 microbarns. In this case, the natural scale of the B's transverse momentum comes from the $2 \to 2$ processes. That scale has a transverse momenta of order the mass of the B's or 5 GeV. The inclusive branching

111

fraction for $B \to \psi+$ anything is about 1%, which means that the cross-section times branching ratio for gluon fusion production of $B\bar{B}$ pairs followed by inclusive decay into ψs is about 100 nanobarns. At moderate transverse momentum, say of order the B mass, all ψs (to first order) come from inclusive B decays.
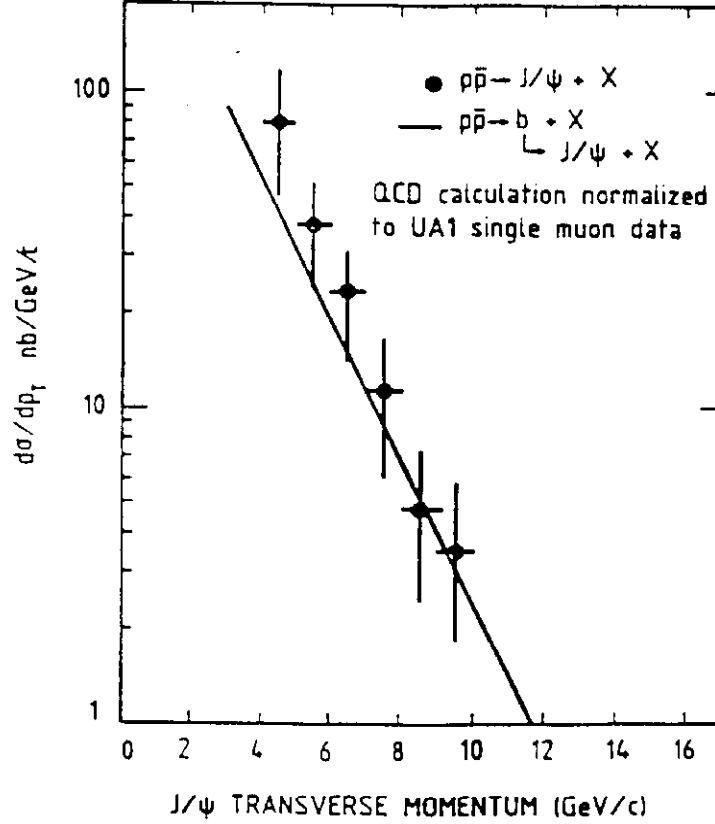

Figure E.14: UA1 data on high $p_\perp$ production of $\psi \to \mu^+\mu^-$ mesons.

The data in Fig. E.14 confirm this expectation in the sense that the scale is about 100 nanobarns and the characteristic fall-off with transverse momenta is characterized by a slope which is of the same order as the B mass. This fact is again experimentally interesting because a possible tag for B's is the appearance of the ψ at moderate transverse momentum, of order 5 GeV.

Another use for dimuons is to confirm the need for $2 \to 3$ processes in heavy flavor production. You recall in Section D that we said we needed $2 \to 3$ processes to explain the magnitudes of the cross-sections. A nice confirmation of that need is to look at the azimuthal correlations in dimuon production. The $2 \to 2$ gluon

112

fusion diagrams for heavy flavor production are shown in Fig. E.15 along with the 2 → 3 processes of gluon-gluon scattering with subsequent virtual decay of a gluon into a heavy quark anti-quark pair. It should be fairly obvious that in the 2 → 2 process the muons will come out on opposite sides of the azimuthal plane, whereas in the case of 2 → 3 processes they will come out on the same side.
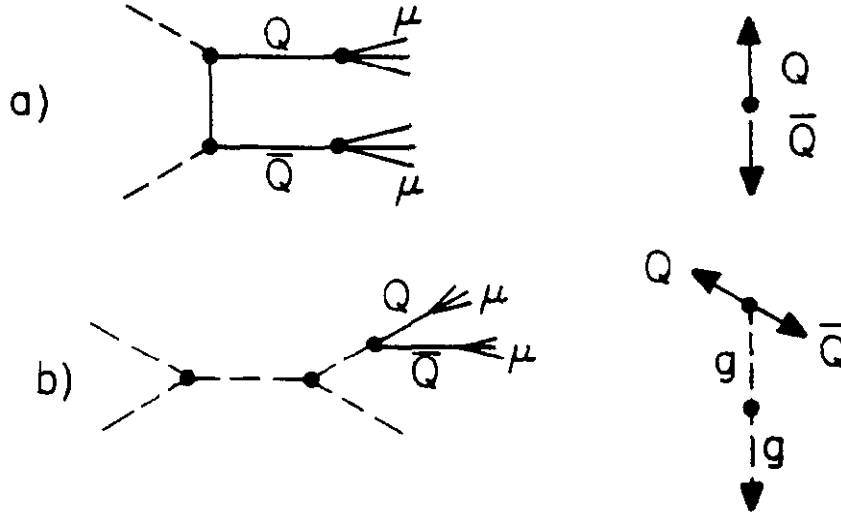

Figure E.15: Gluon diagrams for heavy flavor production. For a) $\phi_{\mu\mu} \sim \pi$ while for b) $\phi_{\mu\mu} \sim 0$.

Data on the azimuthal correlation is shown in Fig. E.16. Clearly both these processes occur in the sense that we have a peak for both toward and away correlations of the dimuons. That means that both these processes are comparable. As we said in Section D, we expect that the extra factor of α_s that one needs in a 2 → 3 strong process is cancelled by the fact that gluon gluon scattering is considerably larger than the gluon-gluon fusion into heavy quark pairs.
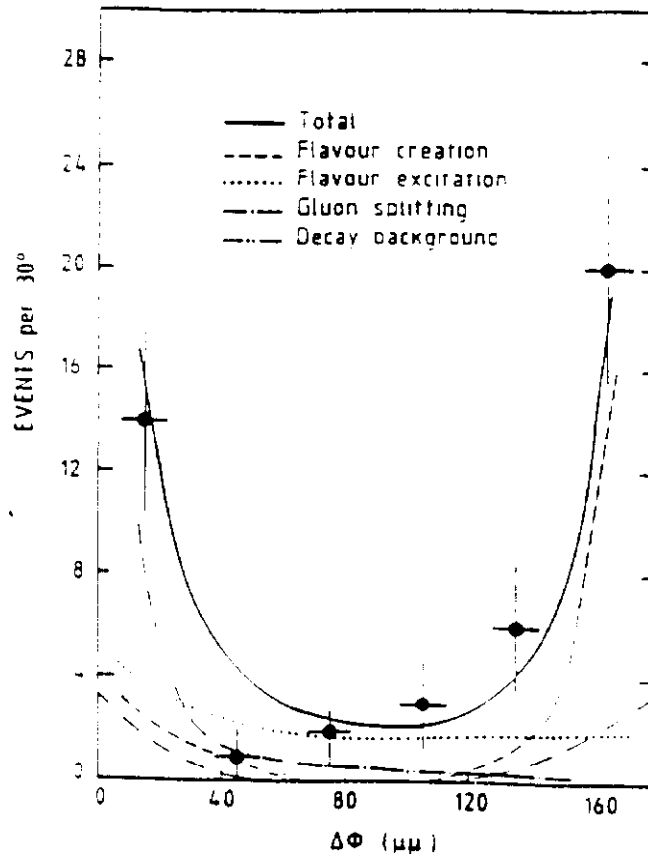
Figure E.16: Collider data on the relative azimuthal angle of μ^+ to μ^- in JJ dimuon production.

This data is a nice confirmation of the assertion, made in Section D, that we need $2 \to 3$ processes to explain the magnitude of the cross-section. By that we mean we needed the other process so that the quark mass parameter that one uses in the theory agrees with its spectroscopic value.

Most spectacularly perhaps, the sign selection of dimuons has proven in the CERN Collider experiments to require that the $B\bar{B}$ system mixes in a way very similar to that of the $K\bar{K}$ system. Heavy flavors are made in pairs of strong interaction eigenstates, say, $B\bar{B}$. Then the decay $b \to cW^-$ implies that $B\bar{B}$ goes to $D\bar{D}W^+W^-$. The virtual W's leptonically decay into $\mu^+\mu^-$. This decay scheme means that the "leading" dimuons are always unlike sign. However, what was seen in the CERN Collider experiments was a large number of like-sign dimuons which could not be explained by the subsequent "non leading" decays of the D and $\bar{D}$s. These decays could be removed on kinematic grounds because the muons from the D decay have lower transverse momenta as we have already discussed. Since

they couldn't be explained in that way, they were taken as evidence for the weak mixing of $B\bar{B}$ before the decay. Thus the sign selected dimuon sample has been extraordinarily useful in contributing to our knowledge of B quark spectroscopy. Remember that mixing of B's has implications for top quark masses and/or V_{bu} (three generation unitarity).

Finally, just a word about future and/or present uses for muons. If the elusive top quark is heavier than the W then the diagram for $2 \rightarrow 2$ production and subsequent decay, of top anti-top is shown, in Fig. E.17. The topology of those events will be two real Ws plus two jets. The Ws decay leptonically and the two b jets may or may not decay in some topologically interesting way into ψ's or leptons. There will be some missing energy indicating the existence of neutrinos. We can estimate the cross-sections for top from simple extrapolation of what we did in Section D. For example, a 200 GeV top has a production cross-section something like 2 picobarns.
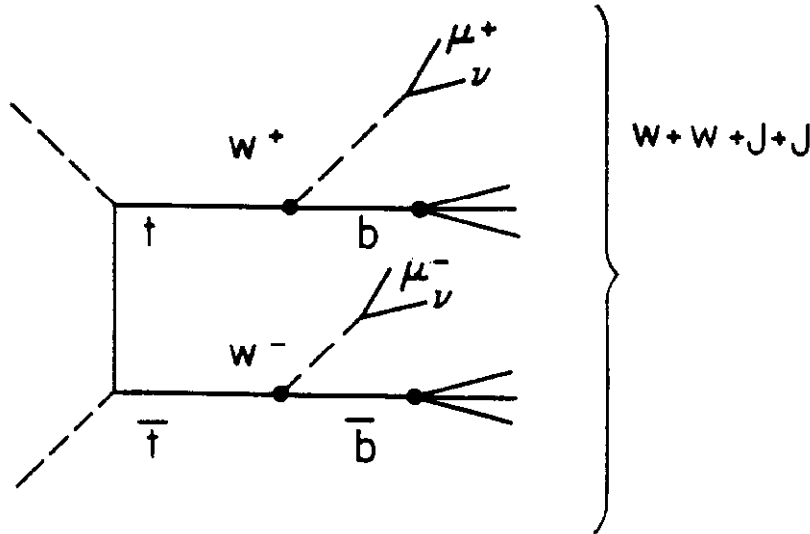

Figure E.17: Diagram for $2 \rightarrow 2$ production and decay of $t\bar{t}$ for heavy top.

What about backgrounds? For example, at a $B\bar{B}$ mass of 100 GeV we still have a differential cross-section of 20 picobarns per GeV which is not substantially different from the $t\bar{t}$ cross-section. These $B\bar{B}$ pairs in their semileptonic decay

would lead to rather high mass dimuons, say of order, 30 GeV from 100 GeV. So in fact, thinking about these numbers leads us to believe that the top search is not such a simple thing. One has to have a reliable estimate of the QCD backgrounds from Ws and from other heavy flavors. Finding the top is not going to be a trivial task for proton anti-proton colliders.

$$\frac{d\sigma(b\bar{b})}{dM}\Bigg|_{M=100} \sim 20 \ pb/\text{GeV}$$

$$M_{\mu\mu} \sim 2k_\perp \sim 30 \ \text{GeV} \tag{E.11}$$

$$\sim M_{b\bar{b}}/3$$

Some crude expectations are shown in Table E.1.

Table E.1.

Cross-Sections for Top Quarks

and Related Particles.

M_t (GeV)	$\sigma_{t\bar{t}}(pb)$	$\sigma_{WW}(pb)$	$\sigma_{b\bar{b}}(pb)$
120	40		
160	10	5	10^7
200	2		
240	0.8		

By comparison, the Drell-Yan expectation for WW pairs is about 5 picobarns, whereas the cross-section for $B\bar{B}$ pairs (being much lighter) is a million times larger or ten microbarns. In fact, the QCD gluon fusion process tails can give B's at large mass (large transverse momentum).

This brings us to the end of Section E. In summary, what we did is look at decays and fragmentation starting with fragmentation of jets into light particles. We defined the fragmentation function and showed how a simple fragmentation parameterization led to a rapidity plateau and a logarithmic dependence of the jet multiplicity on the mass of the jet. We also showed how a simple fragmentation

116

can lead to the same sort of power law behavior of parent to child; for example, jet to π^0. We also looked at the data on inclusive single particle production at lower transverse momentum. Then we turned to heavy particle fragmentation and made a very simple argument leading to the Peterson form of the fragmentation function. This form was confirmed by the data on the fragmentation of both c and b quarks. Finally we combined a lot of these ideas together to look at muons from both the Jacobean peaks of gauge bosons and from the semileptonic decays of heavy flavors. We showed that, due to the softness of the fragmentation function, both single leptons and dimuons from ψ decay at moderate transverse momentum are dominated by B's and not D's as one would expect from just thinking about the production cross-section. Finally, we talked about the use of dileptons for confirming the existence of $2 \to 3$ processes and as a signal for mixing.

F. SUMMARY

In Section A, the Standard Model was specified. Certain remaining questions were raised such as the Higgs mass, the top quark mass, and the total number of generations. The whole question of quark and lepton (including neutrino) masses is basically ad hoc.

In Section B, we saw that the pointlike behavior of quarks was valid. However, the distribution functions $f(x)$ are measured, not calculated from first principles. In particular, the gluons $g(x)$ are known very indirectly. This fact has implications for low x physics, the "gluon bomb," and the failure of the impulse approximation.

In Section C, we looked at the cross-sections for ϕ, ψ, ψ', and Υ production versus s. They seem consistent, but η_c, η_b, and θ rates are lacking. The cross-sections for W and Z production are calculable which provides a consistency check on $\sin\theta_W$ as measured in neutral-current interactions. Still, precise data on Γ_W/Γ_Z and M_t are lacking, which makes a definitive statement on the number of generations impossible. The Higgs has not been seen yet, and Tevatron Upgrade and SSC implications were discussed.

While waiting for the Higgs, we looked at Drell-Yan in Section D. This mechanism, or one very similar, will give us $W\gamma$ and WW pairs at the Tevatron. That

event type will give us our first tests of triple boson gauge couplings. Jet production gave us a limit on compositeness and a view of $2 \to 3$ processes. The rise in σ_I, if it is due to minijets, needs to be corroborated by measuring the real part of the elastic amplitude at the Tevatron. Data will soon be forthcoming. Finally prompt photons and heavy flavors give us a window on the pointlike processes involved. The prompt photon/jet angular distribution confirms the fermion/boson propagators. The rate and topology of $Q\bar{Q}$ production confirms the need for $2 \to 3$ processes. Finally, if $M_t > M_W$, as one might suspect from $B - \bar{B}$ mixing, $t\bar{t}$ production will be seen at the Tevatron.

Section E saw a discussion of fragmentation. Light and heavy quark fragmentation functions are consistent from e^+e^- to $\bar{p}p$ colliders and exhibit scaling. Single leptons are used to extract W and $b\bar{b}$ rates. Dileptons are used to get Z and $B \to \psi X$, $\psi \to \ell^+\ell^-$ rates. Pairs of dileptons also confirm the need for $2 \to 3$ processes in $B\bar{B}$ mixing which feed back on questions of the size of M_t.

Clearly, the next few years of Tevatron Collider data will serve to help in answering many of these questions. Presumably top will be found, and the number of generations will be pinned down. The path the Upgrade takes will provide further direction to Collider Physics. It should be an exciting time!

<u>References</u>

1. Eichten, Hinchliffe, Lane, Quigg, Rev. Mod. Phys. <u>56</u>, 4 (1984).

2. Eichten, FNAL CONF-85/178-T.

3. Barger and Phillips, <u>Collider Physics</u>, Addison Wesley (1987).

4. Quigg, <u>Gauge Theories of the Strong, Weak, and Electromagnetic Interactions</u>, Benjamin/Cummings (1983).

5. Owens, Rev. Mod. Phys. <u>59</u>, 465 (1987).

6. <u>Proton-Antiproton Collider Physics</u>, Directions in High Energy Physics, Vol. 4, World Scientific (1989).

7. 7th Topical Workshop on Proton-Antiproton Collider Physics, Fermilab, 20-24 June (1988).

8. P. Bagnia, S. Ellis, Ann. Rev. Nuc. Part. Sci. $\underline{28}$ (1988).

9. D. Green, FN-433, Fermilab (1986).